

Copyright  
by  
Thong Quang Ngo  
2015

**The Dissertation Committee for Thong Quang Ngo Certifies that this is the approved version of the following dissertation:**

**Atomic Layer Deposition of Functional Materials**

**Committee:**

---

John G. Ekerdt, Supervisor

---

Alexander A. Demkov

---

Gyeong S. Hwang

---

Christopher J. Ellison

---

Brian A. Korgel

**Atomic Layer Deposition of Functional Materials**

**by**

**Thong Quang Ngo, B.E.**

**Dissertation**

Presented to the Faculty of the Graduate School of

The University of Texas at Austin

in Partial Fulfillment

of the Requirements

for the Degree of

**Doctor of Philosophy**

**The University of Texas at Austin**

**May 2015**

## **Dedication**

This is dedicated to my wife, Van, to my parents, to my secondary school teacher, Toan, to my younger brother, Thien, and to all other my family members.

Gửi tặng vợ người luôn yêu thương, chăm sóc và đồng hành cùng chồng qua những ngày tháng vui và buồn, thăng và trầm trong cuộc đời.

Gửi tặng ba má người đã nuôi dưỡng, chăm lo cho anh em con bằng cả đời vất vả và lam lũ trên “quê hương xứ Cát”. Luận văn này chính là một trong những thành quả mà con muốn gửi tặng ba má. Gửi tặng Thiên cho sự yêu thương, lo lắng của em dành cho gia đình và anh.

Gửi tặng thầy Toàn, người đã định hướng, dạy dỗ và luôn dõi theo con để con có được như ngày hôm nay.

Gửi tặng tất cả các thành viên trong gia đình và bạn bè đã luôn tin tưởng và ủng hộ con/em/anh.

## Acknowledgements

There are many individuals to whom I am grateful for their guidance and support through the process of this dissertation. I first would like to have my sincerest thanks to my advisor, Dr. John G. Ekerdt, for his tremendous guidance, support, and encouragement. He has excellent time management skills, providing immediate feedback on papers and presentations. He is not only an excellent scientist, but also is very kindly person. This dissertation would not have been possible without him. He is considerate for my family life. I really appreciate long vacations he gave me for my trips to Vietnam for my engagement and wedding. I consider myself very fortunate to have had him as my advisor. I would like to have special thanks to Dr. Alexander A. Demkov for his guidance and insightful discussions. He has been much like my co-advisor during my time in the Materials Physics Lab. I would also like to thank Dr. Gyeong S. Hwang, Dr. Christopher J. Ellison, and Dr. Brian A. Korgel for their insight and generous feedback on my research as committee members.

I am extremely grateful to the lab manager and brilliant research scientist, Dr. Agham Posadas, for his material and equipment knowledge, experimental guidance, and his time to answer innumerable my questions. I would like to have special thanks to my friend, Martin D. McDaniel for his help during my graduate study. I would also like to thank former and current group members, Sonali Chopra, Blair Cox, Tuo Wang, Tyler Elko-Hansen, Joe McCrate, Wen Liao, Zizhou Zhang, Brad Leonhardt, Dan Bost, Edward Lin, and our newest members Bryce Edmondson, Shen Hu, Himmi Nallan. My thanks are also extended to the Materials Physics Lab members including Miri Choi, Patrick Ponath, and Kristy Kormondy.

I am also thankful to the Vietnam Education Foundation for providing me the opportunity to study in the US. The Vietnam Education Foundation staff including Dr. Lynne McNamara, Dr. Phuong Nguyen, Ms. Hanh Bui, Ms. Sandarshi Gunawardena, Ms. Diana Martens, and other members have been very helpful in processing my paperwork and immigration documents.

I would like to thank The University of Texas at Austin and the Cockrell School of Engineering for providing me such a great opportunity to pursue my Ph.D. degree. My thanks are extended to Dr. Isaac Sanchez and the staff in our Department: Randy Rife, Eddie Ibarra, Kevin Haynes, Butch Cunningham, Kate Baird, Jim Smitherman, T Stockman, Carrie Brown, Tammy McDade, and Megan Anguiano for their help during my graduate study. I would like to acknowledge the support from Dr. Zhou Jianshi for the superconducting quantum interference device magnetometer measurement, Damon Smith and Josh Bolinger for their support at the Center for Nano and Molecular Science Technology, Dr. Steve Swinnea and Vince Lynch for x-ray diffractometer training. My acknowledgement also goes to my friends for your time and friendship.

I am forever grateful to my parents and my younger brother, Thien, for all their support through difficulties I have been facing. I am also forever grateful to my secondary school math teacher, Toan, who has been watching and teaching me along my life. Lastly and mostly, I would like to thank Van for her love and for walking with me through the highs and lows of my life.

My Ph.D. projects were funded by the National Science Foundation (Awards: DMR-1006725, DMR-1207342, and EEC-1160494), the Office of Naval Research (Grant N000 14-10-10489), and the Air Force of Scientific Research (Grant FA9550-12-10494).

# Atomic Layer Deposition of Functional Materials

Thong Quang Ngo, Ph.D.

The University of Texas at Austin, 2015

Supervisor: John G. Ekerdt

Atomic layer deposition (ALD) has emerged as an important technique for depositing thin films in both scientific research and industrial applications. The goal of this work is to integrate functional materials using ALD including high- $\kappa$  dielectric,  $\text{LaAlO}_3$ , ferroelectric  $\text{BaTiO}_3$ , photocatalytic  $\text{CoO}$ , and room temperature ferromagnetic thin films of Co metal for spin-transfer torque random-access memory applications. The work is also to demonstrate the formation of a quasi-two-dimensional electron gas (2-DEG) at the  $\gamma\text{-Al}_2\text{O}_3/\text{SrTiO}_3$  heterointerface enabling a method for all-oxide device manufacturing using ALD.

High permittivity oxide thin films are needed to replace  $\text{SiO}_2$  in complementary metal oxide semiconductor (CMOS) transistors. The replacement of  $\text{SiO}_2$  by hafnium oxide-based high- $\kappa$  materials in CMOS devices in 2007 was a revolutionary development in semiconductor front end of line. The continued device feature shrinking requires higher- $\kappa$  dielectrics, compared to  $\text{HfO}_2$ -based materials. Crystalline perovskite oxides, such as  $\text{SrTiO}_3$ ,  $\text{LaAlO}_3$ , and  $\text{BaTiO}_3$ , etc. have from high to very high dielectric constant and being proposed to replace  $\text{HfO}_2$ -based materials in CMOS devices if the leakage problem is resolved. The work explores the monolithic integration of crystalline perovskite oxide films with  $\text{Si}(001)$  using combined molecular beam epitaxy (MBE) and ALD techniques. Four unit cells of  $\text{SrTiO}_3$  were grown directly on  $\text{Si}(001)$  by MBE and

transferred *in-situ* into the ALD chamber for further depositions. The integration of oxide thin films on Si(001) using the MBE-ALD technique allows us to maintain clean oxide/Si(001) interfaces since low temperatures (180–250 °C) were maintained during the ALD deposition.

The goal of my work is also to explore processes to enable area selective deposition of cobalt (II) oxide, CoO. The effectiveness of poly(trimethylsilylstyrene) in selectively inhibiting surface nucleation of CoO on SiO<sub>2</sub> and MgO substrates is demonstrated. Carbon-free cobalt thin films are formed by reducing CoO using Al and Sr metals to scavenge oxygen from CoO. The work explores the ability to control the structure and morphology of the resultant cobalt film by tuning the reduction conditions, allowing us to tune magnetic properties of the cobalt thin film.

My work also focuses on the growth of  $\gamma$ -Al<sub>2</sub>O<sub>3</sub> on the TiO<sub>2</sub>-terminated SrTiO<sub>3</sub> substrate at temperatures higher than 300 °C. The formation of a quasi-2-DEG is found at the  $\gamma$ -Al<sub>2</sub>O<sub>3</sub>/TiO<sub>2</sub>-terminated SrTiO<sub>3</sub> interface. *In-situ* x-ray photoelectron spectroscopy reveals the presence of Ti<sup>3+</sup> feature at the heterointerface. Conductivity at the interface was found to be proportional to the amount of Ti<sup>3+</sup> species. Oxide quasi-2-DEG might provide opportunities for new generations of all-oxide electronic devices using ALD.

## Table of Contents

List of Tables .....	xii
List of Figures .....	xiii
Chapter 1: Introduction and dissertation overview .....	1
1.1. History of atomic layer deposition.....	1
1.2. Principle and applications.....	2
1.2.1. ALD of high- $\kappa$ materials for Metal Oxide Semiconductor Field Effect Transistor (MOSFET) application .....	4
1.2.2. ALD for DRAM cell capacitors.....	6
1.2.2.1. ALD of $\text{Al}_2\text{O}_3$ for DRAM dielectric.....	6
1.2.2.2. ALD of higher- $\kappa$ oxides for DRAM dielectric .....	7
1.2.3. ALD for other applications .....	7
1.3. Overview of this dissertation .....	8
1.4. References.....	10
Chapter 2: Epitaxial growth of $\text{LaAlO}_3$ on $\text{SrTiO}_3$ -buffered $\text{Si}(001)$ substrates by atomic layer deposition .....	13
2.1. Introduction.....	13
2.2. Experimental .....	15
2.3. Results and discussion .....	17
2.4. Summary .....	30
2.5. References.....	30
Chapter 3: Growth of crystalline $\text{LaAlO}_3$ by atomic layer deposition: a comparison on $\text{SrTiO}_3/\text{Si}(001)$ and $\text{SrTiO}_3$ substrates .....	36
3.1. Introduction.....	36
3.2. Methodology .....	38
3.3. Results and discussion .....	39
3.4. Summary .....	47
3.5. References.....	47

Chapter 4: Epitaxial <i>c</i> -axis oriented BaTiO <sub>3</sub> thin films on SrTiO <sub>3</sub> buffered Si(001) by atomic layer deposition .....	51
4.1. Introduction.....	51
4.2. Experimental.....	52
4.3. Results and discussion .....	54
4.4. Summary .....	60
4.5. References.....	61
Chapter 5: Quasi-Two-Dimensional Electron Gas at the Interface of $\gamma$ -Al <sub>2</sub> O <sub>3</sub> /SrTiO <sub>3</sub> Heterostructures Grown by Atomic Layer Deposition .....	64
5.1. Introduction.....	64
5.2. Experimental.....	66
5.3. Results and discussion .....	68
5.4. Summary .....	79
5.5. References.....	79
Chapter 6: Atomic Layer Deposition of Photoactive CoO/SrTiO <sub>3</sub> and CoO/TiO <sub>2</sub> on Si(001) for Visible Light Driven Photoelectrochemical Water Oxidation ...	82
6.1. Introduction.....	82
6.2. Experimental and theoretical details.....	85
6.3. Results and discussion .....	88
6.3.1. Cobalt oxidation state .....	88
6.3.2. Crystallinity and roughness of CoO/STO and CoO/TiO <sub>2</sub> films	89
6.3.3. Visible light performance for water photooxidation.....	95
6.3.4. Band offsets of the CoO/STO and CoO/TiO <sub>2</sub> hererojunctions	96
6.3.4.1. Experimental measurements .....	96
6.3.4.2. Theoretical calculations .....	98
6.4. Summary.....	102
6.5. References.....	102

Chapter 7: Atomic layer deposition of CoO on SrTiO <sub>3</sub> -buffered Si(001), SiO <sub>2</sub> /Si, and MgO(001) substrates and methods to form thin magnetic Co metal films.	107
7.1. Introduction.....	107
7.2. Experimental.....	111
7.3. Results and discussion .....	112
7.3.1. Growth of CoO on amorphous SiO <sub>2</sub> /Si and single crystal MgO(001) substrates.....	112
7.3.2. Transformation of CoO to Co spinel, Co <sub>3</sub> O <sub>4</sub> .....	116
7.3.3. Transformation of CoO to Co metal and magnetization of Co films .....	118
7.4. Summary.....	129
7.5. References.....	130
Chapter 8: Research Summary.....	134
8.1. Conclusion .....	134
8.2. Recommendation for future work.....	137
Appendix.....	139
First-Author Publications.....	139
Co-author Publications.....	140
Technical Presentations .....	141
Bibliography .....	142
Vita.....	159

## List of Tables

Table 2.1. XPS peak assignments (eV).....	23
Table 6.1. VBMs of pure CoO, STO, TiO <sub>2</sub> and associated core level binding energies .....	98

## List of Figures

- Figure 1.1. Schematic of ALD process. (a) Substrate surface has natural functionalization or is treated to functionalize the surface. (b) Precursor A is pulsed and reacts with surface. (c) Excess precursor and reaction by-products are purged with inert gas carrier. (d) Precursor B is pulsed and reacts with surface. (e) Excess precursor and reaction by-products are purged with inert carrier gas. (f) Steps 2–5 are repeated until the desired material thickness is achieved (Reprinted with permission from Ref. 7). .....3
- Figure 2.1. RHEED images captured before ALD growth [(a), (b)] and after annealing at 600 °C for 2 h of a 10 nm thick LAO film [(c) and (d)]. The beam was aligned along the <100> for (a) and (c), and <110> azimuth for (b) and (d). .....19
- Figure 2.2. AFM image of a  $5 \times 5 \mu\text{m}^2$  area of an 8-nm thick LAO film grown by ALD on STO-buffered Si(001) after annealing at 600 °C for 2 h. ...19
- Figure 2.3. X-ray diffraction pattern of a 10-nm thick LAO film grown by ALD on STO-buffered Si(001) at 250 °C. The sample was post-deposition annealed in vacuum at 600 °C for 2 h. ....21
- Figure 2.4. Rocking curves around the LAO(001) Bragg peak at a fixed  $2\theta=23.68^\circ$  for a 10-nm thick LAO film grown by ALD on STO-buffered Si(001) after annealing at 600 °C for 2 h (a) and after additional annealing at 750 °C for another 2 h (b). .....22

Figure 2.5. (a) X-ray photoelectron spectrum of Si 2s for four unit cell STO-buffered Si(001) grown by MBE: the dotted curves show the fits for Si <sup>0</sup> (red) and Si in SiO <sub>x</sub> (blue); (b) X-ray photoelectron spectrum of Ti 2p for four unit cell STO-buffered Si(001) grown by MBE: the dotted curves show the fits for Ti <sup>4+</sup> (red), Ti <sup>3+</sup> (blue), and Ti <sup>2+</sup> (purple) as-described in Table 2.1.....	24
Figure 2.6. X-ray photoelectron spectra of Si 2s after ALD (a), after annealing at 600 °C for 2 h (b), and after additional annealing at 750 °C for another 2 h (c), respectively: the dotted curves show the fits for Si <sup>0</sup> (red) and Si in SiO <sub>x</sub> and/or strontium silicate (blue).....	26
Figure 2.7. X-ray photoelectron spectra of Ti 2p after ALD (a), after annealing at 600 °C for 2 h (b) and after additional annealing at 750 °C for another 2 h (c), respectively: the dotted curves show the fits for Ti <sup>4+</sup> (red), Ti <sup>3+</sup> (blue), and Ti <sup>2+</sup> (purple) as-described in Table 2.1.....	27
Figure 2.8. X-ray photoelectron spectra of Sr 3d after ALD (a), after annealing at 600 °C for 2 h (b) and after additional annealing at 750 °C for another 2 h (c), respectively: the dotted curves show the fits for Sr in STO (red), in strontium silicate (blue) as-described in Table 2.1. ....	27
Figure 2.9. Cross-sectional Z-contrast TEM image of a 12 nm LAO film on STO-buffered Si(001) after annealing at 600 °C for 2 h that illustrates the Si/STO/LAO interfaces. The inset is an expanded image Si/STO/LAO interface region. ....	29
Figure 2.10. Cross-sectional BF TEM of a 25 nm LAO film on STO-buffered Si(001) after annealing at 750 °C for 2 h.....	29

Figure 3.1. RHEED images of: (a) a four-unit-cell STO-buffered Si(001), (b) an as-deposited 10 nm LAO film on four-unit-cell STO-buffered Si(001), (c) the 10 nm LAO film grown on four-unit-cell STO-buffered Si(001) after annealing at 600 °C for 2 h, and (d) an 8 nm LAO film on STO substrate after annealing at 750 °C for 2 h. The beam was aligned along the  $\langle 110 \rangle$  azimuth for (a), (c) and (d).....41

Figure 3.2. (a) X-ray diffraction patterns of a 10-nm thick LAO film grown by ALD on STO-buffered Si(001) at 250 °C after a 2 h vacuum anneal at 600 °C (red curve), and after an additional vacuum anneal at 750 °C for another 2 h (blue curve); (b) Rocking curves around the LAO(001) Bragg peak at a fixed  $2\theta=23.68^\circ$  for the 10-nm thick LAO film after annealing at 600 °C for 2 h (red) and after additional annealing at 750 °C for another 2 h (blue).....42

Figure 3.3. XRD patterns around LAO(001) Bragg peak of different LAO film thicknesses shows that thicker LAO films, LAO(100) Bragg peak was shifted to a lower  $2\theta$  values indicating the out-of-plane lattice constant of LAO tends to be closer to the bulk value (3.79 Å).....43

Figure 3.4. (a) X-ray diffraction patterns of a 12-nm thick LAO film grown by ALD on STO(001) at 250 °C after a 2 h vacuum anneal at 750 °C.....44

Figure 3.5. La 3d (a) and Al 2p (b) X-ray photoelectron spectra of a 5 nm LAO film on four-unit-cell STO-buffered Si(001) as-deposited (red curves) and after 2 h vacuum anneal at 750 °C (blue curves).....45

Figure 3.6. O 1s X-ray photoelectron spectra of a 3 nm LAO film on four-unit-cell STO-buffered Si(001) as-deposited (a) and after 2 h vacuum anneal at 750 °C (b). The dotted-curves show the fits for O in SiO<sub>x</sub> (green), La<sub>2</sub>O<sub>3</sub> ((a)-blue), LAO ((b)-blue), Al<sub>2</sub>O<sub>3</sub> (purple). .....46

Figure 4.1. (a) and (b) are RHEED patterns of a 7 nm BTO film on four-unit-cell STO-buffered Si(001) as-deposited and after 5 min vacuum anneal at 600 °C, respectively. Both images are taken along <110> direction of STO. (c) Si 2p XP spectra of a typical four-unit-cell STO-buffered Si(001) film (red), a 3 nm ALD BTO film on four-unit-cell STO-buffered Si(001) as-deposited (blue), and the 3 nm BTO film after a 5 min vacuum anneal at 600 °C (green). Please note that there is a negligible change in Si-O bonding before and after the vacuum anneal, so the blue and green lines are almost identical. ....55

Figure 4.2. (a) XRD and (b) 2D-XRD patterns of an as-deposited 20 nm ALD BTO film on four-unit-cell MBE STO on Si(001). The lattice constants of the BTO film calculated from XRD are  $a = 3.93 \text{ \AA}$  and  $c = 4.02 \pm 0.01 \text{ \AA}$  demonstrating tetragonal structure of the as-deposited BTO film. ....58

Figure 4.3. STEM image of a 17 nm ALD-grown BTO film on four-unit-cell MBE-grown STO-buffered Si(001) after a 5 min vacuum anneal at 600 °C. 59

Figure 4.4. C-V(at 100 kHz) characteristics of an as-deposited 18 nm BTO film on 1.6 nm STO-buffered Si(001). .....60

Figure 5.1. RHEED patterns of: (a) TiO<sub>2</sub>-terminated STO substrate and (b) 27-nm-thick Al<sub>2</sub>O<sub>3</sub> grown by ALD on TiO<sub>2</sub>-terminated STO at 345 °C. RHEED patterns were taken along the <110> azimuth of the STO substrate; (c) XRD pattern of an 18-nm-thick Al<sub>2</sub>O<sub>3</sub> film on TiO<sub>2</sub>-terminated STO grown by ALD at 345 °C. ....69

Figure 5.2. In-plane grazing incident-XRD scan of 18-nm-thick ALD-grown Al<sub>2</sub>O<sub>3</sub> film on TiO<sub>2</sub>-terminated STO at 345 °C along (*h*00) direction. The strained Al<sub>2</sub>O<sub>3</sub>(400) peak is roughly coincident with STO(200) substrate peak indicating the in-plane lattice constant of  $\gamma$ -Al<sub>2</sub>O<sub>3</sub> is very close to the STO substrate (3.905 Å). ....70

Figure 5.3. (a) TEM image showing 2.1-nm-thick Al<sub>2</sub>O<sub>3</sub> on TiO<sub>2</sub>-terminated by ALD at 345 °C, (b) TEM image of 2.5-nm-thick Al<sub>2</sub>O<sub>3</sub> on TiO<sub>2</sub>-terminated by ALD at 300 °C, (c) TEM image in <110> projection of 27-nm-thick Al<sub>2</sub>O<sub>3</sub> on TiO<sub>2</sub>-terminated by ALD at 345 °C, and (d) selected- area electron diffraction pattern of 27-nm-thick Al<sub>2</sub>O<sub>3</sub> on TiO<sub>2</sub>-terminated by ALD at 345 °C in the <110> projection, weak spots (arrowed) originate from Al<sub>2</sub>O<sub>3</sub>. ....71

Figure 5.4. (a) Ti 2*p* XP spectra of 25 cycles of Al<sub>2</sub>O<sub>3</sub> grown on TiO<sub>2</sub>-terminated STO by ALD at different temperatures. (b) Angle-resolved XPS of 0.5-nm-thick Al<sub>2</sub>O<sub>3</sub> film grown by ALD on TiO<sub>2</sub>-terminated STO at 345 °C at 30, 50, 70, and 90 ° takeoff angles. (c) and (d) Ti 2*p* XP spectra of Al<sub>2</sub>O<sub>3</sub> layers grown on TiO<sub>2</sub>-terminated STO by ALD at 345 °C with different numbers of ALD cycles. ....73

Figure 5.5. Ti 2*p* XP spectra of TiO<sub>2</sub>-terminated STO substrates after: (a) 5-s exposure to TMA at 345 °C, (b) 5-min exposure to TMA at 345 °C, (c) 5-s exposure to TMA at 300 °C, and (d) 5-min exposure to TMA at 300 °C. ....75

Figure 5.6. (a) Al 2*p* and (b) O 1*s* XP spectra of a TiO<sub>2</sub>-terminated STO substrate after exposure to TMA alone at 345 °C for different times. These spectral features are a good indication of a reaction between TMA and H<sub>2</sub>O to form Ti<sup>3+</sup> and even Ti<sup>2+</sup> and Al<sub>2</sub>O<sub>3</sub>. ....75

Figure 5.7. Thickness and deposition temperature dependent electronic properties of the  $\gamma$ -Al<sub>2</sub>O<sub>3</sub>/STO interface. (a) Thickness and deposition temperature dependence of sheet resistance, R<sub>xx</sub> for the  $\gamma$ -Al<sub>2</sub>O<sub>3</sub>/STO interface conduction at Al<sub>2</sub>O<sub>3</sub> film thicknesses of 1.3 nm, 2.1 nm, 4.3 nm, and 8.5 nm deposited at 345 °C. (b) Hall mobility,  $\mu_{\text{Hall}}$ , and (c) sheet carrier density, n<sub>s</sub>, for the  $\gamma$ -Al<sub>2</sub>O<sub>3</sub>/STO interface conduction at Al<sub>2</sub>O<sub>3</sub> film thicknesses of 1.3 nm, 2.1 nm, and 4.3 nm deposited at 345 °C. ....77

Figure 5.8. Temperature dependent sheet resistance of: (a) 15 cycles ~ 1.3 nm, (b) 25 cycles ~ 2.1 nm, (c) 50 cycles ~ 4.3 nm, and (d) 100 cycles ~ 8.5 nm Al<sub>2</sub>O<sub>3</sub> on TiO<sub>2</sub>-terminated STO by ALD at 345 °C during warm up (red curves) and cool down (black curves) processes. ....78

Figure 6.1. Core level Co 2*p* (a) and O 1*s* (b) XP spectra of an 8-nm ALD CoO film grown on four unit cell STO-buffered Si(001). ....89

Figure 6.2. RHEED images of: (a) a four unit cell STO-buffered Si(001) grown by MBE, (b) a 10-nm ALD-grown TiO<sub>2</sub> on four unit cell STO-buffered Si(001), (c) a 4-nm ALD-grown CoO on four unit cell STO-buffered Si(001), and (d) a 4-nm CoO film on a 10-nm ALD-grown TiO<sub>2</sub> on four unit cell STO-buffered Si(001). All RHEED patterns were taken along <100> direction of STO. ....90

Figure 6.3. 2D AFM images of (a) an 8-nm thick ALD-grown CoO on four unit cell STO-buffered Si(001), and (b) an 8-nm thick ALD-grown CoO on 10-nm thick ALD-grown TiO<sub>2</sub> stack layer on four unit cell STO-buffered Si(001). ....91

Figure 6.4. (a) XRD patterns of a 24-nm thick CoO film on four unit cell STO-buffered Si(001) and rocking curve pattern (inset) of the CoO(002) Bragg peak at a fixed 2θ=42.60°, (b) XRD patterns of a 10-nm thick CoO film on ALD-grown 10-nm TiO<sub>2</sub> stack layer on four unit cell STO-buffered Si(001), (c) XRD patterns of an 8-nm CoO film on a 10-nm ALD STO on four unit cell STO-buffered Si(001). Note: Si(002) peak was not observed in Figure 6.4c. ....93

Figure 6.5. Cross-sectional STEM images of: (a) a 24-nm CoO film on four unit cell STO-buffered Si(001) grown by MBE, and (b) 13-nm CoO film on a 10.8 nm ALD-grown TiO<sub>2</sub> stack layer on four unit cell STO-buffered Si(001). ....94

Figure 6.6. Linear sweep voltammetry (25 mV/s) of CoO(12 nm)/TiO<sub>2</sub>(14 nm)/STO(1.6 nm)/Si ( red curve), CoO(12 nm)/STO(13.6 nm)/Si (blue curve), and TiO<sub>2</sub>(25 nm)/STO(1.6 nm)/Si (black curve). An UV filter that blocked all wavelengths < 420 nm was used as the light source.96

Figure 6.7. Valence band XP spectra for STO (a), TiO<sub>2</sub> (c), and CoO (e), core level XP spectra for STO Ti 2*p* (b), TiO<sub>2</sub> Ti 2*p* (d), and CoO Co 2*p* (f)...98

Figure 6.8. (a) Ball-and-stick model and layer-by-layer projected density of states (pDOS) of the CoO/STO (001) heterostructure. The STO layer is 4 unit cells thick and the CoO layer is 3 unit cells thick with a (2×2) in-plane cell size (dimension = 7.79 Å × 7.79 Å). The type-II antiferromagnetic phase is considered for the CoO layer with spin-up (↑) Co<sup>2+</sup> and spin-down (↓) Co<sup>2+</sup> represented with dark-blue and orange balls. (b) Schematic of band alignment of the Si/STO/CoO (001) heterostructure, generation and separation of electron-hole pair across the interface, and oxidation and reduction of water to form oxygen and hydrogen at the surfaces. (c) Band alignment for two types of heterojunctions CoO/STO and CoO/TiO<sub>2</sub> determined experimentally using *in-situ* high-energy resolution core level and valance band XPS.....101

Figure 7.1: (a) Basic STT-RAM cell structure (Adapted from Ref. 43), (b) A schematic of STT-RAM structure proposed by NASCENT.....109

Figure 7.2: Co 2*p* XP-spectra of 3-nm-thick CoO films on SiO<sub>2</sub>/Si and MgO(001) substrates grown by ALD at ~ 180 °C [Fig. 7.2a (red color) and Fig. 7.2b (blue color), respectively]. RHEED images of a 3-nm-thick CoO film grown on SiO<sub>2</sub> (Fig. 7.2b) and a 15-nm-thick CoO film grown on MgO(001) (Fig. 7.2c).....113

- Figure 7.3: (a) Co  $2p$  XP-spectra of 200 cycles of CoO films on single crystal MgO(001) substrates grown by ALD at  $\sim 270$  (black color), 305 (red color), and 345  $^{\circ}\text{C}$  (blue color). (b) and (c) RHEED images of 200 cycles of CoO films on MgO(001) grown by ALD at 345 and 305  $^{\circ}\text{C}$ , respectively. ....114
- Figure 7.4: (a) C  $1s$  XP-spectra of a 200 ALD cycles of CoO film on MgO(001) grown at 345  $^{\circ}\text{C}$  as-deposited (red color) and after a 15 min vacuum anneal at 500  $^{\circ}\text{C}$  (blue color). (b) C  $1s$  XP-spectra of an as-deposited 200 ALD cycles of CoO film on MgO(001) grown at 305  $^{\circ}\text{C}$ . .....115
- Figure 7.5: (a) Co  $2p$  and (b) O  $1s$  XP-spectra after 300 ALD cycles of CoO film on 50-nm-thick poly(trimethylsilylstyrene) on amorphous MgO/SiO<sub>2</sub>/Si.116
- Figure 7.6: (a) Co  $2p$  XP-spectra of a 4.5-nm-thick as-deposited CoO film on MgO(001) substrate grown by ALD at 180  $^{\circ}\text{C}$  (red color) and the CoO film after exposing to Hg UV light for 30 min at room temperature (blue color). The Co  $2p$  XP-spectrum shows characteristic strongly suppressed shake-up satellite peaks at 6 eV and +22 eV as compared to CoO indicating the formation of Co<sub>3</sub>O<sub>4</sub>. (b) and (c) are RHEED images of the as-deposited CoO and after exposing to Hg UV light for 30 min at room temperature, respectively. ....117
- Figure 7.7: (a) Co  $2p$ , (b) Si  $2p$ , and (c) O  $1s$  XP-spectra of a 4-nm-thick CoO film grown on four unit cell SrTiO<sub>3</sub>-buffered Si(001) as-deposited (red color), after a 30 min vacuum anneal at 500  $^{\circ}\text{C}$  (green color), and after an additional 30 min vacuum anneal at 550  $^{\circ}\text{C}$  (black color). .....119

Figure 7.8: (a) Co 2*p* and (b) O 1*s* XP-spectra of a 4-nm-thick CoO film grown on ~ 15-nm-thick SrTiO<sub>3</sub>-buffered Si(001) as-deposited (red color), after a 30 min vacuum anneal at 500 °C (green color), and after an additional 30 min vacuum anneal at 550 °C (black color).....121

Figure 7.9: (a) Co 2*p* XP-spectra of: an as-deposited 3-nm-thick CoO film on SiO<sub>2</sub> grown by ALD at 180 °C (red color), the CoO film after a 30 min vacuum anneal at 500 °C (blue color), the CoO film after a deposition of 3-nm-thick Sr on it (green color), and the Sr/CoO/SiO<sub>2</sub>/Si heterostructure after a 30 min vacuum anneal at 500 °C. (b) Sr 3*d* XP-spectra of the Sr/CoO/SiO<sub>2</sub>/Si heterostructure as-deposited (green color) and after a 30 min vacuum anneal at 500 °C (black color).....123

Figure 7.10: (a) Co 2*p* XP-spectra of: an as-deposited 3-nm-thick CoO film on SiO<sub>2</sub> grown by ALD at 180 °C (red color), after a deposition of 3-nm-thick Sr on the CoO/SiO<sub>2</sub> (blue color), and the Sr/CoO/SiO<sub>2</sub>/Si heterostructure after a 30 min vacuum anneal at 500 °C. (b) Al 2*p* XP-spectra of the Al/CoO/SiO<sub>2</sub>/Si heterostructure as-deposited (blue color) and after a 30 min vacuum anneal at 500 °C (green color). .....125

Figure 7.11: Magnetization of: (a) SrO/Co/SiO<sub>2</sub>/Si and Al<sub>2</sub>O<sub>3</sub>/Co/SiO<sub>2</sub>/Si heterostructures as a function of applied magnetic field measure at 300K. The sample size of 10×5×0.5 mm<sup>3</sup> was used for the measurement. The applied magnetic field was parallel to the substrates.....126

Figure 7.12: (a) Co 2*p* XP-spectra of: a 3-nm-thick CoO on MgO(001) grown by ALD at 180 °C (red color), after a deposition of a 3-nm-thick Sr on top of the 3-nm CoO (blue color), and after a 30 min vacuum anneal of the Sr/CoO/MgO(001) heterostructures at 500 °C. (b) Co 2*p* XP-spectra of: a 15-nm-thick CoO on MgO(001) grown by ALD at 180 °C (red color), after a deposition of a 3-nm-thick Sr on top of the 15-nm CoO (blue color), and after a 30 min vacuum anneal of the Sr/CoO/MgO(001) heterostructures at 500 °C.....128

Figure 7.13: Magnetization of: SrO/Co/MgO(001) (blue color), and SrO/Co/CoO/MgO(001) (red color) heterostructures as a function of applied magnetic field measured at 300K. The sample size of 10×5×0.5 mm<sup>3</sup> was used for the measurement. The magnetic field was applied parallel to the substrates.....129

# Chapter 1: Introduction and dissertation overview

## 1.1. HISTORY OF ATOMIC LAYER DEPOSITION

Atomic layer deposition (ALD) is not a new technique. The principle of ALD was published under the name of “Molecular Layering” by the Soviet Union in the 1960s.<sup>1</sup> Atomic layer epitaxy (ALE) processes and reactors were invented by Dr. Tuomo Suntola in Finland in 1970s.<sup>1</sup> Dr. Tuomo Suntola and coworkers developed a scientific idea that led to a true thin film deposition technique and applied that technique for an industrial use in electroluminescent flat-panel display manufacturing.<sup>2,3</sup> The need for high quality thin films in electroluminescent (TFEL) flat-panel displays motivated the development of the ALE technology. At that time, the ALE was used with elemental precursors and that is why it named “atomic”. The precursors were converted to molecular precursors later to expand material selection.<sup>1</sup> The word “epitaxy” is from the Greek roots *epi*, meaning “above” and *taxis*, meaning “in an ordered manner.” Dr. Suntola and his team produced TFEL displays at the industrial scale by ALE using manganese-doped zinc sulfide luminescent layers and aluminum-titanium oxide.<sup>1</sup> TFEL was the only industrial application of ALD at that time.

In the late 1990s, the continued shrinkage of electronic device feature sizes required introduction of new materials into microelectronics. In addition, new deposition techniques were necessary in integrated circuit technology since materials needed to be deposited with atomic level accuracy, to be uniform over the size-increasing wafers, and to be conformal over the three-dimensional (3D) device structures.<sup>4</sup> Since then, new attention and interest were paid to ALD. The research activities focusing on the development of processes to manufacture high- $\kappa$  dielectric materials, metals, and

materials for barrier layers using ALD have been significantly increased.<sup>4</sup> The term “ALD” has been used approximately back to 2000, prior to 2000 ALE was more common.<sup>5</sup> The transition from ALE to ALD occurred as the result of the fact that most films grown were not epitaxial to their underlying substrates.<sup>5</sup> ALD started being applied to dynamic random access memory (DRAM) early in this century. Another revolutionary development of ALD in microelectronics was the mass production of microprocessors, which was initiated with the production of Penryn in 2007 by Intel Corporation.<sup>6</sup> Since then ALD has evolved into a standard process in the semiconductor industry. Nowadays, many other types of memory chips also employ ALD processes for various applications.<sup>4</sup> The semiconductor roadmap is coming to an end in a very near future because of the limits of the conventional electronic materials. For continued progress, the future of electronic materials will embrace as yet undefined paradigms.<sup>5</sup> ALD will certainly be part of the new paradigms because of its ability to control deposition atomically and to deposit conformally on the very high aspect ratio features.<sup>5</sup> In addition to the semiconductor industry, ALD processes have been developed to deposit a wide variety of materials for many other applications, such as energy storage, photovoltaic devices, and biomedical applications because of its advantages compared to other deposition techniques.<sup>5</sup>

## **1.2. PRINCIPLE AND APPLICATIONS**

A general ALD process is presented in Figure 1.1 showing two surface reactions occur and deposit a binary compound of a thin film. These two surface reactions are self-limiting. The reactions only occur on a finite number of surface reactive sites since there are only a finite number of surface reactive sites. No reactive sites are left after each of these two surface reactions, resulting in no more than monolayer of atoms deposited after

each of the two reactions. The advantage of ALD is precise thickness control at up to the monolayer level.<sup>5</sup> The self-limiting behavior leads to excellent step coverage and conformal deposition on high aspect ratio structures. Because no surface sites are left behind during film growth, the films tend to be continuous and pinhole-free. These are very important for deposition on 3D structure wafers and the deposition of excellent dielectric films. There have been many reviews focusing on the applications of ALD to microelectronic and nanotechnology recently.<sup>5,7-11</sup>

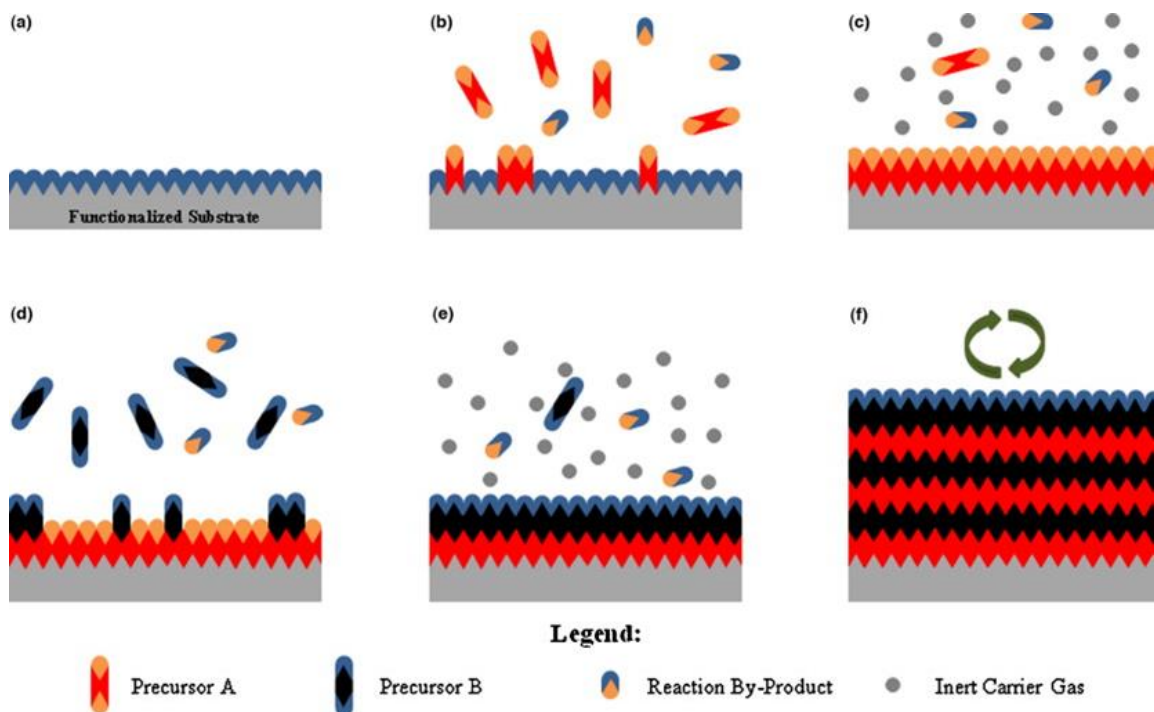


Figure 1.1. Schematic of ALD process. (a) Substrate surface has natural functionalization or is treated to functionalize the surface. (b) Precursor A is pulsed and reacts with surface. (c) Excess precursor and reaction by-products are purged with inert gas carrier. (d) Precursor B is pulsed and reacts with surface. (e) Excess precursor and reaction by-products are purged with inert carrier gas. (f) Steps 2–5 are repeated until the desired material thickness is achieved (Reprinted with permission from Ref. 7).

### 1.2.1. ALD of high- $\kappa$ materials for Metal Oxide Semiconductor Field Effect Transistor (MOSFET) application

Silicon dioxide ( $\text{SiO}_2$ ) has been used as a gate oxide of MOSFETs for decades. The great advantage of  $\text{SiO}_2$  was that it can be grown by high temperature thermal oxidation of the Si substrate.  $\text{SiO}_2$  is formed uniformly and conformally. The  $\text{SiO}_2/\text{Si}$  interface performs a high quality in term of electrical behaviors. Therefore,  $\text{SiO}_2$  with a dielectric constant of 3.9 has dominated the semiconductor industry. The down-scaling of electronic devices below 45 nm requires a  $\text{SiO}_2$  layer thinner than 1.2 nm. That thickness allows direct tunneling, a large leakage current flows across the  $\text{SiO}_2$  layer. In order to continue scaling the devices to the 45 nm node and below, semiconductor device makers have implemented higher- $\kappa$  dielectric and metal gates stack in the MOSFET. The gate oxide in a MOSFET can be modeled as a parallel capacitor. Ignoring quantum mechanics and depletion effects from the gate and silicon substrate, respectively, the capacitance of this capacitor can be estimated by  $C = k\epsilon_0 A/t$ ; where  $A$  is the capacitor area,  $k$  (or  $\kappa$ ) is the dielectric constant of gate oxide material,  $\epsilon_0$  is vacuum permittivity,  $t$  is the thickness of gate oxide.<sup>7</sup>

As discussed above, the leakage current constrained further shrinking of  $\text{SiO}_2$  layer thickness,  $t$ ; an alternative method to increase the gate capacitance is improving the  $\kappa$  value by replacing  $\text{SiO}_2$  with higher- $\kappa$  materials. Representatives of high- $\kappa$  materials include SiN, SiON,  $\text{Al}_2\text{O}_3$ ,  $\text{HfO}_2$ ,  $\text{ZrO}_2$ ,  $\text{HfZrO}_4$ , rutile  $\text{TiO}_2$ , and perovskite-type oxides. The deposition of these materials has been studied extensively by ALD and chemical vapor deposition (CVD). The ALD window temperature is usually lower than CVD temperature, making it to be more desirable method for a lower thermal budget process. Another key technology for using ALD is related to the control of gate thickness. The thickness of high- $\kappa$  dielectric layer in modern chips is lower than 5 nm, meaning that the

thickness variation by 0.5 nm corresponds to more than 10% of the total thickness.<sup>4</sup> In 2007, Intel became the first chip makers to announce that Hf-based high- $\kappa$  dielectric was used in conjunction with a metallic gate for components integrated on the 45-nm transistor technology node in complementary metal oxide semiconductor (CMOS) manufacturing, and shipped it in the 2007-processor series codenamed Penryn.<sup>6</sup> At the same time, IBM announced the plans of transition to Hf-based materials for a higher- $\kappa$  material. One problem of using Hf- and Zr-based materials is that these materials become polycrystalline during dopant activation annealing. The polycrystalline structures have higher leakage compared to amorphous films. Leakage current again became problematic. In addition, the interface of these oxides and Si are not as good as the SiO<sub>2</sub>/Si interface. To overcome these difficulties for next generations of MOSFET devices, crystalline perovskite oxides with higher- $\kappa$  values, such as SrTiO<sub>3</sub> and LaAlO<sub>3</sub> were proposed for beyond Hf- and Zr-based materials.<sup>12,13</sup>

There has been extensive work focusing on the integration of SrTiO<sub>3</sub> and LaAlO<sub>3</sub> on Si by different growth methods.<sup>12-16</sup> The dielectric constants of LaAlO<sub>3</sub> and SrTiO<sub>3</sub> thin films have been reported as  $\sim 30$  and  $\sim 100$ , respectively. With a negligible conduction band offset with the semiconductor (*e.g.*, Si and Ge), the employment of SrTiO<sub>3</sub> as a gate oxide produces very large leakage current. In contrast, even with a lower dielectric constant, LaAlO<sub>3</sub> has been listed as a potential candidate to replace Hf- and Zr-based materials as a gate oxide because of its large band gap (5.6 eV) and acceptable conduction band and valence band offsets with Si and Ge ( $>1\text{eV}$ ). The ALD self-limiting nature of the surface reaction leads to excellent step coverage and is conformal on high aspect ratio structures. Because no surface active sites are left behind during the film growth process, the films tend to be very continuous and pinhole-free. This advantage of ALD is very important for dielectric applications. Recently, the growth of higher- $\kappa$

materials using ALD has been reported extensively.<sup>14-20</sup> Attempts to grow crystalline materials on semiconductors (*e.g.*, Si and Ge) have been demonstrated by many groups using different growth techniques. To date, the growth of high- $\kappa$  crystalline oxides on Si directly using ALD has not been succeeded, however the growth of high- $\kappa$  crystalline oxides on other semiconductors, such as GaAs and Ge has been demonstrated by the Gordon group at Harvard University<sup>21</sup> and the Ekerdt group at The University of Texas at Austin.<sup>22,23</sup> This opens the door to the integration of multi-functional crystalline oxides on semiconductors using only ALD for future electronic applications.

### **1.2.2. ALD for DRAM cell capacitors**

The down-scaling of DRAM technology does not allow sufficient design space for maintaining performance with smaller cell capacitance. ALD has met challenging requirements for the deposition of high quality dielectrics to fabricate trench capacitors for DRAM. Like gate oxide dielectrics, the ALD process has implemented into DRAM dielectric fabrication.

#### ***1.2.2.1. ALD of $Al_2O_3$ for DRAM dielectric***

$Al_2O_3$  thin films have been studied extensively as a dielectric material in DRAM cell capacitors. The dielectric constant of  $Al_2O_3$  is relatively small ( $\sim 9$ ) compared to  $HfO_2$ - and  $ZrO_2$ -based materials, the thin films of  $Al_2O_3$  have a very good leakage barrier due to its large band gap (8.8 eV) and amorphous nature. Because of its ideal ALD behavior,  $Al_2O_3$  is one of most studied materials grown by ALD and was used as a dielectric material in DRAM devices. ALD of  $Al_2O_3$  provides very smooth and conformal films on 300-mm structure wafers with high aspect ratios. Capacitors employing  $Al_2O_3$  thin films as a dielectric were developed for 100–150 nm design rule,

however for the < 100 nm design rule where the equivalent of thickness requires less than 2 nm, the use of Al<sub>2</sub>O<sub>3</sub> as an only DRAM dielectric material becomes inadequate.<sup>4</sup>

#### ***1.2.2.2. ALD of higher- $\kappa$ oxides for DRAM dielectric***

ALD of HfO<sub>2</sub>- and ZrO<sub>2</sub>-based materials are being employed in current DRAM technology. The band-gap of these oxides ranging from 5.5–5.8 eV, which is lower than that of SiO<sub>2</sub> and Al<sub>2</sub>O<sub>3</sub> but still enough to have acceptable electron and hole barriers using most electrode materials. In some cases, Al<sub>2</sub>O<sub>3</sub> is used accompanying with HfO<sub>2</sub> and ZrO<sub>2</sub> as dielectric materials in the metal-insulator-metal capacitor to improve the leakage current problem.<sup>4</sup> ALD growth of HfO<sub>2</sub> and ZrO<sub>2</sub> thin films using different precursors is still under investigation. Even though the dielectric performance of the HfO<sub>2</sub>- and ZrO<sub>2</sub>-based materials is acceptable, higher- $\kappa$  dielectric materials must be pursued for future shrinking of DRAM devices. Promising candidates for next generation DRAM dielectrics are rutile-TiO<sub>2</sub> with a dielectric constant of ~ 80–100 and perovskite-based materials such as SrTiO<sub>3</sub>, BaTiO<sub>3</sub>, and (Ba,Sr)TiO<sub>3</sub> with an extremely high dielectric constant (hundreds to thousands). There have also been many studies on perovskite-structures using ALD for DRAM application.<sup>24,25</sup>

#### **1.2.3. ALD for other applications**

In addition to its applications for MOSFET and DRAM, ALD is also receiving a great attention for its ability to deposit highly conformal film with a monolayer level control. The ALD film conformality makes it become one of the most promising thin film deposition techniques for back end of line (BEOL) process.<sup>4</sup> While ALD of high- $\kappa$  gate oxide has been implemented in the front end of line process, ALD is not yet a standard process in BEOL process. However, it is expected to have an important role in very near future BEOL process for logic devices.<sup>4</sup> ALD has also been paid attention for the

deposition of ultra-thin insulating layers in the magnetic tunnel junction (MTJ), with a thickness of a few nanometers. The growth of metals, such as Co or Fe by ALD for the magnetic layers in MTJ structure is a difficult process.<sup>26-28</sup> In this dissertation, we report methods to form magnetic Co thin films via an ALD process. There are also numerous applications for ALD in energy storage, photovoltaic devices, and memristor applications as discussed in most recent review articles.<sup>7-11</sup>

### 1.3. OVERVIEW OF THIS DISSERTATION

My research explored the monolithic integration of crystalline perovskite oxide films with Si(001) using molecular beam epitaxy (MBE) and ALD techniques. We have successfully demonstrated monolithic integration of high- $\kappa$  LaAlO<sub>3</sub>, rocksalt CoO, and *c*-oriented polarization BaTiO<sub>3</sub> (BTO), and heterostructures on Si(001). Using the combined MBE-ALD techniques, four unit cells of STO were grown directly on Si(001) by MBE and transferred *in-situ* into the ALD chamber for further depositions. The integration of oxide thin films on Si(001) using the MBE-ALD technique allows us to maintain clean oxide/Si(001) interfaces since low temperatures (180 – 250 °C) were maintained during the ALD deposition. Chapters 2 and 3 present the epitaxial growth of LaAlO<sub>3</sub> on SrTiO<sub>3</sub>(001) and SrTiO<sub>3</sub>-buffered Si(001) substrates using ALD. The crystalline and epitaxial LaAlO<sub>3</sub> films on SrTiO<sub>3</sub>-buffered Si(001) demonstrates a chemical method to integrate epitaxial high- $\kappa$  LaAlO<sub>3</sub> films on Si(001). Chapter 4 presents the integration of *c*-axis oriented ferroelectric BaTiO<sub>3</sub> on SrTiO<sub>3</sub>-buffered Si(001). The goal of this work is to grow the ferroelectric field effect transistor (FeFET) heterostructure..

In Chapter 5, the growth of  $\gamma$ -Al<sub>2</sub>O<sub>3</sub> on TiO<sub>2</sub>-terminated SrTiO<sub>3</sub> was demonstrated using ALD at temperatures higher than 300 °C. *In-situ* x-ray photoelectron spectroscopy reveals the presence of Ti<sup>3+</sup> feature at the  $\gamma$ -Al<sub>2</sub>O<sub>3</sub>/SrTiO<sub>3</sub> interface. Conductivity at the interface was found to be proportional to the amount of Ti<sup>3+</sup> species. The formation of a quasi-two dimensional electron gas (2-DEG) was found at the  $\gamma$ -Al<sub>2</sub>O<sub>3</sub>/STO interface. This work enables a possibility to form all-oxide devices for electronic applications.

Chapter 6 presents the ALD epitaxial growth of rock salt CoO on SrTiO<sub>3</sub> and TiO<sub>2</sub> on Si. The band alignment measurement of CoO/SrTiO<sub>3</sub>/Si and CoO/TiO<sub>2</sub>/SrTiO<sub>3</sub>/Si heterostructures is performed using x-ray photoelectron spectroscopy and is compared to electronic structure calculations using density functional theory. Both types of heterostructures demonstrate water photooxidation activity under visible light illumination. The growth of CoO on SiO<sub>2</sub> and MgO(001) are also presented in Chapter 7. While the CoO films grown on SiO<sub>2</sub>/Si are polycrystalline, the CoO films grown on single crystal substrate MgO(001) are crystalline and epitaxial. Attempts to grow CoO at temperatures higher than 305 °C result in ~ 31 % C-incorporated Co films. We demonstrate the reduction of CoO forming carbon-free Co metal using Al and Sr metals to scavenge oxygen from CoO. The room temperature ferromagnetic behavior of the resultant Co films is observed. However, further studies are needed to explore the change in coercivity of the Co films and the ability to control it. The reduction of CoO to form Co metal is performed using scavenger (*e.g.*, Sr and Al), and magnetization of resultant Co thin film is presented. Chapter 8 presents a research summary and recommendations for further work.

#### 1.4. REFERENCES

- <sup>1</sup>G. N. Parsons, J. W. Elam, S. M. George, S. Haukka, H. Jeon, W. M. M. Kessels, M. Leskelä, P. Poodt, M. Ritala, and S. M. Rossnagel, *J. Vac. Sci. Technol. A* **31**, 050818 (2013).
- <sup>2</sup>T. Suntola, J. Antson, U.S. Patent 4,058,430, 1977.
- <sup>3</sup>T. Suntola, A. Pakkala, S. Lindfors, U.S. Patent 4,389,97, 1983.
- <sup>4</sup>C. S. Hwang, *Atomic layer deposition for semiconductors*, Springer (2014).
- <sup>5</sup>S. M. George, *Chem. Rev.* **110**, 111–131 (2010).
- <sup>6</sup>M. T. Bohr, R. S. Chau, T. Ghani and K. Mistry, <http://spectrum.ieee.org/semiconductors/design/the-highk-solution>, (2007)
- <sup>7</sup>R. W. Johnson, A. Hultqvist, and S. F. Bent, *Mater. Today* **17**, 236–246 (2014).
- <sup>8</sup>M. Leskelä, M. Ritala, and O. Nilsen, *MRS Bulletin* **36**, 877–884 (2011).
- <sup>9</sup>V. Miikkulainen, M. Leskelä, M. Ritala, and R. L. Puurunen, *J. Appl. Phys.* **113**, 021301 (2013).
- <sup>10</sup>R. D. Clark, *Materials* **7**, 2913–2944 (2014).
- <sup>11</sup>J. S. Ponraj, G. Attolini, and M. Bosi, *Crit. Rev. Solid State Mater. Sci.* **38**, 203–233 (2013).
- <sup>12</sup>J. W. Reiner, A. M. Kolpak, Y. Segal, K. F. Garrity, S. Ismail-Beigi, C. H. Ahn, and F. J. Walker, *Adv. Mater.* **22**, 2919–2938 (2010).
- <sup>13</sup>J. Robertson, *Rep. Prog. Phys.* **69**, 327–396 (2006).
- <sup>14</sup>J. W. Reiner, A. Posadas, M. Wang, M. Sidorov, Z. Krivokapic, F. J. Walker, T. P. Ma, and C. H. Ahn, *J. Appl. Phys.* **105**, 124501 (2009).

- <sup>15</sup>M. D. McDaniel, A. Posadas, T. Q. Ngo, A. Dhamdhare, D. J. Smith, A. A. Demkov, and J. G. Ekerdt, *J. Vac. Sci. Technol. A* **31**, 01A136 (2013).
- <sup>16</sup>T. Q. Ngo, M. D. McDaniel, A. Posadas, A. A. Demkov, and J. G. Ekerdt, *Proc. of SPIE*, **8987**, 898712 (2014).
- <sup>17</sup>T. Q. Ngo, A. Posadas, M. D. McDaniel, D. A. Ferrer, J. Bruley, C. Breslin, A. A. Demkov, and J. G. Ekerdt, *J. Cryst. Growth*, **363**, 150–157 (2013).
- <sup>18</sup>R. Droopad, Z. Yu, H. Li, Y. Liang, C. Overgaard, A. Demkov, X. Zhang, K. Moore, K. Eisenbeiser, M. Hu, J. Curless, and J. Finder, *J. Cryst. Growth* **251**, 638–644 (2003).
- <sup>19</sup>M. Choi, A. Posadas, R. Dargis, C.-K. Shih, A. A. Demkov, D. H. Triyoso, N. D. Theodore, C. Dubourdieu, J. Bruley, and J. Jordan-Sweet, *J. Appl. Phys.* **111**, 064112 (2012).
- <sup>20</sup>D. H. Triyoso, R. I. Hegde, J. M. Grant, J. K. Schaeffer, D. Roan, B. E. White, and P. J. Tobin, *J. Vac. Sci. Technol. B* **23**, 288 (2005).
- <sup>21</sup>X. Wang, L. Dong, J. Zhang, Y. Liu, P. D. Ye, and R. G. Gordon, *Nano Lett.* **13**, 594–599 (2013).
- <sup>22</sup>M. D. McDaniel, T. Q. Ngo, A. Posadas, C. Hu, S. Lu, D. J. Smith, E. T. Yu, A. A. Demkov, and J. G. Ekerdt, *Adv. Mater. Interfaces*, **1**, 1400081 (2015).
- <sup>23</sup>M. D. McDaniel, C. Hu, S. Lu, T. Q. Ngo, A. Posadas, A. Jiang, D. J. Smith, E. T. Yu, A. A. Demkov, and J. G. Ekerdt, *J. Appl. Phys.* **117**, 054101 (2015).
- <sup>24</sup>M. Vehkamäki, T. Hatanpää, T. Hänninen, M. Ritala, M. Leskelä, *Electrochem. Solid-State Lett.* **2**, 504 (1999).
- <sup>25</sup>M. Vehkamäki, T. Hänninen, M. Ritala, M. Leskelä, T. Sajavaara, E. Rauhala, J. Keinonen, *Chem. Vapor Deposition* **7**, 75 (2001).
- <sup>26</sup>R. Mantovan, M. Georgieva, M. Perego, H. L. Lu, S. Cocco, A. Zenkevich, G. Scarel, and M. Fanciulli, *Acta Physica Polonica A*, **112**, 1271–1280 (2007).

<sup>27</sup>B. S. Lim, A. Rahtu, and R. G. Gordon, *Nat. Mater.* **2**, 749 (2003).

<sup>28</sup>H. Kim, *J. Vac. Sci. Technol. B* **21**, 2231 (2003).

## **Chapter 2: Epitaxial growth of LaAlO<sub>3</sub> on SrTiO<sub>3</sub>-buffered Si(001) substrates by atomic layer deposition**

### **2.1. INTRODUCTION**

The ability to grow epitaxial oxides on Si has presented opportunities to extend and enhance silicon technology.<sup>1-5</sup> The direct deposition of epitaxial strontium titanate [SrTiO<sub>3</sub>] (STO) on Si(001),<sup>1,2,6,7</sup> has opened up a route to the integration of functional oxides such as, ferroelectric, ferromagnetic, high- $\kappa$ , and superconducting complex oxides onto silicon, with the potential towards the development of single-wafer integration of devices and sensors based on these complex oxides with metal-oxide-semiconductor field effect transistors (MOSFETs).<sup>1-13</sup> Single crystal lanthanum aluminate [LaAlO<sub>3</sub>] (LAO) was originally developed as a substrate for the deposition of magnetic, ferroelectric, and high-temperature superconductor thin films.<sup>14-19</sup> However, due to challenges in the crystal growth process, single crystals of LAO suffer from being limited to small sizes (<75 mm) and also exhibit heavy twinning,<sup>20</sup> which can affect the quality of films grown on it. The ability to grow single crystalline LAO on silicon, which is available in large sizes (300 mm) is a promising method to make large area, twin-free LAO substrates.

Single crystal LAO, which has a dielectric constant of 25–30,<sup>21</sup> and a wide band gap of 6.5 eV is also a potential candidate for use as a gate dielectric in next generation MOSFETs. The International Technology Roadmap for Semiconductors lists epitaxial complex oxides such as LAO as a possible replacement material for amorphous oxides based on ZrO<sub>2</sub> or HfO<sub>2</sub> for the sub-22 nm technology generation and beyond, where equivalent oxide thicknesses less than 0.5 nm are required.<sup>22,23</sup>

More recently, the epitaxial interface between LAO and STO has been found to exhibit a two-dimensional electron gas with a high enough mobility to display quantum oscillations in magnetotransport,<sup>24,25</sup> as well as superconductivity.<sup>26-29</sup> Devices based on this phenomenon have already been proposed.<sup>30</sup> The ability to integrate these devices on the standard silicon technology platform may enable their commercialization.

LAO has been previously deposited on Si using chemical vapor deposition,<sup>31-33</sup> pulsed laser deposition (PLD)<sup>34,35</sup> and molecular beam epitaxy (MBE).<sup>36-38</sup> Unlike STO, direct epitaxial growth of LAO films on Si(001) has not yet been demonstrated, even though the lattice mismatch is relatively small (1.3%). LAO films deposited directly on Si remain amorphous even after annealing at high temperature. As a result, single crystal LAO is grown on Si using STO-buffered Si(001) substrates. Epitaxial LAO films on STO-buffered Si(001) substrates have been grown by molecular beam epitaxy (MBE) at high temperature ( $> 600$  °C).<sup>39-41</sup> However, the STO/Si interface is not stable above 600 °C, and oxygen present in the MBE-deposited STO can lead to the formation of an amorphous SiO<sub>x</sub>, or silicate layer at the STO/Si interface at high temperature.<sup>40-43</sup>

Growth of oxide films by ALD may offer several advantages when compared to MBE and PLD, such as uniform deposition over large area substrates, good conformality and compatibility with current processing tools. The use of ALD to deposit complex oxides has been reported,<sup>44-47</sup> including amorphous LAO directly deposited on Si. We demonstrate a relatively low-temperature method of forming epitaxial LAO films on STO-buffered Si(001) by ALD with little ( $<1$  nm) amorphous interfacial layer. In this study, four unit cells of STO grown on Si(001) substrates by MBE were used as a surface template for LAO growth by ALD. Crystalline LAO films were formed after post-deposition annealing at 600 °C in vacuum ( $10^{-9}$  Torr) for 2 h.

## 2.2. EXPERIMENTAL

The ALD system is a custom-built, hot-wall stainless steel rectangular 20-cm long chamber, with a reactor volume of  $460 \text{ cm}^3$ .<sup>48</sup> The 0.5 mm-thick substrates were cut into  $20 \times 20 \text{ mm}^2$  squares from n-type Si(001) wafers. The substrates were ultrasonically cleaned with acetone, isopropyl alcohol, and deionized water for 15 min each, followed by UV/ozone treatment for 15 min to remove residual carbon contamination. The wafers were loaded into the MBE chamber where four unit cells of STO were deposited on Si(001) using a variation of the Motorola-developed process,<sup>49</sup> as described in more detail elsewhere.<sup>7,48</sup>

For LAO growth, tris(N,N'-diisopropylformamidinate)-lanthanum and trimethylaluminum (TMA) were used as precursors for La and Al, respectively, and water was used as the oxidant. The La precursor was maintained at  $137 \text{ }^\circ\text{C}$ , while the Al precursor and water were maintained at room temperature ( $26 \text{ }^\circ\text{C}$ ). The Al and water dosing were limited by an in-line needle valve. The substrate temperature was maintained at  $250 \text{ }^\circ\text{C}$  throughout the deposition. Substrate temperature was monitored with a reference thermocouple in the ALD chamber that was calibrated against an instrumented wafer. Ultrahigh purity argon was used as a purge/carrier gas.

To determine ALD conditions that produce the correct stoichiometry, amorphous LAO films were grown on Si(001) with native oxide. The *in-situ* VG Scienta R3000 X-ray photoelectron spectroscopy (XPS) system was used to determine the film composition. A single-crystal LAO substrate from CrysTec, where the La:Al stoichiometry was assumed to be 1:1, was used as a standard for the La and Al peak area ratio. The peak area ratio of La  $3d_{5/2}$ :Al 2p was found experimentally to be 32.89:1. The La:Al ratio in the LAO films grown by ALD was adjusted by changing either the La dosing time and/or the cycle ratio  $x\text{La}/y\text{Al}$ , using a saturating dose of Al. Our LAO films

were grown using an  $x = 3$  and  $y = 2$  La:Al cycle ratio in which the substrates were dosed with 3 cycles of the La precursor followed by 2 cycles of the Al precursor (noted as a super-cycle), resulting in a slightly La rich film (1.1:1.0 La:Al). Each La cycle consisted of a 2 sec dose of the La precursor, a 10 sec purge of Ar, a 1 sec dose of water and a 10 sec purge of Ar. Each Al cycle consisted of a 0.5 sec dose of the Al precursor, a 15 sec purge of Ar, a 1 sec dose of water and a 10 sec purge of Ar. These same dosing/purging times and cycle ratio were used to grow LAO on STO-buffered Si(001) substrates.

The as-deposited LAO films were annealed in vacuum ( $1 \times 10^{-9}$  Torr) at a temperature range of 500–750 °C to determine the optimum annealing conditions. The annealing chamber temperature is the reading of a thermocouple situated ~3 mm on the backside of the disc-shaped ceramic heater of roughly the same diameter as the substrate holder. During annealing, the substrate is placed ~1 cm in front of the heater with the entire assembly located inside a tantalum shield to keep the radiation confined to the substrate. Film thickness was determined by X-ray reflectivity (XRR). The growth rate of the LAO films on STO-buffered Si (001) under our growth conditions was found to be  $0.50 \pm 0.01$  nm/super-cycle. *In-situ* XPS was used to study the effect of annealing on the STO/Si interface. For these interface studies, a 2.5 nm LAO film was grown on STO-buffered Si(001). XPS measurements were taken before ALD deposition, after deposition, and after annealing. The LAO film crystallinity and orientation were determined by reflection high energy electron diffraction (RHEED) and X-ray diffraction (XRD). XRR and XRD were conducted with a Bruker-AXS D8 Advance Powder Diffractometer using a sealed tube Cu K $\alpha$  radiation source. Veeco Multimode V atomic force microscopy (AFM) was used to determine the root-mean-square surface roughness of the film. Cross-section transmission electron microscopy (TEM) was used to confirm the crystallinity and overall quality of the LAO/STO/Si stack. The TEM observations

were carried out in FEI Tecnai F20 and TITAN instruments. The samples were prepared by focussed ion beam (FIB) milling. To avoid amorphization of the LAO by the electron or ion beam, the surface was first coated with an amorphous C film using Sharpie ink (~100 nm) followed by a Pt overlayer using the Gas-Injection system initially by the electron beam (~150 nm) then by the Ga ion beam (~500 nm). The TEM lamellae were thinned to electron transparency (~50 nm) using a 30kV Ga<sup>+</sup> FIB and cleaned with a final 5 kV beam to minimize sample damage. The samples were transferred *ex-situ* to an amorphous C supporting grid.

### 2.3. RESULTS AND DISCUSSION

The deposition of Al<sub>2</sub>O<sub>3</sub> was done on Si(001) with a native oxide at 250 °C to establish TMA dosing conditions. The same Al<sub>2</sub>O<sub>3</sub> growth rate was found for Al dosing times of 0.5, 1, and 2 sec. This confirmed the ALD growth of Al<sub>2</sub>O<sub>3</sub> using TMA and water was self-limiting as expected. The Al dosing time of 0.5 sec was chosen to grow LAO films. The growth of LAO films was first attempted using a 1:1 La:Al cycle ratio and 1 sec dose of the La precursor; *in-situ* XPS analysis revealed an atomic ratio of 0.65:1 La:Al. The La dosing time was then increased from 1 sec to 4 sec, however the LAO films were Al rich. The cycle ratio  $x\text{La}/y\text{Al}$  and the La dosing time were changed to determine conditions for a stoichiometric LAO film. This study led to the 3 La cycles followed by 2 Al cycles with a 2 sec La precursor dose, and a 0.5 sec Al precursor dose that is used to grow the LAO films on STO reported herein. These growth conditions result in near stoichiometric LAO films (1.1:1 La:Al).

Figures 2.1(a) and 2.1(b) present the RHEED patterns of a typical four-unit cell STO-buffered Si(001) substrate grown by MBE, taken along <100> and <110>

directions, respectively, showing that the STO layer is crystalline with an atomically flat surface. This four-unit cell STO template (thickness of 1.5 nm) was transferred to the ALD chamber *in vacuo* and exposed to 20 super-cycles of LAO that consisted of 60 cycles of La and 40 cycles of Al at 250 °C. After ALD growth, the film was transferred back to the MBE chamber to check the RHEED pattern (not shown) of the as-deposited LAO, which consistently showed that the as-deposited films were amorphous. The LAO film was then transferred to the annealing chamber and heated to 600 °C in vacuum for 2 h. The RHEED patterns in Figures 2.1(c) and 2.1(d) (taken along  $\langle 100 \rangle$  and  $\langle 110 \rangle$  directions) exhibit sharp diffraction lines, showing that the LAO film is highly crystalline. There is some additional intensity modulation along the streaks indicating a slight increase in the surface roughness after the ALD and the annealing processes. The composition, as measured by *in-situ* XPS, did not change after annealing amorphous films. LAO films grown by the same method and annealed at temperatures up to 550 °C for 2 h remained amorphous. According to the AFM analysis, the root-mean-square surface roughness of the LAO film on STO-buffered Si(001) before (not shown) and after annealing at 600 °C (Figure 2.2) was 0.55 nm and 0.54 nm, respectively.

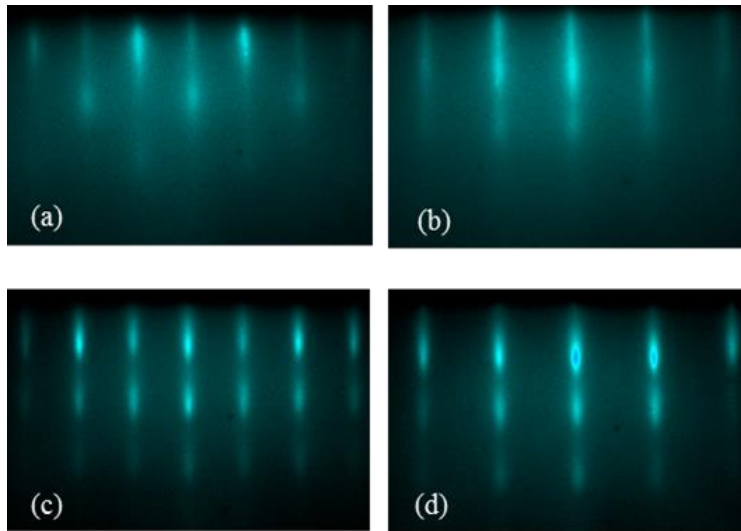


Figure 2.1. RHEED images captured before ALD growth [(a), (b)] and after annealing at 600 °C for 2 h of a 10 nm thick LAO film [(c) and (d)]. The beam was aligned along the <100> for (a) and (c), and <110> azimuth for (b) and (d).

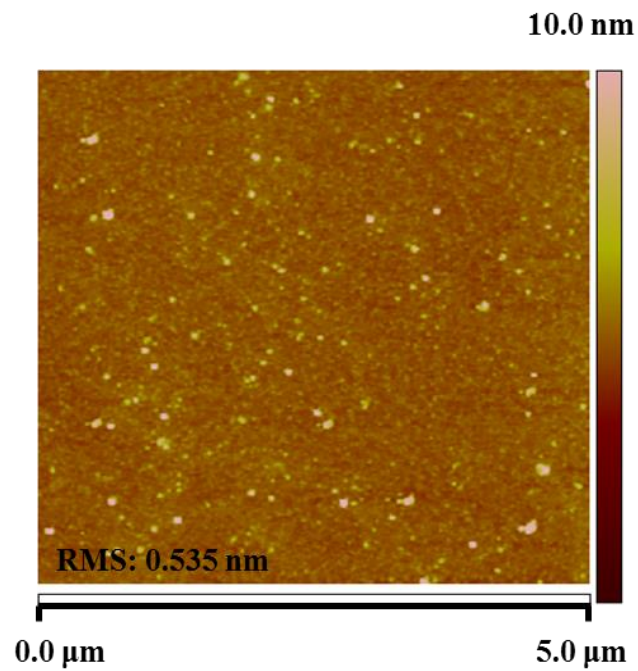


Figure 2.2. AFM image of a  $5 \times 5 \mu\text{m}^2$  area of an 8-nm thick LAO film grown by ALD on STO-buffered Si(001) after annealing at 600 °C for 2 h.

To study the effect of the film thickness on the transition from amorphous to crystalline films, LAO films with different thicknesses were grown on STO-buffered Si(001) templates and annealed at temperatures ranging from 600 to 750 °C. RHEED images taken after annealing (not shown) indicate that LAO films that are either too thick (> 40 nm) or too thin (< 2 nm) were more difficult to crystallize; these films crystallized at higher annealing temperature (700 °C) for an annealing time of 2 h. To study the effect of La:Al ratio on crystallinity, films with varying La:Al ratios were grown by changing the cycle ratio x:y and/or the La dosing time. The La-rich LAO films (up to 1.4:1 La:Al) crystallized after annealing at 600 °C for 2 h, but the Al-rich LAO films (up to 0.85:1 La:Al) crystallized at higher temperature (700-750 °C) based on RHEED images (not shown).

Figure 2.3 presents the ( $\theta$ -2 $\theta$ ) scan of a 10 nm thick LAO film annealed at 600 °C for 2 h. The pseudocubic (001), (002) and (003) Bragg peaks are present, confirming the *c*-axis orientation of the crystalline LAO films.<sup>39,50,51</sup> There was no evidence of any other orientations or secondary phases. The LAO (001) Bragg peak position at  $2\theta = 23.68^\circ$ , corresponds to an out-of-plane lattice constant of 3.75 Å, which is slightly reduced from the bulk pseudocubic LAO lattice constant of 3.79 Å.<sup>52</sup> This is consistent with the LAO film being coherently strained to the underlying Si(001), which has a surface lattice constant of 3.84 Å. If the LAO is perfectly strained to the underlying silicon ( $a = 3.84$  Å), the out-of-plane lattice constant calculated using the reported value of Poisson's ratio of 0.25<sup>53,54</sup> should have a value of 3.76 Å. The XRD rocking curve around the (001) Bragg peak shows a full-width at half-maximum (FWHM) of 0.23° (Figure 2.4(a)), indicating a high degree of crystallinity for the LAO film. Additional annealing of the film in vacuum at 750 °C for 2 h did not improve the crystallinity but rather worsened it, yielding a

FWHM of  $0.40^\circ$  (Figure 2.4(b)). Furthermore, XPS analysis reveals that annealing at  $750^\circ\text{C}$  leads to a substantial fraction of STO reacting with Si to form oxidized silicon and/or silicates (discussed in more detail below), producing a thicker amorphous interfacial layer.

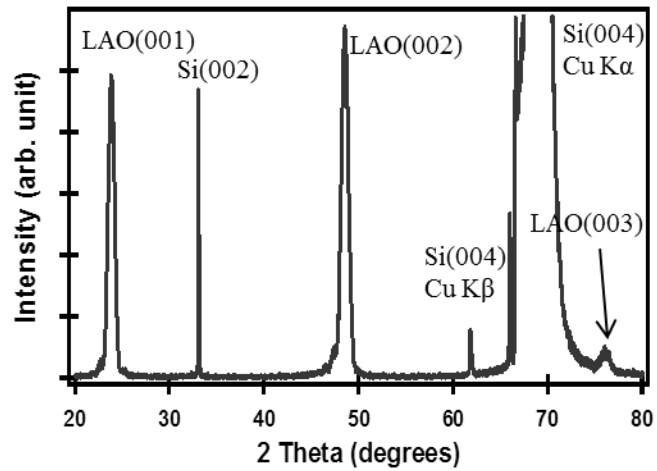


Figure 2.3. X-ray diffraction pattern of a 10-nm thick LAO film grown by ALD on STO-buffered Si(001) at  $250^\circ\text{C}$ . The sample was post-deposition annealed in vacuum at  $600^\circ\text{C}$  for 2 h.

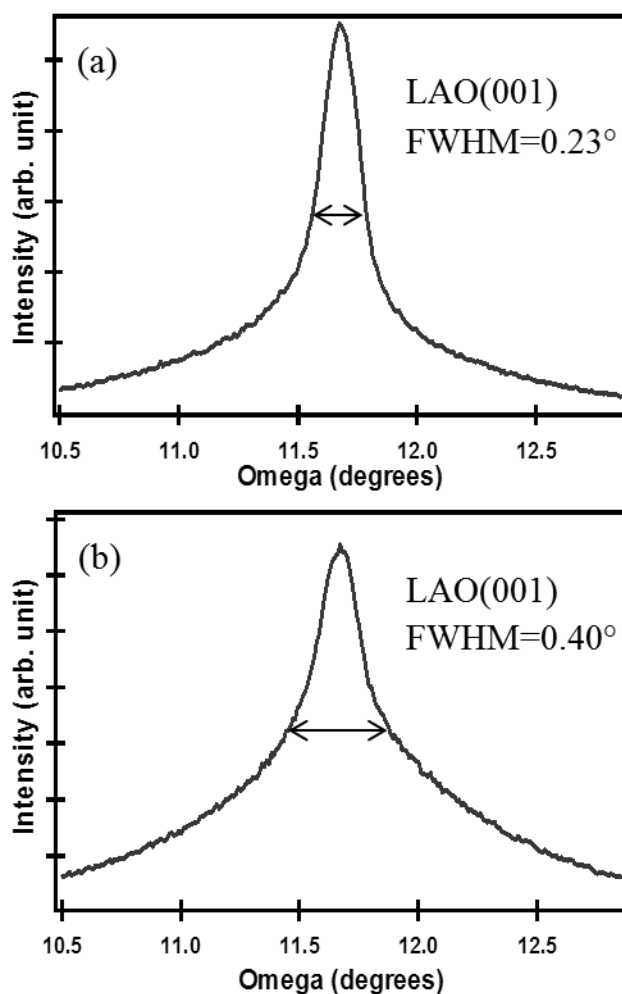


Figure 2.4. Rocking curves around the LAO(001) Bragg peak at a fixed  $2\theta=23.68^\circ$  for a 10-nm thick LAO film grown by ALD on STO-buffered Si(001) after annealing at 600 °C for 2 h (a) and after additional annealing at 750 °C for another 2 h (b).

To study the STO/Si interface reaction during vacuum annealing, a four-unit cell STO on Si(001) sample was grown via MBE and transferred *in-situ* to the XPS system. All XP spectra were shifted by taking the Si 2p elemental peak to be at 99.3 eV, and the peak areas were used for quantification of relative amounts. Because the Si 2p feature partially overlaps with the La 4d feature, the Si 2s spectra were used to study the amount of Si-O bonding at the STO/Si interface throughout the ALD and annealing processes.

Table 2.1 provides binding energy assignments for Ti and Sr XPS peaks. Figures 2.5(a) and 5(b) present spectra of Si 2s and Ti 2p peaks, respectively, for MBE-grown STO on silicon indicating a minor SiO<sub>x</sub> feature (152.2 eV) at the STO/Si interface. We selected the STO growth and annealing conditions to minimize the oxidation of the STO/Si(001) interface. These STO growth conditions lead to an oxygen deficiency as indicated by the presence of Ti<sup>3+</sup> (29%) and Ti<sup>2+</sup> (9%). The sample was transferred to the ALD chamber and exposed to 5 super-cycles of LAO at 250 °C (15 cycles of La and 10 cycles of Al), then transferred back to the XPS chamber.

<b>Sr<sup>2+</sup></b>	<b>Peak</b>	<b>In SrTiO<sub>3</sub></b>	<b>In Strontium Silicate</b>	
		3d <sub>5/2</sub>	133.8	134.8
	3d <sub>3/2</sub>	135.7	136.6	
<b>Ti</b>	<b>Peak</b>	<b>Ti<sup>4+</sup></b>	<b>Ti<sup>3+</sup></b>	<b>Ti<sup>2+</sup></b>
	2p <sub>3/2</sub>	459.7	458.0	455.9
	2p <sub>1/2</sub>	465.5	463.8	461.7

Table 2.1. XPS peak assignments (eV)

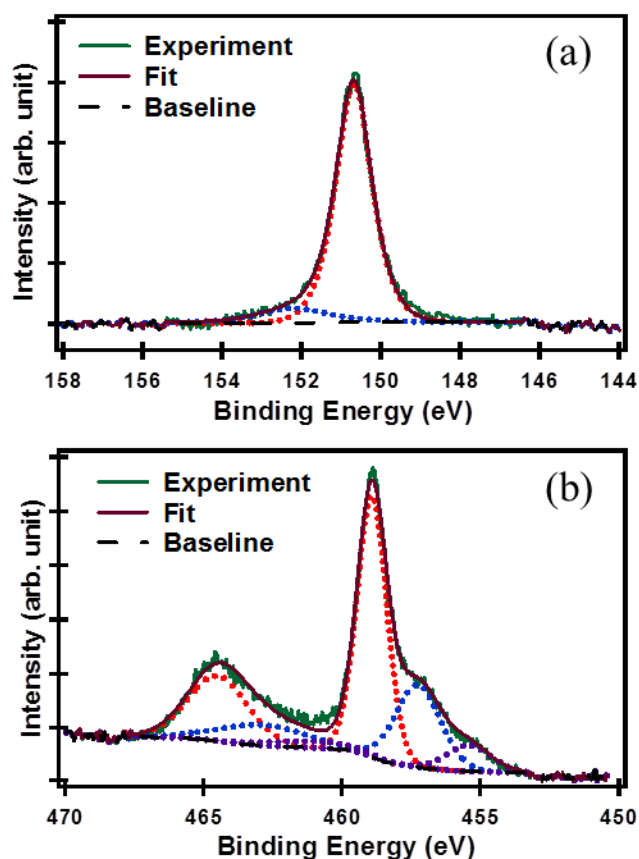


Figure 2.5. (a) X-ray photoelectron spectrum of Si 2s for four unit cell STO-buffered Si(001) grown by MBE: the dotted curves show the fits for Si<sup>0</sup> (red) and Si in SiO<sub>x</sub> (blue); (b) X-ray photoelectron spectrum of Ti 2p for four unit cell STO-buffered Si(001) grown by MBE: the dotted curves show the fits for Ti<sup>4+</sup> (red), Ti<sup>3+</sup> (blue), and Ti<sup>2+</sup> (purple) as-described in Table 2.1.

Figures 2.6, 2.7, and 2.8 present the Si 2s, Ti 2p, and Sr 3d spectra following ALD and post-deposition annealing at 600 and 750 °C, respectively. The results in Figure 2.6(a) show that after the ALD process there is a little to no additional SiO<sub>x</sub> formation during the H<sub>2</sub>O exposures used in ALD at 250 °C, which is consistent with our previous work.<sup>55</sup> After ALD there is 18% Ti<sup>3+</sup> and no Ti<sup>2+</sup> (Figure 2.7(a)) compared to 29% Ti<sup>3+</sup> and 9% Ti<sup>2+</sup> in the MBE-grown template (Figure 2.5(b)) indicating that during ALD growth oxygen from the water reacted with the Ti<sup>2+</sup> and Ti<sup>3+</sup>. The Sr 3d signal appears

unchanged after the ALD process (Figure 2.8(a)). After annealing at 600 °C for 2 h, a small increase in Si-O bond formation was observed at the STO/Si interface (Figure 2.6(b)), accompanied by an increase in the fraction of  $Ti^{3+}$  species (37%), as well as the re-appearance of  $Ti^{2+}$  species (17%), as shown in Figure 2.7(b) indicating that the oxygen within the STO is a likely oxygen source for the reactions at the interface. There is also minor broadening of the Sr 3d peak (Figure 2.8(b)), which can be attributed to the formation of strontium silicates;<sup>56</sup> roughly 25% of the Sr signal is due to strontium silicate. These data indicate that STO started reacting with Si during the annealing process at 600 °C and that roughly a monolayer of the silicate forms after annealing at 600 °C. After further annealing at 750 °C, there was more Si-O bond formation at the STO/Si interface (Figure 2.6(c)), a further reduction of Ti as evidenced by an increase in the peak area of  $Ti^{2+}$  to 22.7% (Figure 2.7(c)), and significant broadening of the Sr 3d peak was also observed indicating the presence of additional strontium silicates (42%) (Figure 2.8(c)). Interfacial  $SiO_2$  may also be present in addition to the strontium silicates.

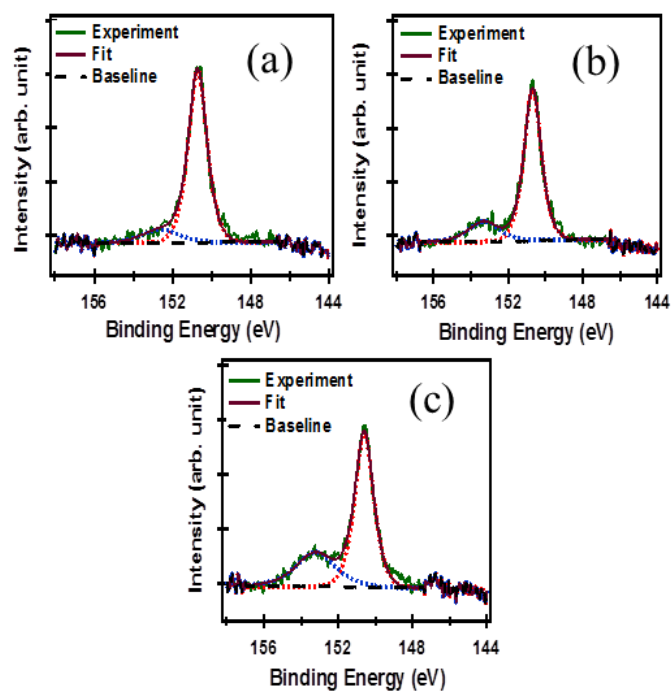


Figure 2.6. X-ray photoelectron spectra of Si 2s after ALD (a), after annealing at 600 °C for 2 h (b), and after additional annealing at 750 °C for another 2 h (c), respectively: the dotted curves show the fits for Si<sup>0</sup> (red) and Si in SiO<sub>x</sub> and/or strontium silicate (blue).

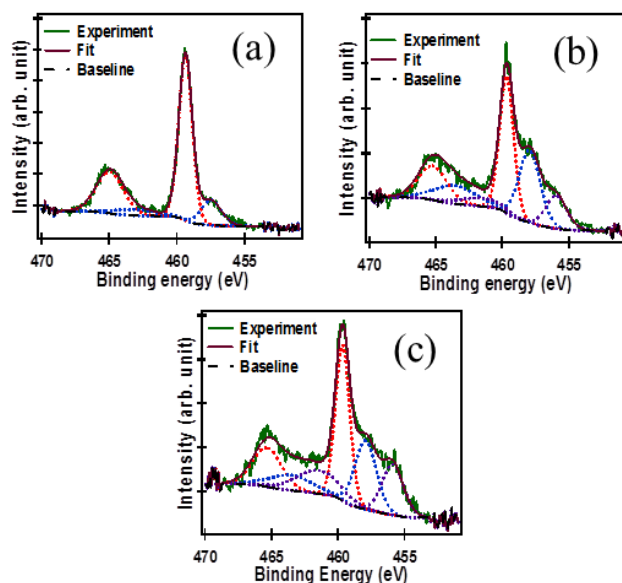


Figure 2.7. X-ray photoelectron spectra of Ti 2p after ALD (a), after annealing at 600 °C for 2 h (b) and after additional annealing at 750 °C for another 2 h (c), respectively: the dotted curves show the fits for  $\text{Ti}^{4+}$  (red),  $\text{Ti}^{3+}$  (blue), and  $\text{Ti}^{2+}$  (purple) as-described in Table 2.1.

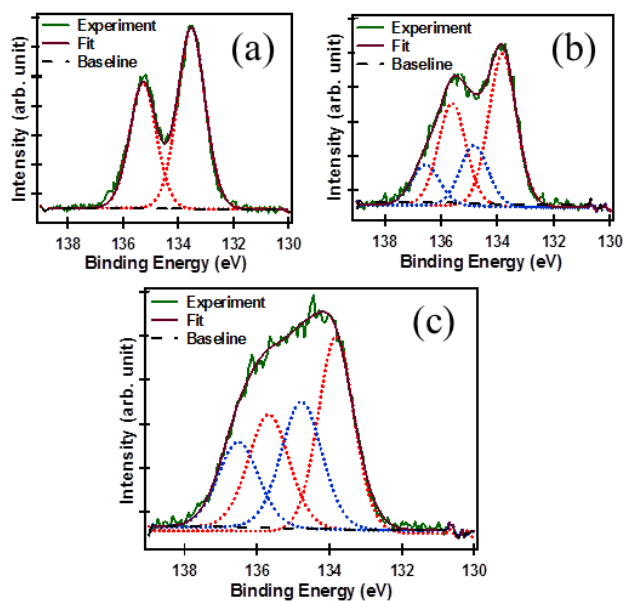


Figure 2.8. X-ray photoelectron spectra of Sr 3d after ALD (a), after annealing at 600 °C for 2 h (b) and after additional annealing at 750 °C for another 2 h (c), respectively: the dotted curves show the fits for Sr in STO (red), in strontium silicate (blue) as-described in Table 2.1.

Figure 2.9 and the inset of Figure 2.9 are spherical-aberration corrected high-angle annular dark field scanning transmission electron microscopy (STEM) cross-sectional Z-contrast images of a 12 nm LAO film annealed at 600 °C for 2 h. These images confirm the high degree of crystallinity of LAO films and show the sharp interface between LAO and STO, as well as the existence of a thin (~1 nm) amorphous interlayer between STO and Si due to strontium silicates and possibly SiO<sub>2</sub>. Figure 2.9 also shows an amorphous LAO column and the STO also appears amorphous in this region. A lower magnification image (not shown) appears to show ~20 nm crystalline domains. Because LAO films are susceptible to ion beam damage during TEM sample preparation,<sup>57</sup> additional studies are required to determine if the amorphous LAO domain remained after 600 °C annealing for 2 h or by the TEM sample preparation process. Geometric phase analysis of the lattice image of the 600 °C-annealed sample (not shown) confirms single crystal orientation of the LAO film with respect to silicon. Figure 2.10 is a cross-section bright-field (BF) TEM image of a 25 nm LAO film annealed at 750 °C for 2 h. The image shows a slightly thicker amorphous interlayer (~1.5 nm) at the STO/Si interface, which is consistent with the XPS results in Figure 2.6(c). The image also shows that the bottom STO interface with Si(001) is no longer sharp indicating significant atomic mixing. These results suggest that annealing temperature and time are important variables for a given LAO thickness and composition to optimize the LAO crystal quality, and minimize the SiO<sub>x</sub> formation and reduction of the STO buffer layer.

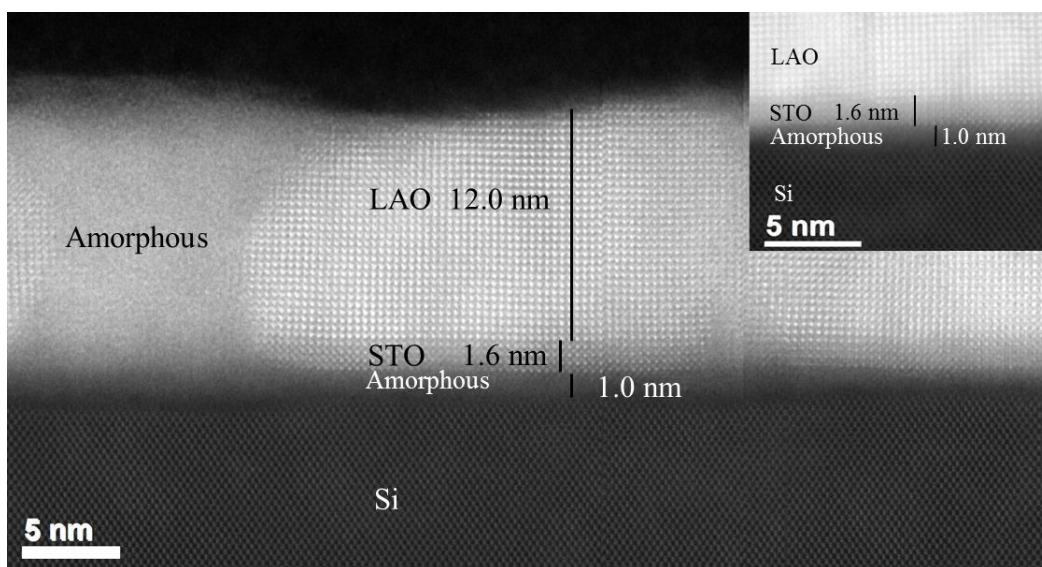


Figure 2.9. Cross-sectional Z-contrast TEM image of a 12 nm LAO film on STO-buffered Si(001) after annealing at 600 °C for 2 h that illustrates the Si/STO/LAO interfaces. The inset is an expanded image Si/STO/LAO interface region.

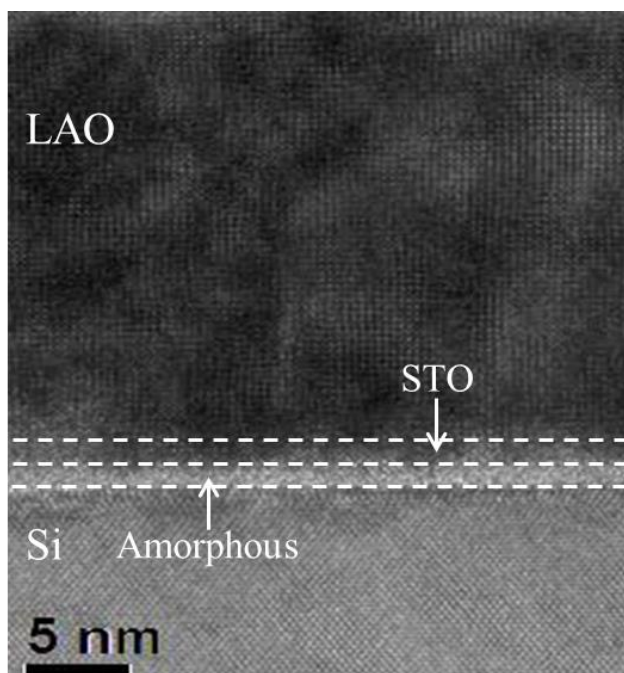


Figure 2.10. Cross-sectional BF TEM of a 25 nm LAO film on STO-buffered Si(001) after annealing at 750 °C for 2 h.

## 2.4. SUMMARY

Epitaxial LAO films have been grown on STO-buffered Si(001) substrates by ALD at 250 °C followed by annealing for 2 h at 600 °C under vacuum. The crystallinity and epitaxial relationship were determined by RHEED, XRD and TEM. By keeping the annealing temperature relatively low, the interfacial amorphous layer at the STO/Si interface was minimized to about one monolayer as observed by XPS and confirmed by TEM. The results demonstrate that highly crystalline, epitaxial LAO films can be formed on STO-buffered Si with a minimal amorphous interfacial layer between STO/Si by maintaining the annealing temperature as low as possible. The ability to obtain high crystalline quality epitaxial LAO films on Si using ALD provides an alternative chemical route for fabricating complex oxide heterostructures and superlattices, and is also potentially suitable as a replacement high- $\kappa$  gate dielectric in Si based-transistors for the sub-22 nm technology.

## 2.5. REFERENCES

- <sup>1</sup>R. A. McKee, F. J. Walker, and M. F. Chisholm, *Phys. Rev. Lett.* **81**, 3014–3017 (1998).
- <sup>2</sup>J. W. Reiner, A. M. Kolpak, Y. Segal, K. F. Garrity, S. Ismail-Beigi, C. H. Ahn, and F. J. Walker, *Adv. Mater.* **22**, 2919–2938 (2010).
- <sup>3</sup>R. Droopad, Z. Yu, H. Li, Y. Liang, C. Overgaard, A. Demkov, X. Zhang, K. Moore, K. Eisenbeiser, M. Hu, J. Curless, and J. Funder, *J. Cryst. Growth* **251**, 638–644 (2003).
- <sup>4</sup>N. Izyumskaya, Y. Alivov, and H. Morkoç, *Crit. Rev. Sol. Stat. Mater. Sci.* **34**, 89–179 (2009).
- <sup>5</sup>S. Coh, T. Heeg, J. H. Haeni, M. D. Biegalski, J. Lettieri, L. F. Edge, K. E. O’Brien, M. Bernhagen, P. Reiche, R. Uecker, S. Trolier-McKinstry, D. G. Schlom, and D. Vanderbilt, *Phys. Rev. B* **82**, 064101 (2010).

- <sup>6</sup>H. Li, X. Hu, Y. Wei, Z. Yu, X. Yang, R. Droopad, A. A. Demkov, J. Erwards, K. Moore, W. Ooms, J. Kulik, and P. Fejes, *J. Appl. Phys.* **39**, 4521–4525 (2003).
- <sup>7</sup>M. Choi, A. Posadas, R. Dargis, C.-K. Shih, A. A. Demkov, D. H. Triyoso, N. D. Theodore, C. Dubourdieu, J. Bruley, and J. Jordan-Sweet, *J. Appl. Phys.* **111**, 064112 (2012).
- <sup>8</sup>Z. Yu, J. Ramdani, J. A. Curless, C. D. Overgaard, J. M. Finder, R. Droopad, K. W. Eisenbeiser, J. A. Hallmark, W. J. Ooms, and V. S. Kaushik, *J. Vac. Sci. Technol. B* **18**, 2139–2145 (2000).
- <sup>9</sup>M. J. Dicken, K. Diest, Y. B. Park, and H. A. Atwater, *J. Cryst. Growth* **300**, 330–335 (2007).
- <sup>10</sup>C. Rossel, M. Sousa, C. Marchiori, J. Fompeyrine, D. Webb, D. Caimi, B. Mereu, A. Ispas, J. P. Locquet, H. Siegwart, R. Germann, A. Tapponnier, and K. Babich, *Microelectro. Eng.* **84**, 1869–1873 (2007).
- <sup>11</sup>J. W. Seo, Ch. Dieker, A. Tapponnier, C. Marchiori, M. Sousa, J. -P. Locquet, J. Fompeyrine, A. Ispas, C. Rossel, Y. Panayiotatos, A. Sotiropoulos, and A. Dimoulas, *Microelectro. Eng.* **84**, 2328–2331 (2007).
- <sup>12</sup>A. Posadas, M. Berg, H. Seo, D. J. Smith, H. Celio, A. P. Kirk, D. Zhernokletov, R. M. Wallace, A. de Lozanne, and A. A. Demkov, *Appl. Phys. Lett.* **98**, 055104 (2011).
- <sup>13</sup>M. P. Warusawithana, C. Cen, C. R. Sleasman, J. C. Woicik, Y. Li, L. F. Kourkoutis, J. A. Klug, H. Li, P. Ryan, L. P. Wang, M. Bedzyk, D. A. Muller, L. Q. Chen, J. Levy, And D. G. Schlom, *Science* **324**, 367–370 (2009).
- <sup>14</sup>Z. L. Wang, *Sur. Sci.* **360**, 180–186 (1996).
- <sup>15</sup>H. Schneidewind, M. Manzel, G. Bruchlos, and K. Kirsch, *Supercond. Sci. Technol.* **14**, 200–212 (2001).

- <sup>16</sup>G. H. Thomas, E. D. Specht, J. Z. Larese, Z. B. Xue, and D. B. Beach, *J. Mater. Res.* **12**, 3281–3287 (2008).
- <sup>17</sup>F. Pan, D. Olaya, J. C. Price, and C. T. Rogers, *Appl. Phys. Lett.* **84**, 1573–1575 (2004).
- <sup>18</sup>H. Schneidewind and G. Bruchlos, *Trans. Appl. Supercond.* **13** 2766–2768 (2003).
- <sup>19</sup>S. B. Majumder, M. Jain, A. Martinez, R. S. Katiyar, F. W. van Keuls, and F. A. Miranda, *J. Appl. Phys.* **90**, 896–903 (2001).
- <sup>20</sup>P. D. Tall, C. Coupeau, and J. Rabier, *Scripta Materialia* **49**, 903–908 (2003).
- <sup>21</sup>J. Robertson, *Rep. Prog. Phys.* **69**, 327–396 (2006).
- <sup>22</sup>C. Zhao, C. Z. Zhao, M. Werner, S. Taylor, and P. R. Chalker, *ISRN Nanotechnol.* **2012**, 689023 (2011).
- <sup>23</sup><http://www.itrs.net/Links/2011ITRS/Home2011.htm>
- <sup>24</sup>A. Ohtomo and H. Y. Hwang, *Nature* **427**, 423–426 (2004).
- <sup>25</sup>Ariando, X. Wang, G. Baskaran, Z. Q. Liu, J. Huijben, J. B. Yi, A. Annadi, A. Roy Barman, A. Rusydi, S. Dhar, Y. P. Feng, J. Ding, H. Hilgenkamp, and T. Venkatesan, *Nat. Comm.* **2**, 188 (2011).
- <sup>26</sup>P. R. Willmott, S. A. Pauli, R. Herger, C. M. Schlepütz, D. Martoccia, B. D. Patterson, B. Delley, R. Clarke, D. Kumah, C. Cionca, and Y. Yacoby, *Phys. Rev. Lett.* **99**, 155502 (2007).
- <sup>27</sup>A. D. Caviglia, S. Gariglio, N. Reyren, D. Jaccard, T. Schneider, M. Gabay, S. Thiel, G. Hammerl, J. Mannhart, and J. -M. Triscone, *Nature* **456**, 624–627 (2008).
- <sup>28</sup>L. Li, C. Richter, J. Mannhart, and R. C. Ashoori, *Nat. Phys.* **7**, 762–766 (2011).
- <sup>29</sup>J. A. Bert, B. Kalisky, C. Bell, M. Kim, Y. Hikita, H. Hwang, K. A. Moler, *Nat. Phys.* **7**, 767–771 (2011).
- <sup>30</sup>N. Reyren, M. Bibes, E. Lesne, J.-M. George, C. Deranlot, S. Collin, A. Barthélémy, and H. Jaffrès, *Phys. Rev. Lett.* **108**, 186802 (2012).

- <sup>31</sup>J. H. Jun, J. Jun, and D. J. Choi, *Electrochem. Solid-State Lett.* **6**, F37–F39 (2003).
- <sup>32</sup>A. D. Li, J. B. Cheng, Q. Y. Shao, H. Q. Ling, D. Wu, Y. Wang, M. Wang, Z. G. Liu, N. B. Ming, C. Wang, H. W. Zhou, and B. Y. Nguyen, *Ferroelec.* **329**, 73–77 (2005).
- <sup>33</sup>J. H. Jun, D. J. Choi, *Jpn. J. Appl. Phys.* **43**, 7576–7578 (2004).
- <sup>34</sup>H. Ling, X. Lu, A. Li, D. Wu, Q. Shao, J. Sheng, Z. Liu, N. Ming, X. Wang, B. Y. Nguyen, and H. Zhou, *Appl. Phys. A* **80**, 641–644 (2005).
- <sup>35</sup>K. -C. Liu, W. -H. Tzeng, K. -M. Chang, J. -J. Huang, Y. -J. Lee, P. -H. Yeh, P. -S. Chen, H. -Y. Lee, F. Chen, and M. -J. Tsai, *Thin Solid Film* **520**, 1246–1250 (2011).
- <sup>36</sup>L. F. Edge, D. G. Schlom, P. Sivasubramani, R. M. Wallace, B. Holländer, and J. Schubert, *Appl. Phys. Lett.* **88**, 112907 (2006).
- <sup>37</sup>X. B. Lu, Z. G. Liu, Y. P. Wang, Y. Yang, X. P. Wang, H. W. Zhou, and B. Y. Nguyen, *J. Appl. Phys.* **94**, 1229 (2003).
- <sup>38</sup>D. H. Triyoso, H. Li, R.I. Hegde, Z. Yu, K. Moore, J. Grant, B. E. White, and P. J. Tobin, *J. Vac. Sci. Technol. B* **23**, 2480 (2005).
- <sup>39</sup>J. W. Reiner, A. Posadas, M. Wang, M. Sidorov, Z. Krivokapic, F. J. Walker, T. P. Ma, and C. H. Ahn, *J. Appl. Phys.* **105**, 124501 (2009).
- <sup>40</sup>W. F. Xiang, H. B. Lu, Z.H. Chen, X. B. Lu, M. He, H. Tian, Y. L. Zhou, C. R. Li, and X. L. Ma, *J. Cryst. Growth* **271**, 165–170 (2004).
- <sup>41</sup>C. Merckling, G. Delhaye, M. El-Kazzi, S. Gaillard, Y. Rozier, L. Rapenne, B. Chenevier, O. Marty, G. Saint-Girons, M. Gendry, Y. Robach, and G. Hollinger, *Microelectro. Relia.* **47**, 540–543 (2007).
- <sup>42</sup>Y. Y. Mi, Z. Yu, S. J. Wang, P. C. Lim, Y. L. Foo, A. C. H. Huan, and C. K. Ong, *Appl. Phys. Lett.* **90**, 181925 (2007).
- <sup>43</sup>A. Posadas, R. Dargis, M. Choi, A. Slepko, J. J. Kim, D. J. Smith, and A. A. Demkov, *J. Vac. Sci. Technol. B* **29**, 1071 (2011).

- <sup>44</sup>K. Kukli, M. Ritala, V. Pore, M. Leskelä, T. Sajavaara, R. I. Hegde, D. C. Gilmer, P. J. Tobin, A. C. Jones, and H. C. Aspinall, *Chem. Vap. Deposition* **12**, 158–164 (2006).
- <sup>45</sup>G. Congedo, S. Spiga, L. Lamagna, A. Lamperti, Y. Lebedinskii, Y. Matveyev, A. Zenkevich, P. Chernykh, and M. Fanciulli, *Microelectro. Engin.* **86**, 1696–1699 (2009).
- <sup>46</sup>D. Eom, C. S. Hwang, H. J. Kim, M.-H Cho, and K. B. Chung, *Electrochem. Solid-State Lett.* **11**, G33–G36 (2008).
- <sup>47</sup>D. H. Triyoso, R. I. Hegde, J. M. Grant, J. K. Schaeffer, D. Roan, B. E. White, and P. J. Tobin, *J. Vac. Sci. Technol. B* **23**, 288 (2005).
- <sup>48</sup>M. D. McDaniel, A. Posadas, T. Wang, A. A. Demkov, and J. G. Ekerdt, *Thin Solid Film* **520**, 6525–6530 (2012).
- <sup>49</sup>Z. Yu, J. Ramdani, J. A. Curless, J. M. Finder, C. D. Overgaard, R. Droopad, K. W. Eisenbeiser, J. A. Hallmark, W. J. Ooms, J. R. Conner, and V. S. Kaushik, *J. Vac. Sci. Technol. B* **18**, 1653 (2000).
- <sup>50</sup>N. M. Sbrockey, M. Luong, E. M. Gallo, J. D. Sloppy, G. Chen, C. R. Winkler, S. H. Johnson, M. L. Taheri, G. S. Tompa, J. E. Spanier, *J. Electro. Mater.* **41** 819–823 (2012).
- <sup>51</sup>M. Nieminen, T. Sajavaara, E. Rauhala, M. Putkonen, and L. Niinistö, *J. Mater. Chem.* **11**, 2340–2345 (2001).
- <sup>52</sup>G. W. Berkstresser, A. J. Valentino, and C. D. Brandle, *J. Cryst. Growth* **109**, 457–466 (1991).
- <sup>53</sup>X. Luo and B. Wang, *J. Appl. Phys.* **104**, 073518 (2008).
- <sup>54</sup>S. A. Pauli, S. J. Leake, B. Delley, M. Bjorck, C. W. Schneider, C. M. Schleputz, D. Martoccia, S. Paetel, J. Mannhart, and P. R. Willmott, *Phys. Rev. Lett.* **106**, 023101 (2011).
- <sup>55</sup>M. D. McDaniel, A. Posadas, T. Q. Ngo, A. Dhamdhere, D. J. Smith, A. A. Demkov, and J. G. Ekerdt, *J. Vac. Sci. Technol. B* **30**, 04E111 (2012).

<sup>56</sup>M. El Kazzi, G. Delhayé, C. Merckling, E. Bergignat, Y. Robach, G. Grenet, and G. Hollinger, *J. Vac. Sci. Technol. A* **25**, 1505–1511 (2007).

<sup>57</sup>E. Montoya, S. Bals, M. D. Rossell, D. Schryvers, and G. V. Tendeloo, *Microsc. Res. Tech.* **70**, 1060–1071 (2007).

## **Chapter 3: Growth of crystalline LaAlO<sub>3</sub> by atomic layer deposition: a comparison on SrTiO<sub>3</sub>/Si(001) and SrTiO<sub>3</sub> substrates**

### **3.1. INTRODUCTION**

With a dielectric constant of 25-30 and a bandgap of 6.5 eV single crystal lanthanum aluminate [LaAlO<sub>3</sub>] (LAO) is a potential candidate for a gate dielectric in future metal-oxide-semiconductor field effect transistors (MOSFETs).<sup>1,2</sup> In addition, the interface between crystalline LAO and strontium titanate [SrTiO<sub>3</sub>] (STO) has been shown to exhibit a two-dimensional electron gas that displays quantum oscillation in magnetotransport<sup>3,4</sup> and superconductivity.<sup>5-8</sup> Devices have been proposed that exploit the two-dimensional gas property of this interface.<sup>9</sup>

Single crystal LAO is grown on Si using STO-buffered Si(001) substrates. Epitaxial LAO films on STO-buffered Si(001) substrates have been grown by molecular beam epitaxy (MBE) at high temperature (> 600 °C).<sup>10-12</sup> However, the STO/Si interface is not stable above 600 °C, and oxygen present in the MBE-deposited STO can lead to the formation of an amorphous SiO<sub>x</sub> or silicate layer at the STO/Si interface at high temperature.<sup>11-14</sup> Growth of oxide films by atomic layer deposition (ALD) may offer several advantages when compared to MBE and pulsed laser deposition, such as uniform deposition over large area substrates, good conformality and compatibility with current processing tools. The use of ALD to deposit complex oxides has been reported.<sup>15-18</sup> We have previously reported the growth of LAO on STO-buffered Si(001) by a chemical route.<sup>19</sup> LAO films were grown epitaxially on Si(001) by ALD using a buffer layer of STO grown by MBE. The ALD growth of LAO was done at 250 °C by using tris(N,N'-diisopropylformamidinate)-lanthanum, trimethylaluminum, and water as co-reactants.

Four unit cells of STO were required as the buffer layer. The as-deposited LAO films were amorphous and became crystalline after vacuum annealing at 600 °C for 2 h. *In-situ* X-ray photoelectron spectroscopy (XPS) analysis showed minimal Si-O bonding at the STO/Si interface after the ALD process and after post-deposition annealing at 600 °C for 2 h.

Single crystal LAO can also be grown on single crystal substrates by pulsed laser deposition and molecular beam epitaxy.<sup>20,21</sup> The substrate temperature is between 680 and 800 °C during growth. Post growth processing may also be required.

This study compares the ALD growth of LAO on a bulk crystal of STO and on STO-buffered Si(001). For direct integration of STO with Si(001), there is a relatively small (1.7%) lattice mismatch with a 45° in-plane rotation, where the STO is compressively strained to Si. Previous studies have shown a four-unit cell STO layer to be commensurate with the Si(001) lattice. The degree of compressive strain is a function of the annealing temperature and the thickness of the SiO<sub>2</sub> layer that can form at the interface between Si(001) and STO.<sup>22</sup> In the case of four unit cells annealed at less than 650 °C, the in-plane lattice constant of the STO film is the same as Si(001) spacing along the [110] direction. Films grown on the STO-buffered Si(001) substrate are strained to the Si(001) lattice spacing (3.84 Å). Single crystal STO has a larger lattice constant ( $a = 3.905$  Å), creating more tensile strain in the epitaxial LAO film. A comparison of the growth and annealing of crystalline LAO films on the two different substrates is described.

### 3.2. METHODOLOGY

The ALD system has been previously described.<sup>19,23</sup> The 0.5 mm-thick Si(001) substrates were cut into  $20 \times 20 \text{ mm}^2$  squares from n-type Si(001) wafers, and were ultrasonically cleaned with acetone, isopropyl alcohol, and deionized water for 15 min each, followed by UV/ozone treatment for 15 min to remove residual carbon contamination. The wafers were loaded into the MBE chamber where four unit cells of STO were deposited on Si(001) as described in more detail elsewhere.<sup>22,23</sup> The LAO growth was also examined on  $10 \times 10 \times 0.5 \text{ mm}^3$  STO(001) single crystal substrates from MTI. The STO substrates were ultrasonically cleaned with acetone, isopropyl alcohol, and deionized water for 15 min each, followed by UV/ozone treatment for 15 min to remove residual carbon contamination. The STO substrates were then loaded into the system and annealed at 650 °C for 15 min to outgas before ALD growth.

For ALD, tris(N,N'-diisopropylformamidinate)-lanthanum and trimethylaluminum were used as precursors for La and Al, respectively, and water was used as the oxidant. The La precursor was maintained at 137 °C, while the Al precursor and water were maintained at room temperature (26 °C). The substrate temperature was maintained at 250 °C throughout the deposition. Ultrahigh purity argon was used as a purge/carrier gas. Experiments have been presented that describe the conditions that produce a nearly stoichiometric film on STO-buffered Si(001).<sup>19</sup> The *in-situ* VG Scienta R3000 X-ray photoelectron spectroscopy (XPS) system was used to determine the film composition. Each La cycle consisted of a 2 sec dose of the La precursor, a 10 sec purge of Ar, a 1 sec dose of water and a 10 sec purge of Ar. Each Al cycle consisted of a 0.5 sec dose of the Al precursor, a 15 sec purge of Ar, a 1 sec dose of water and a 10 sec purge of Ar. LAO films were grown using 3 La cycles followed by 2 Al cycles (noted as a super-cycle), resulting in a slightly La rich film (1.1:1.0 La:Al). The same conditions were used

for growth on STO(001). The growth rate of the LAO films on STO-buffered Si (001) under these conditions is  $0.50\pm 0.01$  nm/super-cycle.

As-deposited LAO films were annealed in vacuum ( $1\times 10^{-9}$  Torr) at temperatures ranging from 500 to 750 °C. Film thickness was determined by X-ray reflectivity (XRR). *In-situ* XPS was used to study the effect of annealing on the STO/Si interface. The LAO film crystallinity and orientation were determined by reflection high energy electron diffraction (RHEED) and X-ray diffraction (XRD). XRR and XRD were conducted with a Bruker-AXS D8 Advance Powder Diffractometer using a sealed tube Cu K $\alpha$  radiation source. Veeco Multimode V atomic force microscopy (AFM) was used to determine the root-mean-square surface roughness of the film. Cross-section transmission electron microscopy (TEM) was used to confirm the crystallinity and overall quality of the LAO/STO/Si stack.<sup>19</sup>

### 3.3. RESULTS AND DISCUSSION

Figure 3.1(a) presents the RHEED patterns of a typical four-unit-cell STO-buffered Si(001) substrate grown by MBE, taken along  $\langle 110 \rangle$  direction, showing that the STO layer is crystalline with an atomically flat surface. This four-unit-cell STO template (thickness of 1.5 nm) was transferred to the ALD chamber *in vacuo* and exposed to 20 super-cycles of LAO that consisted of 60 cycles of La and 40 cycles of Al at 250 °C. After ALD growth, the film was transferred back to the MBE chamber to check the RHEED pattern. Figure 3.1(b) presents the RHEED patterns of an as-deposited 10-nm LAO film showing the bright back ground, which consistently indicated that the as-deposited films were amorphous. The LAO film was then transferred to the annealing chamber and heated to 600 °C in vacuum for 2 h. The RHEED patterns in Figure 3.1(c)

(again taken along  $\langle 110 \rangle$  direction) exhibit sharp diffraction lines, showing that the LAO film is highly crystalline. There is some additional intensity modulation along the streaks indicating a slight increase in the surface roughness after the ALD and the annealing processes. The composition, as measured by *in-situ* XPS, did not change after annealing amorphous films. LAO films grown by the same method and annealed at temperatures up to 550 °C for 2 h still remained amorphous. According to the AFM analysis, the root-mean-square surface roughness of the LAO film on STO-buffered Si(001) before and after annealing at 600 °C (not shown) were 0.55 nm and 0.54 nm, respectively. ALD LAO growth was also examined on single crystal STO substrates from MTI using the same ALD condition. The ALD-grown LAO films on STO substrates were amorphous as-deposited and after a 2 h vacuum anneal at 600 °C. The LAO grown on single crystal STO became crystalline after a 2 h vacuum anneal at 750 °C (Figure 3.1(d)). Figure 3.1(d) shows well-defined streaks, indicating the high degree of crystalline order. The larger lattice constant mismatch between LAO and STO substrate (-2.9 %), compared to LAO and STO-buffered Si(001) (-1.3%-assuming in-plane lattice constant of four-unit-cell STO is equal to the Si surface lattice constant) could be a factor that leads to the higher annealing temperature of LAO on STO substrates (750 °C compared to 600 °C).

In addition to differences in the substrates, film thickness and film stoichiometry affected the ability of the amorphous LAO films on STO-buffered Si(001) to crystallize.<sup>19</sup> Films that were  $< 2$  nm or  $> 40$  nm required annealing temperatures of 700 °C for 2 hr. LAO film composition can be adjusted by varying the number of La ALD cycles and Al ALD cycles. La-rich films ranging from 1.1 to 1.7 La:Al crystallize upon annealing at 600 °C for 2 h, whereas substoichiometric (*i.e.*, La:Al  $< 1$ ) required annealing temperatures of 700-750 °C.

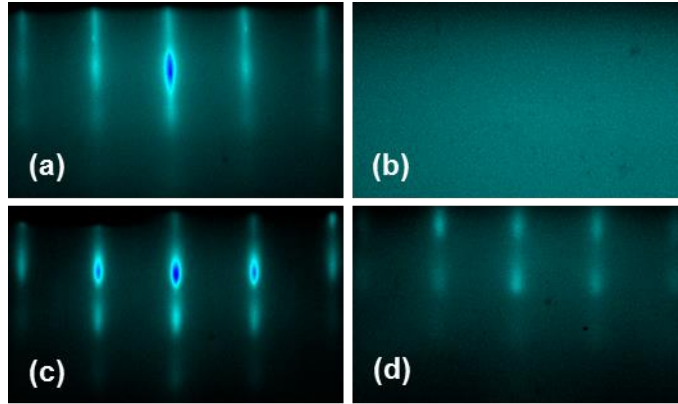


Figure 3.1. RHEED images of: (a) a four-unit-cell STO-buffered Si(001), (b) an as-deposited 10 nm LAO film on four-unit-cell STO-buffered Si(001), (c) the 10 nm LAO film grown on four-unit-cell STO-buffered Si(001) after annealing at 600 °C for 2 h, and (d) an 8 nm LAO film on STO substrate after annealing at 750 °C for 2 h. The beam was aligned along the  $\langle 110 \rangle$  azimuth for (a), (c) and (d).

Figure 3.2(a) presents the  $(\theta-2\theta)$  scans of a 10 nm thick LAO film annealed at 600 °C for 2 h (red curve),<sup>19</sup> and after an additional annealing at 750 °C for another 2 h. The pseudo cubic (001), (002) and (003) Bragg peaks are present, confirming the  $c$ -axis orientation of the crystalline LAO films.<sup>10,24,25</sup> There was no evidence of any other orientations or secondary phases. The Bragg peak positions of the film after annealing at 600 °C for 2 h and after additional annealing at 750 °C for another 2 h are identical indicating the lattice constant of LAO film still remained unchanged after additional annealing at 750 °C. The LAO (001) Bragg peak position at  $2\theta = 23.68^\circ$ , corresponds to an out-of-plane lattice constant of 3.75 Å, which is slightly reduced from the bulk pseudo cubic LAO lattice constant of 3.79 Å.<sup>26</sup> This is consistent with the LAO film being coherently strained to the underlying Si(001), which has a surface lattice constant of 3.84 Å. If the LAO is perfectly strained to the underlying silicon ( $a = 3.84$  Å), the out-of-plane lattice constant calculated using the reported value of Poisson's ratio of 0.25<sup>27,28</sup> should have a value of 3.76 Å. The XRD rocking curve around the (001) Bragg peak of the film

after annealing at 600 °C for 2 h shows a full-width at half-maximum (FWHM) of 0.23° [Figure 3.2(b)-red curve], indicating a high degree of crystallinity for the LAO film. Additional annealing of the film in vacuum at 750 °C for 2 h did not improve the crystallinity but rather worsened it, yielding a FWHM of 0.40° [Figure 3.2(b)-blue curve]. Annealing at 750 °C leads to interfacial reactions at the STO-Si(001) interface (see below), therefore, it is best to limit the annealing temperature as much as possible.

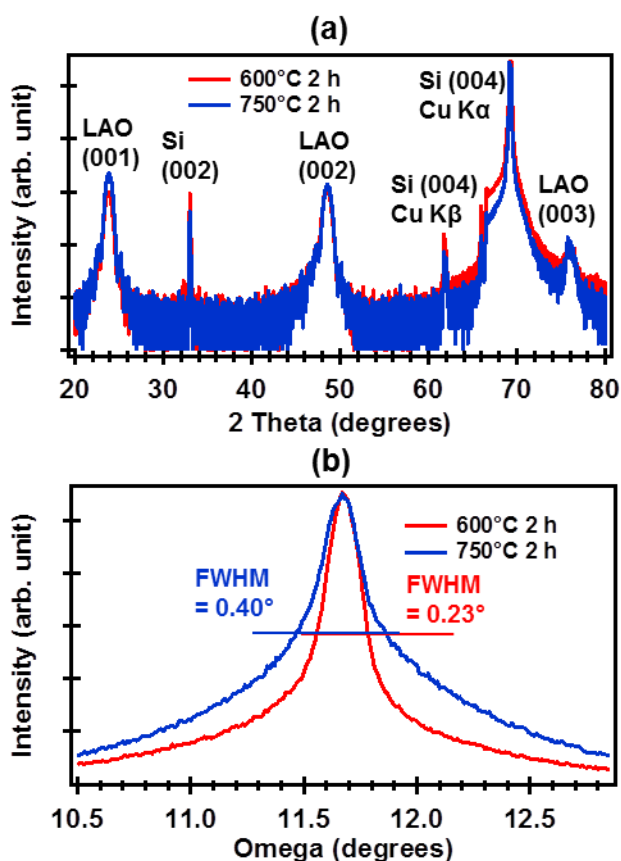


Figure 3.2. (a) X-ray diffraction patterns of a 10-nm thick LAO film grown by ALD on STO-buffered Si(001) at 250 °C after a 2 h vacuum anneal at 600 °C (red curve), and after an additional vacuum anneal at 750 °C for another 2 h (blue curve); (b) Rocking curves around the LAO(001) Bragg peak at a fixed  $2\theta=23.68^\circ$  for the 10-nm thick LAO film after annealing at 600 °C for 2 h (red) and after additional annealing at 750 °C for another 2 h (blue).

Figure 3.3 shows the XRD patterns around the LAO(001) Bragg peak of different LAO film thicknesses. The LAO(001) Bragg peaks for 7.5, 10, and 25 nm-thick LAO films were found to be at 23.72, 23.68 and 23.60°, corresponding to an out-of-plane lattice constant of 3.748, 3.754, and 3.767 Å, respectively. This indicates that the LAO films tend to be relaxed and the out-of-plane lattice constant approaches the bulk pseudo cubic LAO lattice constant of 3.79 Å as the film thickness increases.

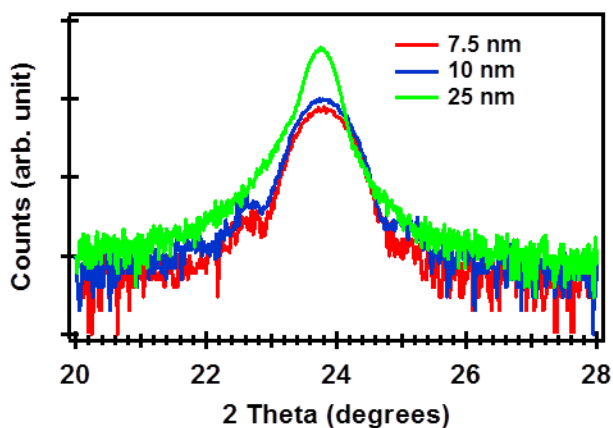


Figure 3.3. XRD patterns around LAO(001) Bragg peak of different LAO film thicknesses shows that thicker LAO films, LAO(100) Bragg peak was shifted to a lower  $2\theta$  values indicating the out-of-plane lattice constant of LAO tends to be closer to the bulk value (3.79 Å).

Figure 3.4 presents the ( $\theta$ - $2\theta$ ) scan of a 12 nm thick LAO film grown on STO(001) and annealed at 750 °C for 2 h. The LAO(001) Bragg peak is nearly coincident with the STO(001) Bragg peak making it difficult to deconvolute the contribution the LAO film makes to this diffraction feature. Deconvolution reveals a LAO(001) peak at 23.52° that leads to  $c$ -axis of 3.779 Å. This is quite close to the lattice constant of pseudo cubic LAO of 3.79 Å. A second weaker LAO(001) peak may occur at 24.01°, corresponding to a  $c$ -axis of 3.703 Å. STO has a lattice constant of 3.905 Å. It is possible

majority of the thick (12 nm) LAO film has relaxed during the high temperature annealing step and only a minor fraction is strained to the STO substrate. More studies are required to determine the relationship of film thickness on the strain remaining in the LAO grown on STO(001) after annealing.

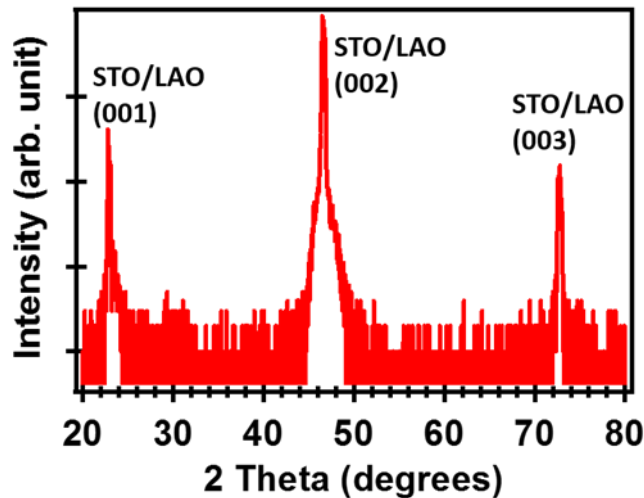


Figure 3.4. (a) X-ray diffraction patterns of a 12-nm thick LAO film grown by ALD on STO(001) at 250 °C after a 2 h vacuum anneal at 750 °C.

Figures 3.5(a) and 3.5(b) show the La 3*d* and Al 2*p* XP-spectra of a 5 nm LAO film on four-unit-cell STO-buffered Si(001) as-deposited (red curve) and after a 2 h vacuum anneal at 600 °C. All XP spectra were shifted by taking the Si 2*p* elemental peak to be at 99.3 eV. The La 3*d* XP-spectra in lanthanum-oxygen compounds are known to show a strong satellite peaks at a higher binding energy (about 4eV). The peak positions at the same binding energy before and after annealing were found for La and Al indicates that the La and Al oxidation states were unchanged after vacuum annealing. However, the intensity of the spectra is higher for crystalline LAO film indicating larger escape depth of crystalline versus amorphous LAO films.

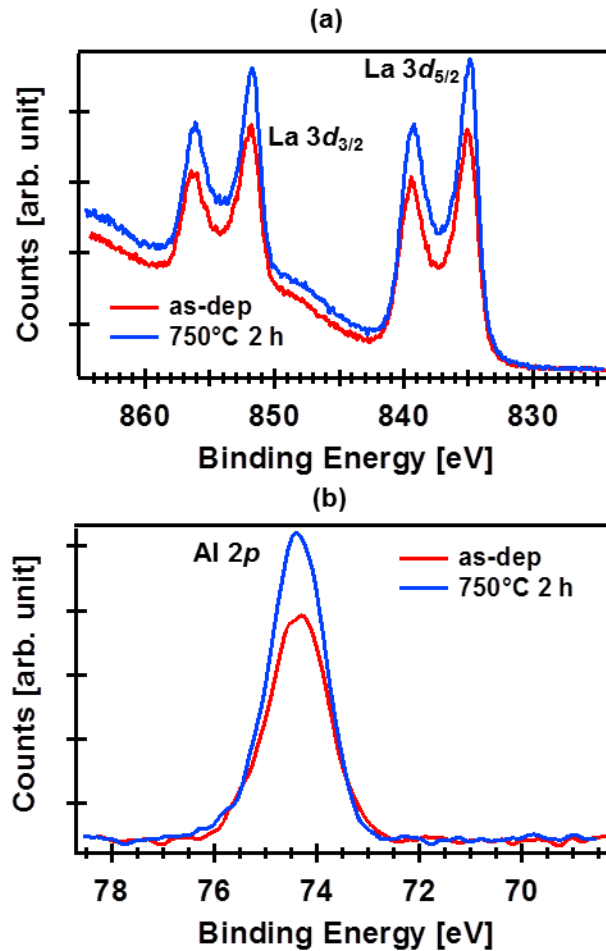


Figure 3.5. La 3d (a) and Al 2p (b) X-ray photoelectron spectra of a 5 nm LAO film on four-unit-cell STO-buffered Si(001) as-deposited (red curves) and after 2 h vacuum anneal at 750 °C (blue curves).

Figure 3.6(a) shows the O 1s X-ray photoelectron (XP) spectra of a 3 nm as-deposited LAO film on four-unit-cell STO-buffered Si(001). The blue curve with a binding energy of 530.3 eV represents for O in La<sub>2</sub>O<sub>3</sub>, while the purple curve at the binding energy of 531.2 eV represents for O in Al<sub>2</sub>O<sub>3</sub>. Crystalline LAO films was formed after a 2 h vacuum annealing at 750 °C, leading to the formation of one shaper oxygen peak at the binding energy of 530.7 eV as shown in Figure 3.6(b).

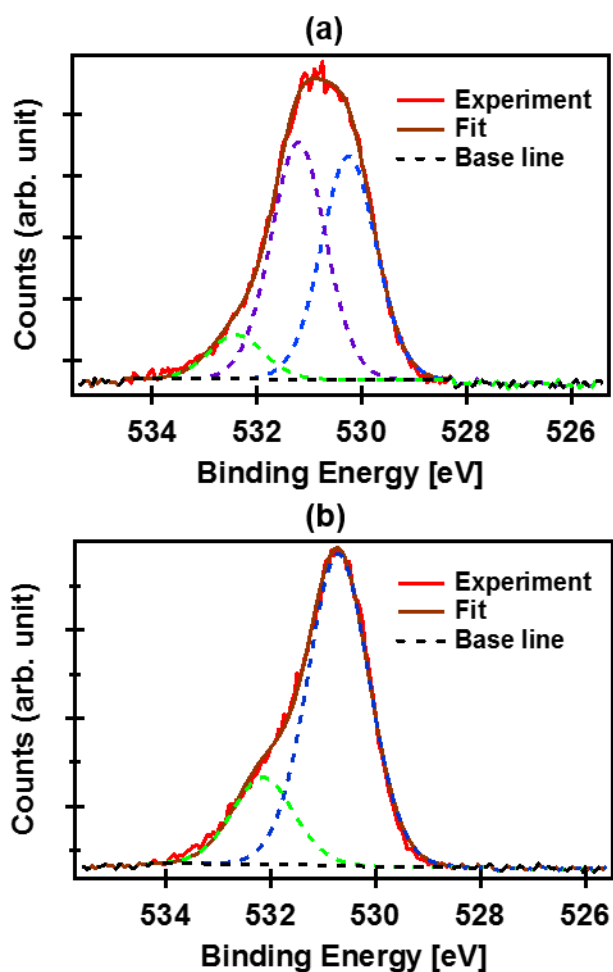


Figure 3.6. O 1s X-ray photoelectron spectra of a 3 nm LAO film on four-unit-cell STO-buffered Si(001) as-deposited (a) and after 2 h vacuum anneal at 750 °C (b). The dotted-curves show the fits for O in SiO<sub>x</sub> (green), La<sub>2</sub>O<sub>3</sub> ((a)-blue), LAO ((b)-blue), Al<sub>2</sub>O<sub>3</sub> (purple).

The results in Figures 5 and 6 indicate the LAO is thermally stable against reduction during annealing in vacuum. The STO however does begin to thermally decompose since the Si can oxidize for annealing temperatures of 600 °C and above. We previously reported on the interfacial reactions associated with the growth of LAO on STO-buffered Si(001).<sup>19</sup> ALD growth at 250 °C does not increase the amount of SiO<sub>x</sub> that is present after MBE growth of four-unit cells of STO. The ALD growth ambient

acts to more completely oxidize the Ti in STO. There is an increase in the SiO<sub>x</sub> content following annealing at 600 or 750 °C, and the higher temperature leads to more SiO<sub>x</sub>. Transmission electron microscopy images reveal an amorphous layer of 1 nm and 1.5 nm for 600 and 750 °C annealing, respectively.<sup>19</sup> Reduction of some of the Ti in the STO and the appearance of XPS peaks consistent with strontium silicates accompany the formation of the SiO<sub>x</sub> layer during annealing. In a separate study we report annealing at 600 °C for 5 min does not reduce the STO buffer layer and does not oxidize the STO-Si(001) interface.<sup>29</sup>

### **3.4. SUMMARY**

Crystalline LAO films have been grown on STO-buffered Si(001) substrates by ALD at 250 °C followed by annealing for 2 h at 600 °C under vacuum. Crystalline LAO films have also been grown on single crystal STO(001) at the same temperature and annealing for 2 h at 750 °C under vacuum. The crystallinity and epitaxial relationship were determined by RHEED and XRD. Higher annealing temperatures are required on STO since there is greater strain in films that are commensurate on STO than on Si. The results demonstrate that highly crystalline, epitaxial LAO films can be formed on STO-buffered Si with a minimal amorphous interfacial layer between STO/Si by maintaining the annealing temperature as low as possible.

### **3.5. REFERENCES**

- <sup>1</sup>J. Robertson, Rep. Prog. Phys. **69**, 327-396 (2006).
- <sup>2</sup>C. Zhao, C. Z. Zhao, M. Werner, S. Taylor, and P. R. Chalker, ISRN Nanotechnol. **2012**, 689023, 1–35 (2011).

- <sup>3</sup>A. Ohtomo, and H. Y. Hwang, *Nature* **427** 423–426 (2004).
- <sup>4</sup>Ariando, X. Wang, G. Baskaran, Z. Q. Liu, J. Huijben, J. B. Yi, A. Annadi, A. Roy Barman, A. Rusydi, S. Dhar, Y. P. Feng, J. Ding, H. Hilgenkamp, and T. Venkatesan, *Nat. Comm.* **2**, 188 (2011).
- <sup>5</sup>P. R. Willmott, S. A. Pauli, R. Herger, C. M. Schlepütz, D. Martoccia, B. D. Patterson, B. Delley, R. Clarke, D. Kumah, C. Cionca, and Y. Yacoby, *Phys. Rev. Lett.* **99**, 155502 (2007).
- <sup>6</sup>A. D. Caviglia, S. Gariglio, N. Reyren, D. Jaccard, T. Schneider, M. Gabay, S. Thiel, G. Hammerl, J. Mannhart, and J.-M. Triscone, *Nature* **456**, 624–627 (2008).
- <sup>7</sup>L. Li, C. Richter, J. Mannhart, and R. C. Ashoori, *Nat. Phys.* **7**, 762–766 (2011).
- <sup>8</sup>J. A. Bert, B. Kalisky, C. Bell, M. Kim, Y. Hikita, H. Hwang, K. A. Moler, *Nat. Phys.* **7**, 767–771 (2011).
- <sup>9</sup>N. Reyren, M. Bibes, E. Lesne, J.-M. George, C. Deranlot, S. Collin, A. Barthélémy, and H. Jaffrès, *Phys. Rev. Lett.* **108**, 186802 (2012).
- <sup>10</sup>J. W. Reiner, A. Posadas, M. Wang, M. Sidorov, Z. Krivokapic, F. J. Walker, T. P. Ma, and C. H. Ahn, *J. Appl. Phys.* **105**, 124501 (2009).
- <sup>11</sup>W. F. Xiang, H. B. Lu, Z. H. Chen, X. B. Lu, M. He, H. Tian, Y. L. Zhou, C. R. Li, and X. L. Ma, *J. Cryst. Growth* **271**, 165–170 (2004).
- <sup>12</sup>C. Merckling, G. Delhaye, M. El-Kazzi, S. Gaillard, Y. Rozier, L. Rapenne, B. Chenevier, O. Marty, G. Saint-Girons, M. Gendry, Y. Robach, and G. Hollinger, *Microelectro. Relia.* **47**, 540–543 (2007).
- <sup>13</sup>Y. Y. Mi, Z. Yu, S. J. Wang, P. C. Lim, Y. L. Foo, A. C. H. Huan, and C. K. Ong, *Appl. Phys. Lett.* **90**, 181925 (2007).
- <sup>14</sup>A. Posadas, R. Dargis, M. Choi, A. Slepko, J. J. Kim, D. J. Smith, and A. A. Demkov, *J. Vac. Sci. Technol. B* **29**, 1071 (2011).

- <sup>15</sup>K. Kukli, M. Ritala, V. Pore, M. Leskelä, T. Sajavaara, R. I. Hegde, D. C. Gilmer, P. J. Tobin, A. C. Jones, and H. C. Aspinall, *Chem. Vap. Deposition* **12**, 158–164 (2006).
- <sup>16</sup>G. Congedo, S. Spiga, L. Lamagna, A. Lamperti, Y. Lebedinskii, Y. Matveyev, A. Zenkevich, P. Chernykh, and M. Fanciulli, *Microelectro. Engin.* **86**, 1696–1699 (2009).
- <sup>17</sup>D. Eom, C. S. Hwang, H. J. Kim, M.-H. Cho, and K. B. Chung, *Electrochem. Solid-State Lett.* **11**, G33–G36 (2008).
- <sup>18</sup>D. H. Triyoso, R. I. Hegde, J. M. Grant, J. K. Schaeffer, D. Roan, B. E. White, and P. J. Tobin, *J. Vac. Sci. Technol. B* **23**, 288, 1–10 (2005).
- <sup>19</sup>T. Q. Ngo, A. Posadas, M. D. McDaniel, D. A. Ferrer, J. Bruley, C. Breslin, A. A. Demkov, and J. G. Ekerdt, *J. Cryst. Growth* **363**, 150–157 (2013).
- <sup>20</sup>H. K. Sato, C. Bell, Y. Hikita, and H. Y. Hwang, *Appl. Phys. Lett.* **102**, 251602 (2013).
- <sup>21</sup>M. P. Warusawithana, C. Richter, J. A. Mundy, P. Roy, J. Ludwig, S. Paetel, T. Heeg, A. A. Pawlicki, M. Zheng, M. Lee, B. Mulcahy, W. Zander, Y. Zhu, J. Schubert, J. N. Eckstein, D. A. Muller, C. S. Hellberg, J. Mannhart, and D. G. Schlom, *Nature Comm.* **4**, 2351 (2013).
- <sup>22</sup>M. Choi, A. Posadas, R. Dargis, C.-K. Shih, A. A. Demkov, D. H. Triyoso, N. D. Theodore, C. J. Dubourdieu, J. Bruley, and J. Jordan-Sweet, *J. Appl. Phys.* **111**, 064112 (2012).
- <sup>23</sup>M. D. McDaniel, A. Posadas, T. Wang, A. A. Demkov, and J. G. Ekerdt, *Thin Solid Film* **520** 6525–6530 (2012).
- <sup>24</sup>N. M. Sbrockey, M. Luong, E. M. Gallo, J. D. Sloppy, G. Chen, C. R. Winkler, S. H. Johnson, M. L. Taheri, G. S. Tompa, and J. E. Spanier, *J. Electro. Mater.* **41**, 819–823 (2012).
- <sup>25</sup>M. Nieminen, T. Sajavaara, E. Rauhala, M. Putkonen, and L. Niinistö, *J. Mater. Chem.* **11**, 2340–2345 (2011).

<sup>26</sup>G. W. Berkstresser, A. J. Valentino, and C. D. Brandle, *J. Cryst. Growth* **109**, 457–466 (1991).

<sup>27</sup>X. Luo and B. Wang, *J. Appl. Phys.* **104**, 073518 (2008).

<sup>28</sup>S. A. Pauli, S. J. Leake, B. Delley, M. Bjorck, C. W. Schneider, C. M. Schleputz, D. Martoccia, S. Paetel, J. Mannhart, and P. R. Willmott, *Phys. Rev. Lett.* **106**, 023101 (2011).

<sup>29</sup>T. Q. Ngo, A. B. Posadas, M. D. McDaniel, C. Hu, J. Bruley, E. T. Yu, A. A. Demkov, and J. G. Ekerdt, *Appl. Phys. Lett.* **104**, 082910 (2014).

## Chapter 4: Epitaxial *c*-axis oriented BaTiO<sub>3</sub> thin films on SrTiO<sub>3</sub> buffered Si(001) by atomic layer deposition

### 4.1. INTRODUCTION

The ability to grow SrTiO<sub>3</sub> (STO) epitaxially on Sr-passivated Si(001) using molecular beam epitaxy (MBE)<sup>1</sup> has opened up a pathway to integrate functional oxides onto silicon for the next generation of photonic and electronic devices. Over the years, a variety of functional perovskite oxides including BaTiO<sub>3</sub> (BTO) have been integrated on Si through this approach.<sup>2-9</sup> Ferroelectric BTO has several advantages for non-volatile ferroelectric memory applications compared to other candidates (*e.g.*, PbZrTiO<sub>3</sub>, SrBi<sub>2</sub>Ta<sub>2</sub>O<sub>5</sub>) particularly due to its non-toxic elements, better compatibility with integrated circuit fabrication, and lower fatigue effects.<sup>6,9-13</sup> Ferroelectricity is fundamentally associated with the BTO structural phase transition at the Curie temperature ( $T_C = 120$  °C); above  $T_C$ , BTO is a paraelectric cubic perovskite ( $a_{\text{BTO}(c)} = 4.005$  Å) and below  $T_C$ , it is a tetragonal ferroelectric ( $a_{\text{BTO}(t)} = 3.992$  Å and  $c_{\text{BTO}(t)} = 4.036$  Å) with a spontaneous polarization along the *c*-axis.<sup>6</sup>

The effort to integrate BTO directly on Si(001) is challenging due to the large lattice mismatch between BTO and Si (4.0 and 4.4% below and above  $T_C$ , respectively) and the reaction of Si with oxygen to form an amorphous layer that inhibits epitaxial growth. The idea of employing crystalline STO as a buffer layer to integrate BTO on Si has been demonstrated by using MBE.<sup>6,9,11,14,15</sup> However, MBE growth is performed at relatively high temperatures and in the presence of oxygen, leading to the formation of a significant amorphous SiO<sub>x</sub> layer at the STO/Si interface.<sup>12,16</sup> The formation of this SiO<sub>x</sub> layer may be undesirable in applications because it is in series with the perovskite films.

Moreover, the mismatch between the thermal expansion coefficients of BTO/STO and Si tends to favor a polar axis lying in-plane rather than out-of-plane as the stacks are cooled down.<sup>14,17</sup>

It has recently been proposed that the incorporation of a ferroelectric as a gate oxide could decrease the subthreshold slope below the intrinsic thermodynamic limit of  $60 \text{ mV dec}^{-1}$  at room temperature in metal-oxide-semiconductor field effect transistors,<sup>18</sup> enabling even lower voltage operation of electronic devices. The moderate Curie temperature of BTO may be an advantage in this case as reported by a recent proof-of-concept demonstration of negative capacitance in  $\text{Pb}(\text{Zr}_{0.2}\text{Ti}_{0.8})\text{O}_3/\text{SrTiO}_3$  metal-insulator-metal heterostructures.<sup>19</sup> The epitaxial growth of tetragonal BTO on Si with out-of-plane polarization in a metal-ferroelectric-semiconductor stack has been reported by a limited number of groups<sup>6,11,14,15</sup> and without a metallic contact by our group.<sup>9</sup> In this letter, we report a low temperature chemical means of growing *c*-axis oriented BTO films with thicknesses ranging from 7-20 nm on thin (1.6 nm) STO-buffered Si(001) substrates. By keeping the substrate temperature below 225 °C during the deposition process, we are able to (i) maintain a clean STO/Si interface, free from  $\text{SiO}_2$  and (ii) practically eliminate the effects of the difference of thermal expansion coefficients on the polarization orientation. Capacitance-voltage (C-V) measurements are also performed to demonstrate the dielectric properties of ALD-grown epitaxial BTO.

## 4.2. EXPERIMENTAL

The 1.6-nm STO templates were grown on Si(001) by MBE using the Motorola-derived process, as described in more detail elsewhere.<sup>16,20</sup> Reflection high energy electron diffraction (RHEED) with an electron energy of 21 keV at a glancing angle of ~

3° is used to monitor in real time the crystallinity and surface morphology of the films. The STO-buffered Si(001) substrates were then transferred *in-situ* to the ALD chamber for chemical deposition of BTO. The ALD system is a custom built, hot-wall stainless steel rectangular 20-cm long chamber, with a reactor volume of 460 cm<sup>3</sup>.<sup>21</sup> Ultrahigh purity argon was used as a purge/carrier gas. BTO films were grown using barium bis(triisopropylcyclopentadienyl), titanium tetraisopropoxide as metal sources, and with water as the oxidant. The Ba and Ti precursors were held at 135 and 34 °C, respectively. The substrate temperature was maintained at 225 °C, while the working pressure was maintained at 1 Torr. *In-situ* X-ray photoelectron spectroscopy (XPS) using a VG Scienta R3000 analyzer was used to determine the film composition within an error less than 5%. A single-crystal BTO substrate from MTI, where the Ba:Ti ratio was assumed to be 1:1, was used as a standard for determining the Ba:Ti ratio of ALD-grown BTO films. The Ba:Ti ratio was adjusted by changing the cycle ratio  $x\text{Ba}:y\text{Ti}$ . The stoichiometry of the ALD-grown BTO films reported herein was found to be 1.1:1 (Ba:Ti) using an  $x=3, y=4$  cycle ratio. Each Ba or Ti unit-cycle consisted of a 2 s pulse of the Ba or Ti precursor, respectively, a 15 s purge of Ar, a 1 s dose of water, and a 15 s purge of Ar (noted as “2/15/1/15”). The BTO films were crystalline as-deposited. Films with varying Ba:Ti ratio were grown by changing the cycle ratio  $x:y$ . It was found that the Ba-rich BTO films (up to 1.4:1 Ba:Ti) were also crystalline as-deposited, while the Ti-rich BTO films (up to 0.85:1 Ba:Ti) were amorphous even after vacuum annealing.

The film thickness and the growth rate were determined by X-ray reflectivity (XRR). X-ray diffraction (XRD) was used to determine the out-of-plane lattice constants and the crystalline quality. Two dimensional XRD was also performed to determine both the in-plane and out-of-plane lattice constants of the films. XRR and XRD were performed using an X'PERT diffractometer with a sealed-tube Cu K $\alpha$  radiation source.

Scanning transmission electron microscopy (STEM) was also performed to confirm the crystallinity and the nature of the STO/Si interface after BTO growth. The STEM observations were carried out using an FEI TITAN instrument. The STEM samples were prepared by FIB using standard *in-situ* lift out techniques; a capping layer of e-beam deposited Pt followed by ion beam Pt is put down. The sample is then cut using a 30 kV followed by a 5 kV Ga beam. C-V characterization of capacitor structures was performed using a Keithley 590 Analyzer interfaced to a Keithley 4200 Semiconductor Characterization System. Ti/Au top contacts (10-200  $\mu\text{m}$  radius) were fabricated using photolithography, metallization via e-beam evaporation, and lift-off. For the bottom contact, the backside of Si substrates were scraped with a scalpel and placed on a copper block using a layer of In-Ga eutectic alloy in between. The bias was applied to the gold electrode, while the copper block was grounded.

### 4.3. RESULTS AND DISCUSSION

The growth of BTO on Si with a native oxide was first performed to determine the effect of varying the cycle ratio on stoichiometry. Near stoichiometric 1.1:1 Ba:Ti composition was established using ALD cycle conditions of {Ba: 2/15/1/15 $\times$  1, Ti: 2/15/1/15 $\times$  1, Ba: 2/15/1/15  $\times$  1, Ti: 2/15/1/15  $\times$  1, Ba: 2/15/1/15  $\times$  1, and Ti: 2/15/1/15  $\times$  2}  $\times$  number of ALD super-cycles. These BTO films were amorphous. The same ALD cycle conditions were then used to grow BTO on 1.6-nm STO-buffered Si(001). The BTO samples were characterized using *in-situ* RHEED after ALD growth and throughout the annealing processes. RHEED patterns of a 7-nm BTO film as-deposited and after a 5-min vacuum anneal at 600  $^{\circ}\text{C}$  taken along the [110] azimuth of STO are shown in Figures 4.1(a) and (b), respectively. Both images show well-defined streaks indicating the high

degree of crystalline order in the ALD BTO films. Sharper streaks in Figure 4.1(b) compared to those of Figure 4.1(a) indicate improvement in the crystallinity of post-deposition annealed films. XRR measurements found that the growth rate of amorphous BTO is 0.6 Å/unit-cycle, while the growth rate of crystalline BTO is 0.9Å/unit-cycle. This indicates that the crystalline surface enhances the BTO growth rate similar to what we observed with STO films grown by ALD.<sup>22</sup>

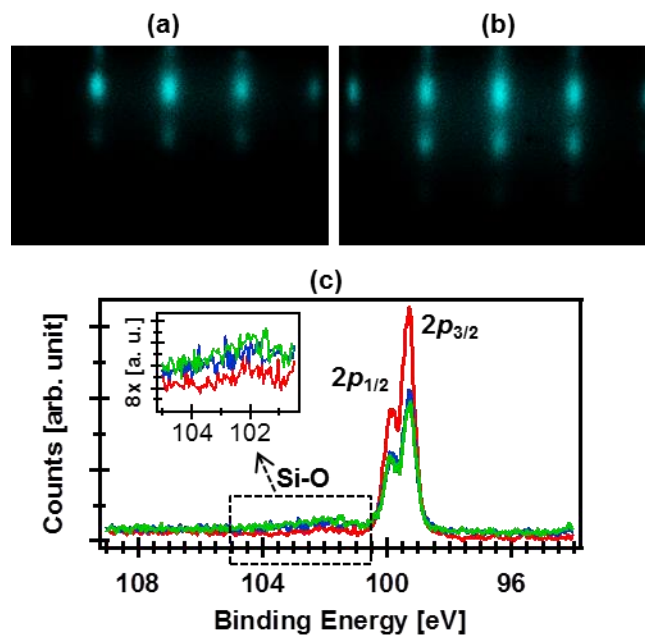


Figure 4.1. (a) and (b) are RHEED patterns of a 7 nm BTO film on four-unit-cell STO-buffered Si(001) as-deposited and after 5 min vacuum anneal at 600 °C, respectively. Both images are taken along  $\langle 110 \rangle$  direction of STO. (c) Si 2p XP spectra of a typical four-unit-cell STO-buffered Si(001) film (red), a 3 nm ALD BTO film on four-unit-cell STO-buffered Si(001) as-deposited (blue), and the 3 nm BTO film after a 5 min vacuum anneal at 600 °C (green). Please note that there is a negligible change in Si-O bonding before and after the vacuum anneal, so the blue and green lines are almost identical.

A thinner (3 nm) BTO film was deposited on STO-buffered Si(001) to study the STO/Si interface throughout the ALD and annealing processes using *in-situ* XPS. With

the initial 1.6 nm MBE-grown STO on Si(001), a small amount of Si-O (silicate) bonding at the STO/Si interface can be observed prior to ALD growth, as shown by the red color in Figure 4.1(c) with a binding energy of 102 eV. There is a negligible change in Si-O bonding after ALD growth and after vacuum annealing (Figure 4.1(c) - blue and green colors), demonstrating the ability of ALD to maintain a clean STO/Si interface.

XRD was used to determine the crystalline structure of ALD-grown BTO films on STO-buffered Si(001). Figure 4.2(a) shows  $\theta$ - $2\theta$  scan of an as-deposited 20-nm thick BTO on 1.6-nm STO-buffered Si(001). The (001), (002) Bragg peaks from BTO are present, confirming the  $c$ -axis orientation of the BTO layer. The (002) Bragg peak position at  $2\theta = 45.10^\circ$ , corresponds to an out-of-plane lattice constant of  $4.018 \text{ \AA} \pm 0.005$ , which is slightly bigger than the bulk value of BTO cubic structure ( $4.005 \text{ \AA}$ ). Figure 4.2(b) shows a reciprocal space map around the (103) BTO Bragg peak. A two-dimensional Gaussian fit was used to find the center of the peak, which was found to be at  $2\theta = 74.632^\circ$  and  $\omega = 18.472^\circ$ . This corresponds to in-plane and out-of-plane lattice constants of  $a = 3.93 \pm 0.01$  and  $c = 4.02 \pm 0.01 \text{ \AA}$ , respectively. Different thicknesses of BTO films were grown to study the dependence of the  $c$  lattice constant on thickness. It is found that for film thickness ranging from 7 to 20 nm, the  $c$  lattice constant varies from 4.095 to  $4.018 \pm 0.005 \text{ \AA}$ , consistent with BTO relaxation with increasing thickness. An XRD rocking curve around the (002) Bragg peak produced a full-width at half-maximum (FWHM) of  $0.91^\circ$  indicating reasonable crystallinity of the as-deposited BTO films. The  $\phi$ -scan indicates that there is an in-plane  $45^\circ$  rotation of the BTO film with respect to Si suggesting that the BTO [100] direction is parallel to the Si [110] direction.

To study the effect of post-deposition annealing on the BTO crystalline structure, the 20-nm BTO film was annealed at  $600^\circ\text{C}$  for 5 min with a ramping rate of  $30^\circ\text{C}/\text{min}$ . The sample was cooled below  $80^\circ\text{C}$  before unloading. The (002) Bragg peak of the

annealed film shifted to a position  $2\theta = 45.42^\circ$ , corresponding to an out-of-plane lattice constant of  $3.990 \pm 0.005 \text{ \AA}$ . The (103) reciprocal space map was re-examined and showed that the lattice constants were now  $a = 4.01$  and  $c = 4.00 \pm 0.01 \text{ \AA}$ . This indicates that the  $c$ -axis orientation is lost under this post-deposition annealing condition. The rocking curve around this (002) Bragg peak, however, now has a smaller FWHM value ( $0.74^\circ$ ) indicating improved crystallinity.

To study the effect caused by the difference in thermal expansion coefficients between perovskites and Si on the BTO crystalline structure, a 7-nm tetragonal BTO film ( $c = 4.095 \pm 0.005 \text{ \AA}$ ) was annealed at  $600 \text{ }^\circ\text{C}$  for 5 min with a ramping rate of  $5^\circ/\text{min}$ . An XRD  $\theta$ - $2\theta$  scan found the out-of-plane lattice constant to be  $4.045 \pm 0.005 \text{ \AA}$  after annealing. This shows that by keeping ramping rate low ( $5^\circ/\text{min}$ ), we can minimize the effects of thermal expansion mismatch on the crystalline structure of tetragonal BTO.

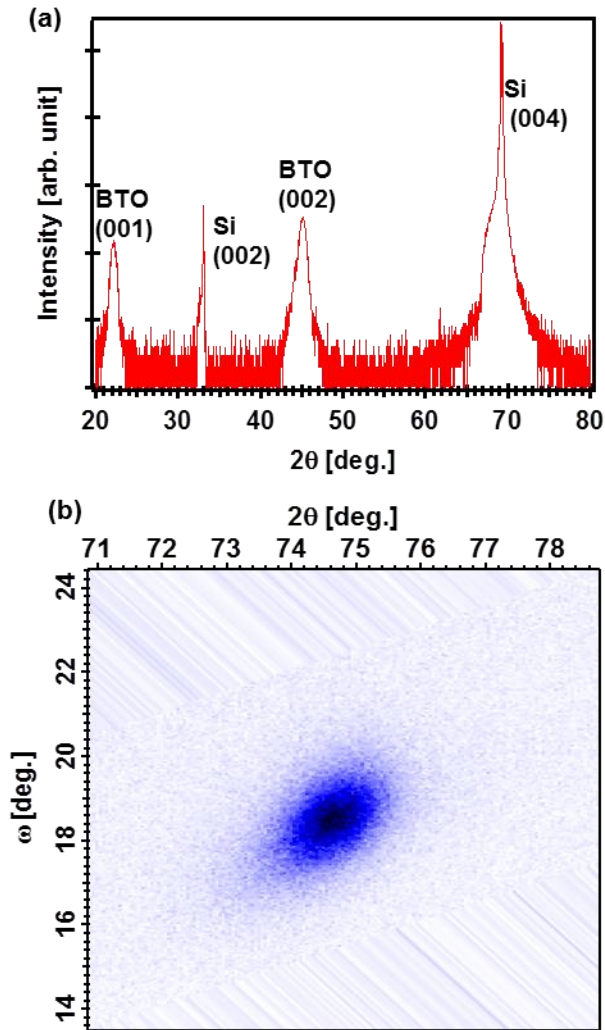


Figure 4.2. (a) XRD and (b) 2D-XRD patterns of an as-deposited 20 nm ALD BTO film on four-unit-cell MBE STO on Si(001). The lattice constants of the BTO film calculated from XRD are  $a = 3.93 \text{ \AA}$  and  $c = 4.02 \pm 0.01 \text{ \AA}$  demonstrating tetragonal structure of the as-deposited BTO film.

Figure 4.3 shows a cross-sectional Z-contrast STEM image of a 17 nm ALD-grown BTO film on 1.6-nm STO-buffered Si(001) after 5 min vacuum anneal at 600 °C. The high degree of crystallinity of the BTO and STO layers and the abrupt STO/Si interface can be seen. No amorphous layer is observable at the interface. The image also shows that the BTO/STO interface is very sharp. The good crystalline order and very

clean STO/Si interface (no amorphous layer) are consistent with RHEED, XRD, and XPS analyses.

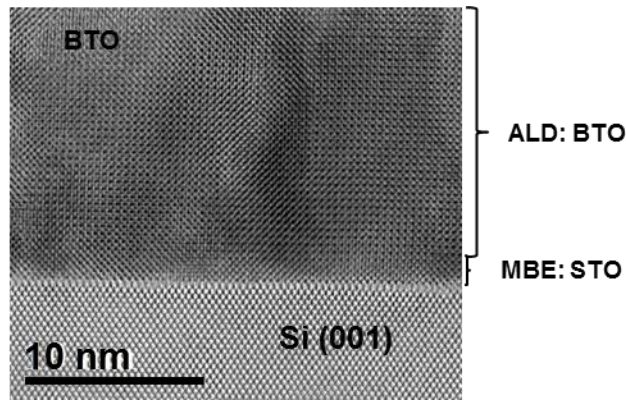


Figure 4.3. STEM image of a 17 nm ALD-grown BTO film on four-unit-cell MBE-grown STO-buffered Si(001) after a 5 min vacuum anneal at 600 °C.

C-V measurements at 100 kHz were performed on an 18-nm as-deposited BTO film, the results of which are shown in Figure 4.4. The forward voltage sweep (-1.7 to +1.7 V, 10 mV/step, 0.5 V/s) and reverse sweep (+1.7 to -1.7 V, 10 mV/step, 0.5 V/s) curves are approximately identical, with no significant hysteresis observed. The ferroelectric coercive field for BTO is commonly reported to be very low with a typical value of 500V/cm.<sup>23,24</sup> Even if the BTO film were ferroelectric, the low coercivity combined with the film thickness is expected to result in a hysteresis width of <10 mV. Therefore, the coercive field in the C-V data is inconclusive concerning ferroelectricity of the BTO film. The relative dielectric constant calculated from the accumulation side of the C-V curve was found to be ~660, consistent with previous reports for BTO thin films.<sup>25,26</sup>

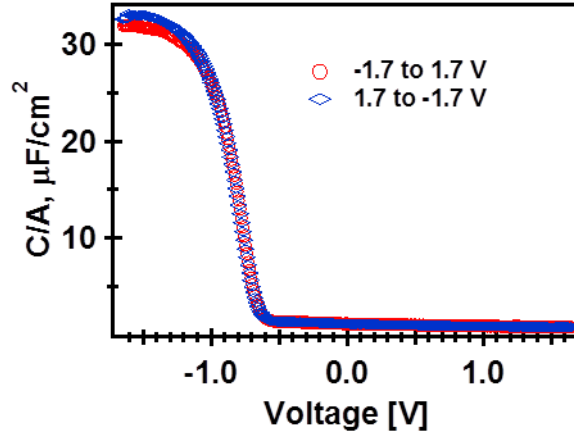


Figure 4.4. C-V(at 100 kHz) characteristics of an as-deposited 18 nm BTO film on 1.6 nm STO-buffered Si(001).

#### 4.4. SUMMARY

In conclusion, we have grown *c*-axis oriented epitaxial BTO at 225 °C using ALD on 1.6-nm STO-buffered Si(001). The BTO films have a good degree of crystallinity and no amorphous layer was observed at the STO/Si interface. A 5-min vacuum anneal at 600 °C significantly improved BTO crystallinity. Annealing using a relatively high temperature ramping rate (30 °C/min) could destroy the tetragonal structure, while annealing using a lower ramping rate (5 °C/min) is able to maintain the *c*-axis orientated tetragonal structure. The dielectric constant of the BTO/STO stack on Si was estimated to be ~660. We expect the ALD method of growing *c*-axis oriented epitaxial BTO on STO-buffered Si(001) at low temperature to be a potential way to fabricate the negative capacitance gate oxide structure on Si with no amorphous layer between STO and Si in the near future.

#### 4.5. REFERENCES

- <sup>1</sup>R. A. McKee, F. J. Walker, and M. F. Chisholm, *Phys. Rev. Lett.* **81**, 3014 (1998).
- <sup>2</sup>J. W. Reiner, A. M. Kolpak, Y. Segal, K. F. Garrity, S. Ismail-Beigi, C. H. Ahn, and F. J. Walker, *Adv. Mater.* **22**, 2919 (2010).
- <sup>3</sup>H. Li, X. Hu, Y. Wei, Z. Yu, X. Yang, R. Droopad, A. A. Demkov, J. Erwards, K. Moore, W. Ooms, J. Kulik, and P. Fejes, *J. Appl. Phys.* **39**, 4521 (2003).
- <sup>4</sup>Z. Yu, J. Ramdani, J. A. Curless, C. D. Overgaard, J. M. Finder, R. Droopad, K. W. Eisenbeiser, J. A. Hallmark, W. J. Ooms, and V. S. Kaushik, *J. Vac. Sci. Technol. B* **18**, 2139 (2000).
- <sup>5</sup>J. W. Reiner, A. Posadas, M. Wang, M. Sidorov, Z. Krivokapic, F. J. Walker, T. P. Ma, and C. H. Ahn, *J. Appl. Phys.* **105**, 124501 (2009).
- <sup>6</sup>C. Merckling, G. Saint-Girons, C. Botella, G. Hollinger, M. Heyns, J. Dekoster, and M. Caymax, *Appl. Phys. Lett.* **98**, 092901 (2011).
- <sup>7</sup>H. Seo, A. B. Posadas, C. Mitra, A. V. Kvit, J. Ramdani, and A. A. Demkov, *Phys. Rev. B* **86**, 075301 (2012).
- <sup>8</sup>A. Posadas, M. Berg, H. Seo, D. J. Smith, H. Celio, A. P. Kirk, D. Zhernokletov, R. M. Wallace, A. de Lozanne, and A. A. Demkov, *Appl. Phys. Lett.* **98**, 055104 (2011).
- <sup>9</sup>C. Dubourdieu, J. Bruley, T. M. Arruda, A. Posadas, J. Jordan-Sweet, M. M. Frank, E. Cartier, D. J. Frank, S. V. Kalinin, A. A. Demkov, and V. Narayanan, *Nature Nanotechnology* **8**, 748 (2013).
- <sup>10</sup>J. Y. Jo, Y. S. Kim, T. W. Noh, J.-G. Yoon, and T. K. Song, *Appl. Phys. Lett.* **89**, 232909 (2006).
- <sup>11</sup>V. Vaithyanathan, J. Lettieri, W. Tian, A. Sharan, A. Vasudevarao, Y. L. Li, A. Kochhar, H. Ma, J. Levy, P. Zschack, J. C. Woicik, L. Q. Chen, V. Gopalan, and D. G. Schlom, *J. Appl. Phys.* **100**, 024108 (2006).

- <sup>12</sup>S. Abel, T. Stöferle, C. Marchiori, C. Rossel, M. D. Rossell, R. Erni, D. Caimi, M. Sousa, A. Chelnokov, B. J. Offrein, and J. Fompeyrine, *Nat. Commun.* **4**, 1671 (2013).
- <sup>13</sup>X. L. Li, H. B. Lu, M. Li, Z. Mai, H. Kim, and Q. J. Jia, *Appl. Phys. Lett.* **92**, 012902 (2008).
- <sup>14</sup>F. Niu and B. W. Wessels, *J. Vac. Sci. Technol. B* **25**, 1053 (2007).
- <sup>15</sup>G. Niu, S. Yin, G. Saint-Girons, B. Gautier, P. Lecoœur, V. Pillard, G. Hollinger, and B. Vilquin, *Microelectron. Eng.* **88**, 1232 (2011).
- <sup>16</sup>M. Choi, A. Posadas, R. Dargis, C. -K. Shih, A. A. Demkov, D. H. Triyoso, N. D. Theodore, C. Dubourdieu, J. Bruley, and J. Jordan-Sweet, *J. Appl. Phys.* **111**, 064112 (2012).
- <sup>17</sup>S. Abel, M. Sousa, C. Rossel, D. Caimi, M. D. Rossell, R. Erni, J. Fompeyrine, and C. Marchiori, *Nanotechnol.* **24**, 285701 (2013).
- <sup>18</sup>S. Salahuddin and S. Datta, *Nano Lett.* **8**, 405 (2008).
- <sup>19</sup>A. I. Khan, D. Bhowmik, P. Yu, S. J. Kim, X. Pan, R. Ramesh, and S. Salahuddin, *Appl. Phys. Lett.* **99**, 113501 (2011).
- <sup>20</sup>Z. Yu, J. Ramdani, J. A. Curless, J. M. Finder, C. D. Overgaard, R. Droopad, K. W. Eisenbeiser, J. A. Hallmark, W. J. Ooms, J. R. Conner, and V. S. Kaushik, *J. Vac. Sci. Technol. B* **18**, 1653 (2000).
- <sup>21</sup>M. D. McDaniel, A. Posadas, T. Wang, A. A. Demkov, and J. G. Ekerdt, *Thin Solid Films* **520**, 6525 (2012).
- <sup>22</sup>M. D. McDaniel, A. Posadas, T. Q. Ngo, A. Dhamdhare, D. J. Smith, A. A. Demkov, and J. G. Ekerdt, *J. Vac. Sci. Technol. A* **31**, 01A136 (2013).
- <sup>23</sup>W. J. Merz, *Phys. Rev.* **95**, 690 (1954).
- <sup>24</sup>R. A. Mckee, F. J. Walker, and M. F. Chisholm, *Science* **293**, 468 (2001).

<sup>25</sup>J. P. George, J. Beeckman, W. Woestenborghs, P. F. Smet, W. Bogaerts, and K. Neyts, *Nanoscale Res. Lett.* **8**:62, 1–7 (2013).

<sup>26</sup>P. R. Arya , P. Jha, G. N. Subbanna, and A. K. Ganguli, *Mater. Res. Bull.* **38**, 617 (2003).

## **Chapter 5: Quasi-Two-Dimensional Electron Gas at the Interface of $\gamma$ - $\text{Al}_2\text{O}_3/\text{SrTiO}_3$ Heterostructures Grown by Atomic Layer Deposition**

### **5.1. INTRODUCTION**

Oxide materials play a very important role and are present in the majority of current electronic devices.<sup>1-3</sup> Oxides exhibit a broad range of behavior from insulating to metallic, with many also being ferromagnetic, ferroelectric, and/or superconducting, depending on their composition and crystal structure. The fabrication of heteroepitaxial structures of these functional oxides enables one to explore the fundamental materials physics and the possibility of new technology applications. When different oxides are brought together in an atomically intimate manner, a wide range of phenomena not found in bulk materials occur at their interface.<sup>4,5</sup> The most obvious effect at an interface is “symmetry breaking” of the charge, spin, orbital, and lattice symmetry, which leads to the modification of electronic and structural properties. These emergent properties of oxide heterostructure interfaces can be exploited, potentially yielding devices with novel functionalities.

The epitaxial interface between  $\text{LaAlO}_3$  (LAO) and  $\text{SrTiO}_3$  (STO) has been found to exhibit a two-dimensional electron gas (2-DEG) with sufficiently high mobility to exhibit Shubnikov-de Haas oscillations.<sup>6,7</sup> Electrons are confined near the interface for epitaxial LAO films grown by either pulsed laser deposition (PLD) or molecular beam epitaxy (MBE) on  $\text{TiO}_2$ -terminated STO substrates. Devices based on this phenomenon have already been proposed.<sup>8,9</sup> One explanation for 2-DEG formation at the LAO/STO interface is based on electronic reconstruction, in which electrons move to the interface to avoid the divergence in potential known as the polar catastrophe.<sup>10</sup> The electronic

reconstruction yields a  $\text{Ti}^{3+}$  signal in photoemission that arises from the presence of electrons in the STO conduction band.<sup>6-11</sup> An alternative explanation for the generation of a 2-DEG is due to La interdiffusion across the interface, doping the STO interface with electrons.<sup>12</sup> A third explanation is oxygen vacancy accumulation on the STO side of the interface.<sup>12,13</sup>

It has been discovered that a 2-DEG could also be formed by growing amorphous LAO layers on  $\text{TiO}_2$ -terminated STO substrates.<sup>14,15</sup> 2-DEGs have also been observed for Al-based amorphous oxide/STO interfaces. The Al-based oxides were grown by atomic layer deposition (ALD) using trimethylaluminum (TMA) and water at 300 °C. The formation of a 2-DEG in this case was attributed to the formation of oxygen vacancies on the STO side of the oxide/STO interface, which were formed during the film growth process.<sup>15</sup> The conductivity of amorphous oxide/STO interfaces vanishes after air/oxygen atmosphere annealing.<sup>15</sup> Recently, it has been reported that oxygen vacancies are the dominant source of mobile carriers when the overlayer is amorphous LAO, and that both oxygen vacancies and the polar catastrophe contribute to the conducting interface in crystalline LAO/STO heterostructures.<sup>16</sup> In addition to the LAO/STO system, a 2-DEG with extremely high electron mobility at 2 K ( $> 100,000 \text{ cm}^2\text{V}^{-1}\text{s}^{-1}$ ) has been reported at the spinel  $\gamma\text{-Al}_2\text{O}_3$ /STO interface.<sup>17</sup> We have also observed the formation of a conductive interface layer in MBE-grown  $\gamma\text{-Al}_2\text{O}_3$ /STO interface.<sup>18</sup>

Oxide 2-DEGs could provide opportunities for the fabrication of all-oxide electronic devices. To date, high mobility 2-DEGs at crystalline oxide interfaces have been fabricated at temperatures higher than 600 °C by physical vapor deposition methods (PLD and MBE). However, it still remains a challenge to design all-oxide electronic devices due to the high temperature needed for the growth of the crystalline oxide layers. More recently, Chen *et al.* have reported room temperature formation of a high mobility

2-DEG at the  $\gamma$ -Al<sub>2</sub>O<sub>3</sub>/STO interface grown by PLD.<sup>19</sup> ALD offers a chemical route for the deposition of crystalline oxides at lower temperatures. Furthermore, for device manufacturing applications, ALD has advantages over PLD and MBE due to its high step coverage, significantly low thermal budget, and scalability.

In this chapter, we describe the growth and characterization of a quasi-2-DEG system with electron Hall mobility as large as 3,000 cm<sup>2</sup>V<sup>-1</sup>s<sup>-1</sup> and sheet carrier density as high as 5×10<sup>12</sup> cm<sup>-2</sup> at 15 K in epitaxial  $\gamma$ -Al<sub>2</sub>O<sub>3</sub>/STO heterointerfaces. Al<sub>2</sub>O<sub>3</sub> films were grown on TiO<sub>2</sub>-terminated STO substrates by ALD at a temperature range of 200–345 °C using TMA and H<sub>2</sub>O. We show that Al<sub>2</sub>O<sub>3</sub> grown above 300 °C is crystalline and epitaxial. The formation of the 2-DEG can be explained by oxygen vacancy generation in the surface region of the STO substrate<sup>20–22</sup> during the initial stages of growth. The formation of smooth Al<sub>2</sub>O<sub>3</sub> films with a high degree of crystallinity on STO allows for further epitaxial integration on top of the Al<sub>2</sub>O<sub>3</sub> layer, which is promising for realization of more complex device architectures.

## 5.2. EXPERIMENTAL

*Sample Growth.* TiO<sub>2</sub>-terminated STO(001) substrates of dimension 5 mm × 5 mm × 0.5 mm from CrysTec were ultrasonically cleaned with acetone, isopropyl alcohol, and deionized water for 5 min each, followed by a UV/ozone exposure for 15 min to remove residual carbon contamination. The substrates were loaded into the system and vacuum-annealed at 650 °C and pressures lower than 1×10<sup>-8</sup> Torr for 30 min to outgas. STO substrates were then transferred *in situ* to the ALD chamber for Al<sub>2</sub>O<sub>3</sub> deposition. The ALD reactor consists of a custom built, hot-wall stainless steel rectangular chamber with 20 cm long and 460 cm<sup>3</sup> volume. Ultra-high purity Ar was used as the purge/carrier

gas with a cross-flow along the reactor. The operating pressure was maintained at  $\sim 1$  Torr. TMA and water were used as co-reactants for  $\text{Al}_2\text{O}_3$  growth. The  $\text{Al}_2\text{O}_3$  films were grown at temperatures ranging from 200–345 °C. An ALD cycle for  $\text{Al}_2\text{O}_3$  consists of 1 s of TMA dosing, a 15 s purge, followed by 1 s of  $\text{H}_2\text{O}$  dosing and another 15 s purge.

*Characterization of  $\text{Al}_2\text{O}_3$  Films.* The as-deposited  $\text{Al}_2\text{O}_3$  films were transferred *in situ* to the MBE chamber, where reflection high energy electron diffraction (RHEED) is used to characterize crystallinity and surface morphology. A VG Scienta R3000 XPS system is used to determine the valence state of Ti and to characterize the  $\text{Al}_2\text{O}_3/\text{STO}$  interface. XPS was performed *in situ* with a monochromatic Al  $K\alpha$  source with a photon energy of 1486.6 eV. Thicknesses and growth rates of  $\text{Al}_2\text{O}_3$  films were determined by x-ray reflectivity (XRR). X-ray diffraction (XRD) and transmission electron microscopy (TEM) are used to determine the crystallinity of the  $\text{Al}_2\text{O}_3$  films. XRR analysis was conducted using a Panalytical X'PERT Pro diffractometer with a sealed tube Cu  $K\alpha$  radiation source ( $\lambda \sim 1.5406 \text{ \AA}$ ), operating at 40 kV and 30 mA. XRD characterization was carried out at the National Synchrotron Light Source beam line X20A using a triple access configuration in non-dispersive geometry with a Ge(111) double-crystal monochromator and analyzer set to  $l = 1.5405 \text{ \AA}$ . TEM analysis employed a JEOL JEM-4000EX transmission electron microscope equipped with a double-tilt specimen holder, operating at 400 keV. The samples were prepared using standard mechanical polishing followed by argon-ion-milling to perforation.

*Electrical Measurement.* In order to electrically contact the alumina/STO interface, four indium contacts were placed on scribed corners of each sample in a van der Pauw geometry. Measurements were taken using a Quantum Design Physical Property Measurement System capable of applying a  $\pm 9$  T magnetic field and 1.9–350 K temperature range. Two Stanford SR830 lock-in amplifiers and one SR570 current

preamplifier were used to perform 4-wire electrical transport measurement using less than 1  $\mu\text{A}$  current at a frequency of 7 or 13 Hz.

### 5.3. RESULTS AND DISCUSSION

Figures 5.1a and 5.1b show RHEED patterns of a  $\text{TiO}_2$ -terminated STO substrate and a 27-nm-thick  $\text{Al}_2\text{O}_3$  film grown by ALD at 345 °C. RHEED patterns were taken along the  $\langle 110 \rangle$  azimuth of the STO substrate before and after the  $\text{Al}_2\text{O}_3$  deposition. Streaky patterns along with clear Kikuchi lines highlight the high degree of crystalline order and low surface roughness of the  $\text{Al}_2\text{O}_3$  layers. Streaky RHEED patterns were also maintained during the growth of thick  $\text{Al}_2\text{O}_3$  films, indicating good crystalline quality throughout the  $\text{Al}_2\text{O}_3$  layers. RHEED patterns also indicated that  $\text{Al}_2\text{O}_3$  films grown on  $\text{TiO}_2$ -terminated STO at 200 °C were amorphous and that  $\text{Al}_2\text{O}_3$  films grown at 300 °C were crystalline (not shown). The growth rate of  $\text{Al}_2\text{O}_3$  on STO was found to be 0.85  $\text{\AA}/\text{cycle}$  at 345 °C becoming higher at lower growth temperature (about 1  $\text{\AA}$ –1.1  $\text{\AA}/\text{cycle}$ ), which is consistent with previous reports.<sup>23</sup> Figure 5.1c shows the x-ray diffraction patterns of an 18-nm-thick  $\text{Al}_2\text{O}_3$  film on  $\text{TiO}_2$ -terminated STO, grown at 345 °C. Besides the  $(00l)$  Bragg peaks of STO, only the  $(00l)$   $\gamma\text{-Al}_2\text{O}_3$  Bragg peaks are observed in the 18-nm-thick  $\text{Al}_2\text{O}_3$  sample, with no detectable presence of impurity phases or other orientations. The  $(004)$   $\gamma\text{-Al}_2\text{O}_3$  peak appears at a reciprocal lattice spacing of  $q_l = 3.142 \text{ \AA}^{-1}$  and corresponds to an out-of-plane lattice constant for the film of 7.999  $\text{\AA}$ . This is larger than the bulk out-of-plane lattice constant of  $\gamma\text{-Al}_2\text{O}_3$ ,<sup>24</sup> but consistent with the  $\gamma\text{-Al}_2\text{O}_3$  layer being strained to the underlying STO, which has a lattice parameter of  $a = 3.905 \text{ \AA}$ . Detail film strain analysis is not possible due to weak scattering of alumina and its close proximity to strong STO peaks. An in-plane scan along the  $(h00)$  direction

(Figure 5.2) indicates a strained (400)  $\gamma$ -Al<sub>2</sub>O<sub>3</sub> peak that is roughly coincident with the (200) STO substrate peak. Figure 5.1c also shows finite size oscillations around the (002) STO and (004)  $\gamma$ -Al<sub>2</sub>O<sub>3</sub> reflection indicating a very smooth Al<sub>2</sub>O<sub>3</sub> film surface and a sharp  $\gamma$ -Al<sub>2</sub>O<sub>3</sub>/STO interface. The omega scan at  $q_l = 3.142 \text{ \AA}^{-1}$  (not shown) shows a full-width at half-maximum of  $\sim 0.3^\circ$  confirming the high degree of crystallinity of the  $\gamma$ -Al<sub>2</sub>O<sub>3</sub> film.

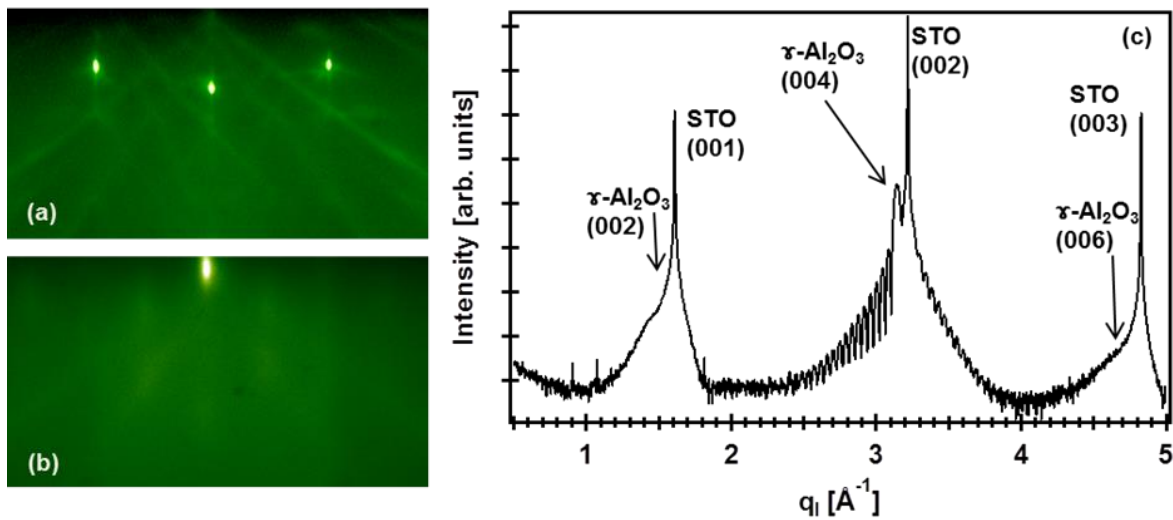


Figure 5.1. RHEED patterns of: (a) TiO<sub>2</sub>-terminated STO substrate and (b) 27-nm-thick Al<sub>2</sub>O<sub>3</sub> grown by ALD on TiO<sub>2</sub>-terminated STO at 345 °C. RHEED patterns were taken along the  $\langle 110 \rangle$  azimuth of the STO substrate; (c) XRD pattern of an 18-nm-thick Al<sub>2</sub>O<sub>3</sub> film on TiO<sub>2</sub>-terminated STO grown by ALD at 345 °C.

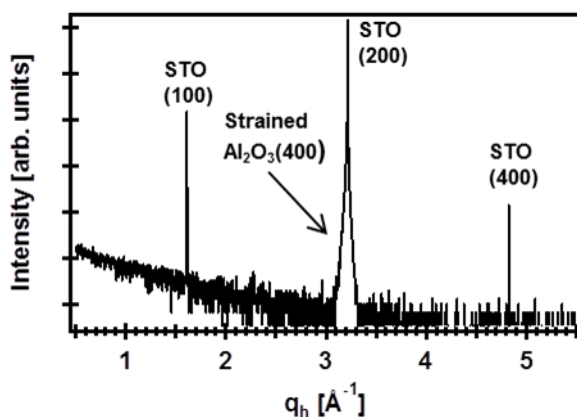


Figure 5.2. In-plane grazing incident-XRD scan of 18-nm-thick ALD-grown Al<sub>2</sub>O<sub>3</sub> film on TiO<sub>2</sub>-terminated STO at 345 °C along (*h*00) direction. The strained Al<sub>2</sub>O<sub>3</sub>(400) peak is roughly coincident with STO(200) substrate peak indicating the in-plane lattice constant of  $\gamma$ -Al<sub>2</sub>O<sub>3</sub> is very close to the STO substrate (3.905 Å).

Figure 5.3a shows a cross-sectional TEM image of a 2.1-nm-thick Al<sub>2</sub>O<sub>3</sub> film grown at 345 °C by ALD on a TiO<sub>2</sub>-terminated STO substrate, again confirming the crystallinity of the Al<sub>2</sub>O<sub>3</sub> film. The surface of the Al<sub>2</sub>O<sub>3</sub> film is very smooth, consistent with RHEED and XRD. Figure 5.3a also shows an abrupt interface between the Al<sub>2</sub>O<sub>3</sub> film and the STO substrate. The Al<sub>2</sub>O<sub>3</sub> films grown at 300 °C also display a similar high degree of crystallinity (Figure 5.3b). Figure 5.3c presents an electron micrograph in the <110> projection of STO for a 27-nm-thick Al<sub>2</sub>O<sub>3</sub> film grown at 345 °C, confirming that the Al<sub>2</sub>O<sub>3</sub> film still maintains a smooth surface as the thickness increases. The corresponding selected area electron diffraction pattern in Figure 5.3d shows strong spots originating from the STO substrate while the weaker spots (arrowed) come from the Al<sub>2</sub>O<sub>3</sub> film.

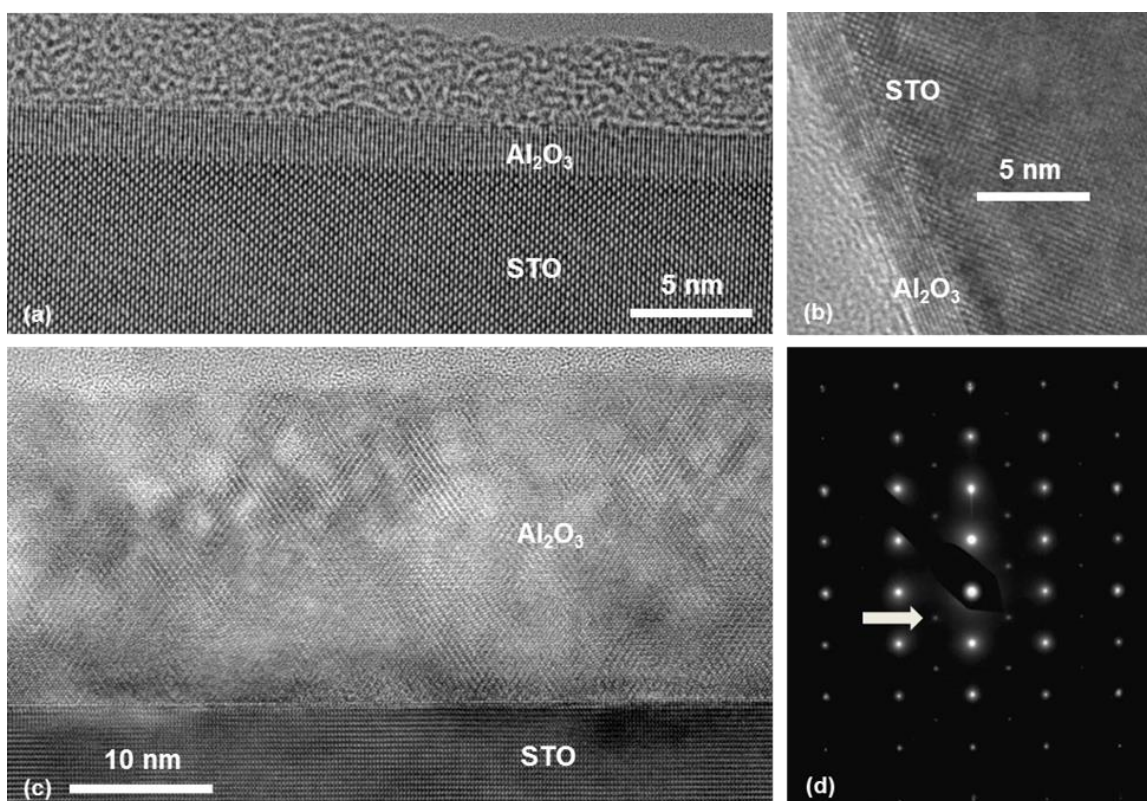


Figure 5.3. (a) TEM image showing 2.1-nm-thick  $\text{Al}_2\text{O}_3$  on  $\text{TiO}_2$ -terminated by ALD at 345 °C, (b) TEM image of 2.5-nm-thick  $\text{Al}_2\text{O}_3$  on  $\text{TiO}_2$ -terminated by ALD at 300 °C, (c) TEM image in  $\langle 110 \rangle$  projection of 27-nm-thick  $\text{Al}_2\text{O}_3$  on  $\text{TiO}_2$ -terminated by ALD at 345 °C, and (d) selected-area electron diffraction pattern of 27-nm-thick  $\text{Al}_2\text{O}_3$  on  $\text{TiO}_2$ -terminated by ALD at 345 °C in the  $\langle 110 \rangle$  projection, weak spots (arrowed) originate from  $\text{Al}_2\text{O}_3$ .

To determine the origin of interfacial conductivity of the  $\gamma\text{-Al}_2\text{O}_3/\text{STO}$  heterostructure, *in situ* XPS measurements were performed during our study. The Ti 2*p* core level XP spectra indirectly provide information about the oxygen vacancy concentration near the heterointerface on the STO side. The more Ti 2*p* that appears in reduced forms ( $\text{Ti}^{3+}$ ,  $\text{Ti}^{2+}$ ), the more oxygen vacancies that must have been formed in the STO. Figure 5.4a shows normalized Ti 2*p* core-level XP spectra after 25 cycles of  $\text{Al}_2\text{O}_3$  on  $\text{TiO}_2$ -terminated STO single crystal substrates at different temperatures (from 200–345 °C). No  $\text{Ti}^{3+}$  features in the Ti 2*p* spectrum are detected for the bare  $\text{TiO}_2$ -terminated

STO substrates even after a 30-min ultrahigh vacuum anneal at 650 °C, as well as after the growth of 25 ALD cycles of Al<sub>2</sub>O<sub>3</sub> at 200 and 300 °C, thus indicating negligible Ti<sup>3+</sup> formation for these case. These results differ from the report that Ti<sup>3+</sup> species were observed at the amorphous Al<sub>2</sub>O<sub>3</sub>/STO interface grown by ALD at 300 °C.<sup>15,25</sup>

The occurrence of a Ti<sup>3+</sup> feature at a binding energy of ~ 457 eV in the Al<sub>2</sub>O<sub>3</sub>/STO heterostructure is clear for the Al<sub>2</sub>O<sub>3</sub> samples grown at 325 °C (purple curve) and 345 °C (red curve). Moreover, the amount of Ti<sup>3+</sup> increases with increasing deposition temperature. The 325 °C ALD-grown Al<sub>2</sub>O<sub>3</sub> shows 6.7 % Ti<sup>3+</sup> and the 345 °C ALD-grown Al<sub>2</sub>O<sub>3</sub> film yields 11.0 % Ti<sup>3+</sup>. This result suggests a possible means to control the amount of oxygen vacancies by simply modifying the ALD deposition temperature, thus leading to the possibility of controlling the conductivity of the heterointerface.

Angle-resolved XPS was performed with varying photoelectron takeoff angle for a 0.5-nm-thick Al<sub>2</sub>O<sub>3</sub> film grown by ALD on TiO<sub>2</sub>-terminated STO at 345 °C (Figure 5.4b). The ratio Ti<sup>3+</sup>/Ti<sup>4+</sup> increases as the takeoff angle decreases from normal emission, indicating that the electrons generated by oxygen vacancies are localized near the STO surface region. Figures 5.4c and 5.4d show normalized Ti 2*p* XP spectra for different numbers of ALD cycles grown on a TiO<sub>2</sub>-terminated STO substrate at 345 °C. After one ALD cycle, there is a negligible Ti<sup>3+</sup> feature, but the Ti<sup>3+</sup> feature becomes more visible after 2 to 3 ALD cycles (Figure 5.4c). After 5 cycles of ALD, we observe a significant amount of Ti<sup>3+</sup> at the Al<sub>2</sub>O<sub>3</sub>/STO interface (4.5%). After 10–20 ALD cycles of Al<sub>2</sub>O<sub>3</sub>, the amount of Ti<sup>3+</sup> remains constant (~ 11%).

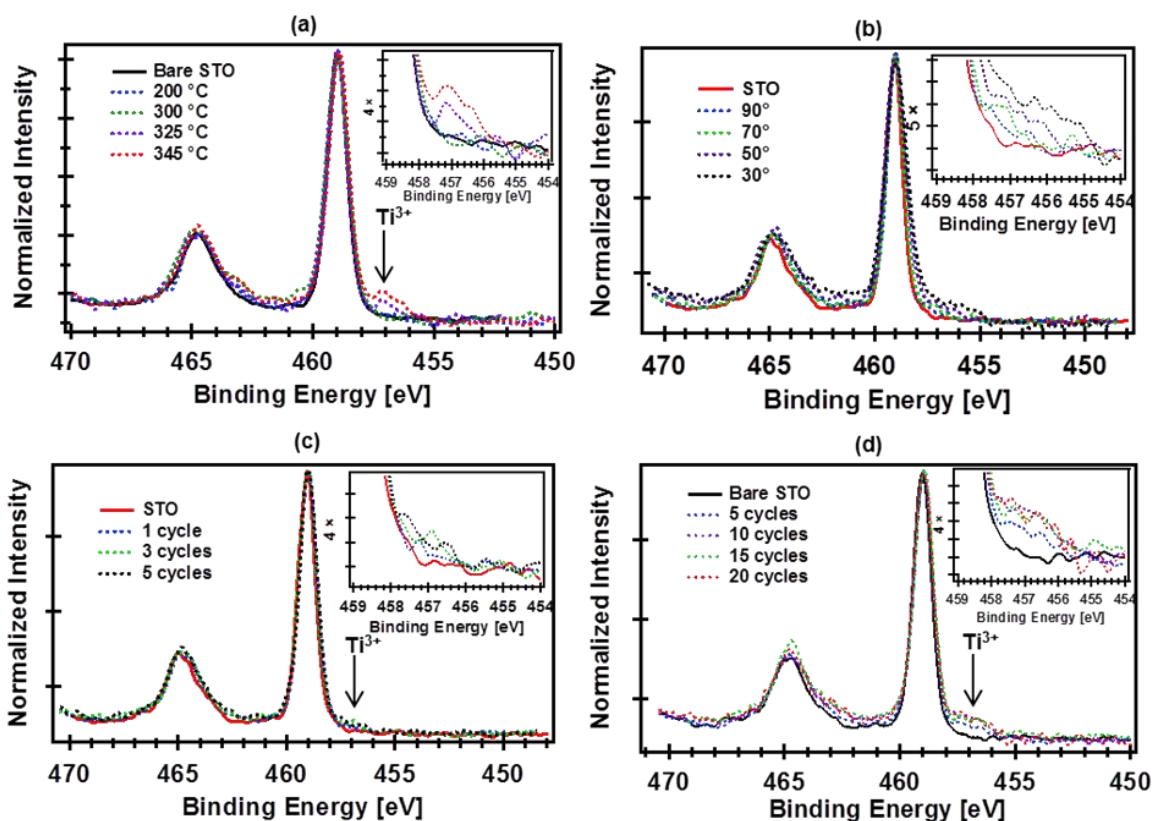


Figure 5.4. (a) Ti  $2p$  XPS spectra of 25 cycles of  $\text{Al}_2\text{O}_3$  grown on  $\text{TiO}_2$ -terminated STO by ALD at different temperatures. (b) Angle-resolved XPS of 0.5-nm-thick  $\text{Al}_2\text{O}_3$  film grown by ALD on  $\text{TiO}_2$ -terminated STO at 345 °C at 30, 50, 70, and 90 ° takeoff angles. (c) and (d) Ti  $2p$  XPS spectra of  $\text{Al}_2\text{O}_3$  layers grown on  $\text{TiO}_2$ -terminated STO by ALD at 345 °C with different numbers of ALD cycles.

To better understand the formation of oxygen vacancies, exposure of  $\text{TiO}_2$ -terminated STO substrates to TMA were carried out at 300 and 345 °C. Figure 5.5 presents Ti  $2p$ , and Figure 5 presents Al  $2p$  and O  $1s$  XPS spectra of STO substrate after exposing it to TMA. Exposure of a  $\text{TiO}_2$ -terminated STO substrate to TMA alone for 5 s at 345 °C leads to an 8.9%  $\text{Ti}^{3+}$  feature at  $\sim 457$  eV (Figure 5.5a). The appearance of an Al  $2p$  XPS feature at a binding energy of 75.5 eV (Figure 5.6a) and a small shoulder for the O  $1s$  XPS spectrum at a binding energy of 532.5 eV (Figure 5.6b) indicate

that formation of  $\text{Al}_2\text{O}_3$  occurred due to the reaction between TMA and STO, even without  $\text{H}_2\text{O}$  dosing. The longer the exposure time to TMA without  $\text{H}_2\text{O}$  dosing, then the more STO reacts with TMA to form even more  $\text{Ti}^{3+}$ . Figure 5.5b shows Ti 2*p* XP spectra of a STO substrate after exposure to TMA for 5 min. An even more-reduced  $\text{Ti}^{2+}$  feature appears at a binding energy of  $\sim 456$  eV, accompanied by an increase of  $\text{Ti}^{3+}$ . The increase of Al 2*p* and O 1*s* signals for  $\text{Al}_2\text{O}_3$  (Figure 5.6) are clear demonstrations of the reaction between TMA and STO. Figures 5.5c and 5.5d show Ti 2*p* XP spectra for a STO substrate after exposure to TMA at 300 °C for 5 s and 5 min, respectively, indicating that exposures of STO substrates to TMA at 300 °C could also lead to the formation of  $\text{Ti}^{3+}$  features (6.7 %  $\text{Ti}^{3+}$  for 5 s and 7.7 %  $\text{Ti}^{3+}$  for 5 min exposures). This demonstrates the reduction of STO by TMA has occurred at 300 °C, and differs from the previous study that the repetitive pulse of TMA did not induce the reduction of STO substrate at the same temperature.<sup>15</sup> It should be noted that this does not contradict the result above that the reduction of STO was not observed during the ALD growth of  $\text{Al}_2\text{O}_3$  at 300 °C. During the growth of  $\text{Al}_2\text{O}_3$  at 300 °C,  $\text{H}_2\text{O}$  is introduced into every ALD cycle and  $\text{H}_2\text{O}$  can fully re-oxidize the STO substrate (at 300 °C), whereas the re-oxidation of STO might happen incompletely at higher temperature (*e.g.*, 345 °C).

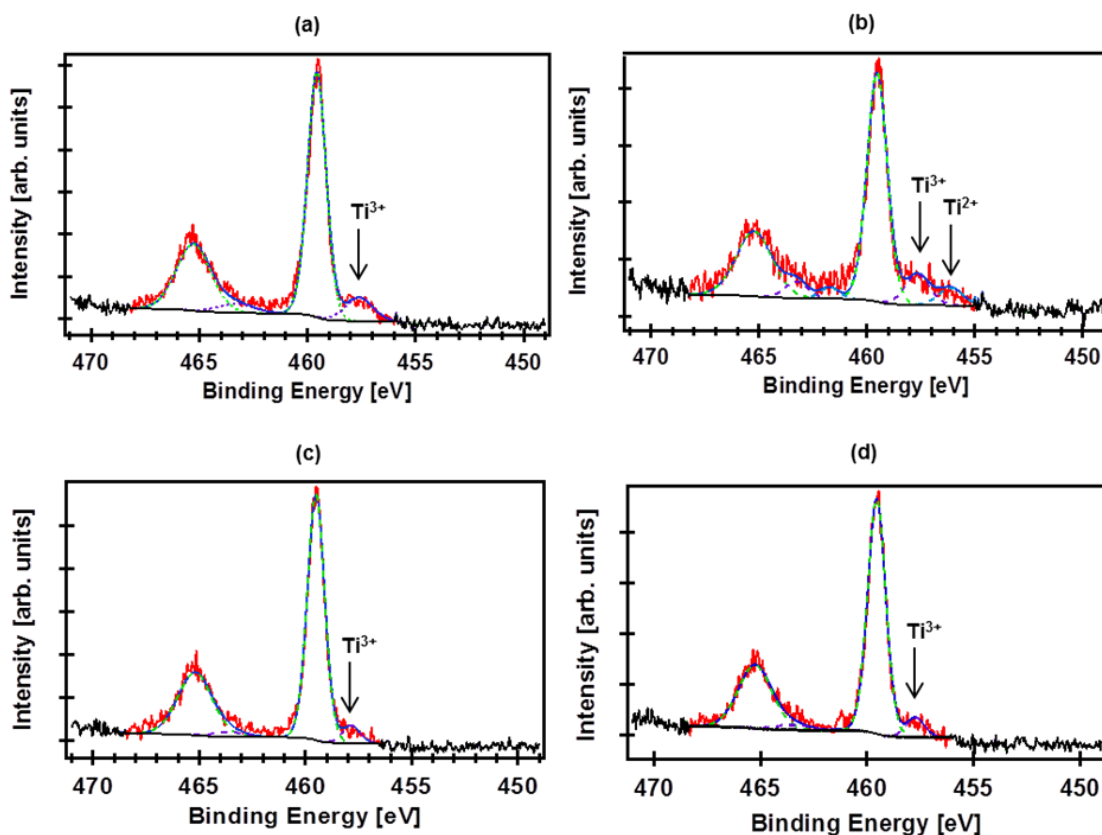


Figure 5.5. Ti  $2p$  XP spectra of  $\text{TiO}_2$ -terminated STO substrates after: (a) 5-s exposure to TMA at  $345\text{ }^\circ\text{C}$ , (b) 5-min exposure to TMA at  $345\text{ }^\circ\text{C}$ , (c) 5-s exposure to TMA at  $300\text{ }^\circ\text{C}$ , and (d) 5-min exposure to TMA at  $300\text{ }^\circ\text{C}$ .

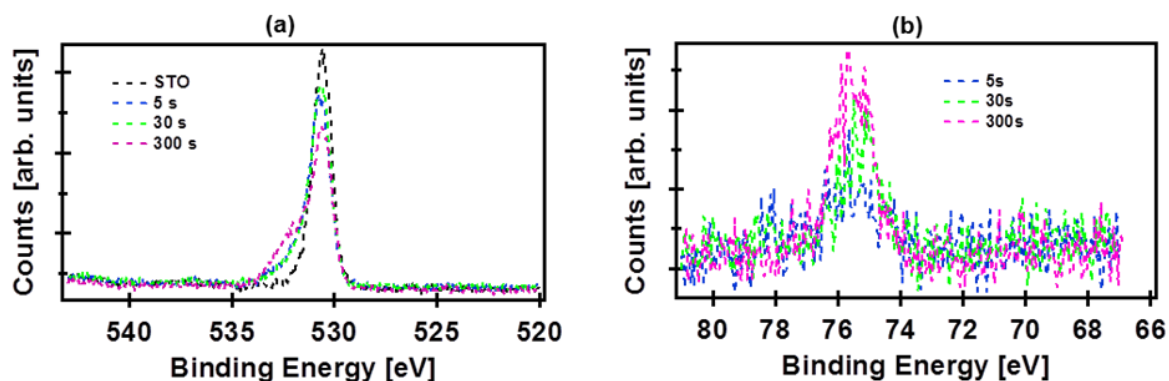


Figure 5.6. (a) Al  $2p$  and (b) O  $1s$  XP spectra of a  $\text{TiO}_2$ -terminated STO substrate after exposure to TMA alone at  $345\text{ }^\circ\text{C}$  for different times. These spectral features are a good indication of a reaction between TMA and  $\text{H}_2\text{O}$  to form  $\text{Ti}^{3+}$  and even  $\text{Ti}^{2+}$  and  $\text{Al}_2\text{O}_3$ .

TiO<sub>2</sub>-terminated STO substrates after a 30 min vacuum anneal at 650 °C are still very insulating (sheet resistance on the order of GΩ at room temperature). The interface of Al<sub>2</sub>O<sub>3</sub> films grown at temperatures lower than 300 °C are also insulating with sheet resistance that varies from MΩ to GΩ at room temperature. Figure 5.7 shows the temperature-dependent electronic properties of the Al<sub>2</sub>O<sub>3</sub>/STO interface with different film thicknesses. At an Al<sub>2</sub>O<sub>3</sub> thickness of ~ 2.1 nm (25 ALD cycles), the room temperature sheet resistance was found to be ~ 30 kΩ/sq, which is 3–5 times lower than what has been reported for amorphous LAO/STO and amorphous Al<sub>2</sub>O<sub>3</sub>/STO systems.<sup>15</sup> As shown in Figure 5.7a, while the 2.1-nm-thick Al<sub>2</sub>O<sub>3</sub>/STO heterointerface shows metallic behavior down to low temperatures, heterointerfaces with 4.3-nm-thick (50 ALD cycles) and 8.5-nm-thick (100 ALD cycles) Al<sub>2</sub>O<sub>3</sub> films have an increase of sheet resistance below 100 K. Sheet resistance generally increases with increasing film thicknesses for the film thickness above 2.1 nm (Figure 5.7a). The increase of sheet resistance with film thicknesses is correlated with the decrease in oxygen vacancies as the film thickness increases, possibly because exposure of the heterolayer to more water during ALD growth of the thicker films limits vacancy formation. Ti 2*p* spectra show that ~ 11 % of Ti<sup>3+</sup> feature is present in the 10–25 ALD cycle-Al<sub>2</sub>O<sub>3</sub> films, ~ 8.5 % of Ti<sup>3+</sup> is present in a 35 ALD cycle-Al<sub>2</sub>O<sub>3</sub> film (3.0-nm-thick), and ~ 6 % of Ti<sup>3+</sup> is present in a 50 ALD cycle-Al<sub>2</sub>O<sub>3</sub> film. The 15 cycle Al<sub>2</sub>O<sub>3</sub> sample (~ 1.3 nm) shows higher sheet resistance compared to the 25 cycle Al<sub>2</sub>O<sub>3</sub> sample (~ 2.1 nm).

The increase of sheet resistance for the 1.3-nm-thick film is possibly due to the Al<sub>2</sub>O<sub>3</sub> layer not being thick enough to protect the Al<sub>2</sub>O<sub>3</sub>/STO interface from re-oxidation when the sample is exposed to air. Oxygen can slowly diffuse through the Al<sub>2</sub>O<sub>3</sub> layer if it is thin enough and react with oxygen vacancies at the Al<sub>2</sub>O<sub>3</sub>/STO interface. To verify this hypothesis, a 1.3-nm-thick Al<sub>2</sub>O<sub>3</sub> was grown on TiO<sub>2</sub>-terminated STO by ALD at

345 °C. Ti 2*p* XP spectra reveal ~ 11 % of Ti<sup>3+</sup> at the interface. The sample was taken out of the vacuum chamber and exposed to ambient air at room temperature for 5 days and was then re-loaded into the system. Ti 2*p* XP spectrum (not shown) displays ~ 4 % of Ti<sup>3+</sup> at the interface after air exposure. The same experiment was also performed with a 2.1-nm-thick Al<sub>2</sub>O<sub>3</sub>/STO sample. Ti 2*p* XP spectrum indicates that Ti<sup>3+</sup> feature remains unchanged after exposing to air ambient for 5 days. This demonstrates that the increase of sheet resistance for the 1.3-nm-thick Al<sub>2</sub>O<sub>3</sub>/STO sample is likely due to the reaction between oxygen vacancies and oxygen in air diffusing through the very thin Al<sub>2</sub>O<sub>3</sub> layer.

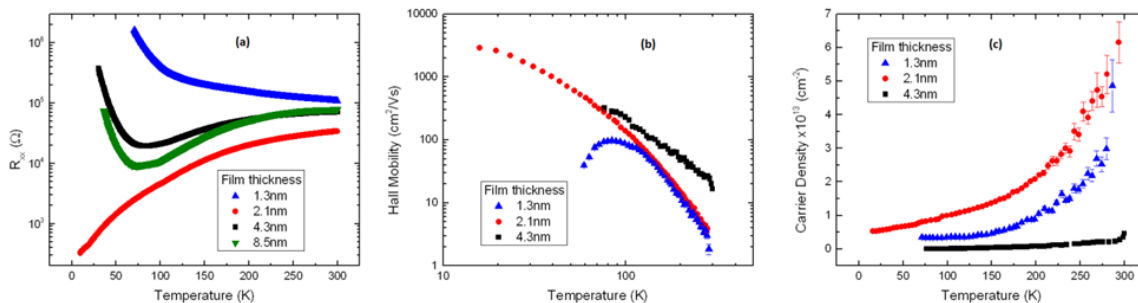


Figure 5.7. Thickness and deposition temperature dependent electronic properties of the  $\gamma$ -Al<sub>2</sub>O<sub>3</sub>/STO interface. (a) Thickness and deposition temperature dependence of sheet resistance,  $R_{xx}$  for the  $\gamma$ -Al<sub>2</sub>O<sub>3</sub>/STO interface conduction at Al<sub>2</sub>O<sub>3</sub> film thicknesses of 1.3 nm, 2.1 nm, 4.3 nm, and 8.5 nm deposited at 345 °C. (b) Hall mobility,  $\mu_{Hall}$ , and (c) sheet carrier density,  $n_s$ , for the  $\gamma$ -Al<sub>2</sub>O<sub>3</sub>/STO interface conduction at Al<sub>2</sub>O<sub>3</sub> film thicknesses of 1.3 nm, 2.1 nm, and 4.3 nm deposited at 345 °C.

A 2.1-nm-thick Al<sub>2</sub>O<sub>3</sub>/STO sample was annealed in air at 500 °C for 60 min and became very insulating. The sample was re-loaded into the system after annealing for XPS analysis and displayed no Ti<sup>3+</sup> feature (not shown), which indicates that oxygen vacancies at the Al<sub>2</sub>O<sub>3</sub>/STO interface are the major source of carriers. Similarly, all  $\gamma$ -Al<sub>2</sub>O<sub>3</sub>/STO samples became very insulating after annealing in air at 500 °C for 60 min. The temperature dependence of the Hall mobility and carrier density for different film

thicknesses are shown in Figures 5.7b and 5.7c. The mobility at room temperature for a 2.1-nm-thick  $\text{Al}_2\text{O}_3/\text{STO}$  is  $30 \text{ cm}^2\text{V}^{-1}\text{s}^{-1}$  with a carrier density of  $\sim 6 \times 10^{13} \text{ cm}^{-2}$ , while mobility and carrier density at 15 K are  $\sim 3,000 \text{ cm}^2\text{V}^{-1}\text{s}^{-1}$  and  $5 \times 10^{12} \text{ cm}^{-2}$ , respectively. The observed mobility of the  $\gamma\text{-Al}_2\text{O}_3/\text{STO}$  interfaces are similar to the mobility reported for the  $\gamma\text{-Al}_2\text{O}_3/\text{STO}$  heterostructure grown by PLD.<sup>17,19</sup> Systematic variations of mobility and carrier density with  $\text{Al}_2\text{O}_3$  thicknesses are also observed in our study.

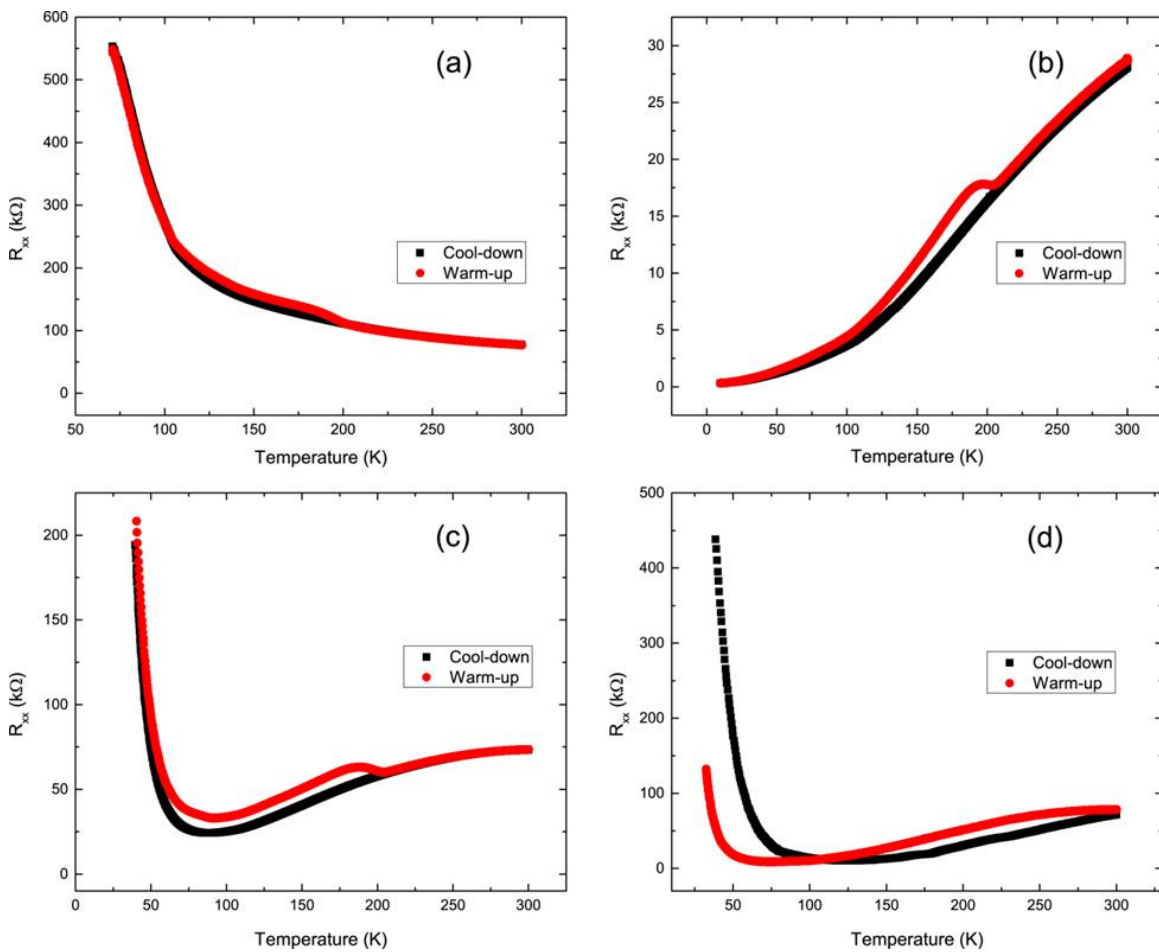


Figure 5.8. Temperature dependent sheet resistance of: (a) 15 cycles  $\sim 1.3$  nm, (b) 25 cycles  $\sim 2.1$  nm, (c) 50 cycles  $\sim 4.3$  nm, and (d) 100 cycles  $\sim 8.5$  nm  $\text{Al}_2\text{O}_3$  on  $\text{TiO}_2$ -terminated STO by ALD at  $345^\circ\text{C}$  during warm up (red curves) and cool down (black curves) processes.

Figures 5.8a–d show sheet resistance vs. temperature for samples with different  $\text{Al}_2\text{O}_3$  thicknesses, varying from 1.3 to 8.5 nm. The measurements were taken during both cool down (black curves) and warm up (red curves). Hysteresis of the sheet resistance with temperature is also observed in the heterostructure with higher sheet resistance exhibited during the warm up process for different thicknesses of  $\text{Al}_2\text{O}_3$ . This is suggestive of the occurrence of a structural phase transition in the  $\gamma\text{-Al}_2\text{O}_3/\text{STO}$  heterointerface.<sup>26</sup> We are performing further studies to address this phenomenon.

#### 5.4. SUMMARY

We demonstrate a chemical route to the formation of highly crystalline  $\gamma\text{-Al}_2\text{O}_3$  on STO using ALD. We also showed that a high mobility quasi-2-DEG forms at the crystalline  $\gamma\text{-Al}_2\text{O}_3/\text{STO}$  heterointerface. The sheet resistance of the interface for samples grown at temperatures lower than 300 °C is high ( $>M\Omega$ ), whereas the sheet resistance of samples grown at a temperature of 345 °C is much lower and comparable to what has been reported elsewhere for similar systems. The control of sheet resistance can be achieved by modifying the deposition temperature. A mobility of  $3,000\text{ cm}^2\text{V}^{-1}\text{s}^{-1}$  was measured for the 2.1-nm-thick  $\text{Al}_2\text{O}_3/\text{STO}$  heterointerface at 15 K. High mobility quasi-2-DEG formation at the  $\text{Al}_2\text{O}_3/\text{STO}$  interface and the ideal ALD behavior of  $\text{Al}_2\text{O}_3$  film growth are promising factors that could lead to the use of crystalline  $\text{Al}_2\text{O}_3$  in all-oxide device applications.

#### 5.5. REFERENCES

- <sup>1</sup>J. H. Ngai, F. J. Walker, and C. H. Ahn, *Annu. Rev. Mater. Res.* **44**, 1 (2014).
- <sup>2</sup>E. Fortunato, P. Barquinha, and R. Martins, *Adv. Mater.* **24**, 2945 (2012).

- <sup>3</sup>D. T. Gillaspie, R. C. Tenent, and A. C. Dillon, *J. Mater. Chem.* **20**, 9585 (2010).
- <sup>4</sup>P. Zubko, S. Gariglio, M. Gabay, P. Ghosez, and J.-M. Triscone, *Annu. Rev. Condens. Matter Phys.* **2**, 141 (2011).
- <sup>5</sup>H. Y. Hwang, Y. Iwasa, M. Kawasaki, B. Keimer, N. Nagaosa, and Y. Tokura, *Nat. Mater.* **11**, 103 (2012).
- <sup>6</sup>A. Ohtomo and H. Y. Hwang, *Nature* **427**, 423 (2004).
- <sup>7</sup>A. McCollam, S. Wenderich, M. K. Kruize, V. K. Guduru, H. J. A. Molegraaf, M. Huijben, G. Koster, D. H. A. Blank, G. Rijnders, A. Brinkman, H. Hilgenkamp, U. Zeitler, and J. C. Maan, *Appl. Phys. Lett.* **2**, 022102 (2014).
- <sup>8</sup>N. Reyren, M. Bibes, E. Lesne, J.-M. George, C. Deranlot, S. Collin, A. Barthélémy, and H. Jaffrès, *Phys. Rev. Lett.* **108**, 186802 (2012).
- <sup>9</sup>J. Mannhart and D. G. Schlom, *Science* **327**, 1607 (2010).
- <sup>10</sup>J. Lee and A. A. Demkov, *Phys. Rev. B* **78**, 193104 (2008).
- <sup>11</sup>N. Nakagawa, H. Y. Hwang, and D. A. Muller, *Nat. Mater.* **5**, 204 (2006).
- <sup>12</sup>S. A. Chambers, *Adv. Mater.* **22**, 219 (2010).
- <sup>13</sup>W. Siemons, G. Koster, H. Yamamoto, W. A. Harrison, G. Lucovsky, T. H. Geballe, D. H. A. Blank, and M. R. Beasley, *Phys. Rev. Lett.* **98**, 196802 (2007).
- <sup>14</sup>Y. Chen, N. Pryds, J. E. Kleibeuker, G. Koster, J. Sun, E. Stamate, B. Shen, G. Rijnders, and S. Linderoth, *Nano Lett.* **11**, 3774 (2011).
- <sup>15</sup>S. W. Lee, Y. Liu, J. Heo, and R. G. Gordon, *Nano Lett.* **12**, 4775 (2012).
- <sup>16</sup>Z. Q. Liu, C. J. Li, W. M. Lü, X. H. Huang, Z. Huang, S. W. Zeng, X. P. Qiu, L. S. Huang, A. Annadi, J. S. Chen, J. M. D. Coey, T. Venkatesan, and Ariando, *Phys. Rev. X* **3**, 021010 (2013).
- <sup>17</sup>Y. Z. Chen, N. Bovet, F. Trier, D. V. Christensen, F. M. Qu, N. H. Andersen, T. Kasama, W. Zhang, R. Giraud, J. Dufouleur, T. S. Jespersen, J. R. Sun, A. Smith, J.

Nygård, L. Lu, B. Büchner, B. G. Shen, S. Linderoth, and N. Pryds, *Nat. Commun.* **4**, 1371 (2012).

<sup>18</sup>K. J. Kormondy, A. B. Posadas, T. Q. Ngo, S. Lu, N. Goble, J. Jordan-Sweet, X. P. A. Gao, D. J. Smith, M. R. McCartney, J. G. Ekerdt, and A. A. Demkov, *J. Appl. Phys.* **117**, 095303 (2015).

<sup>19</sup>Y. Z. Chen, N. Bovet, T. Kasama, W. W. Gao, S. Yazdi, C. Ma, N. Pryds, and S. Linderoth, *Adv. Mater.* **26**, 1462 (2013).

<sup>20</sup>C. Lin, C. Mitra, and A. A. Demkov, *Phys. Rev. B* **86**, 161102(R) (2012).

<sup>21</sup>C. Mitra, C. Lin, J. Robertson, and A. A. Demkov, *Phys. Rev. B* **86**, 155105 (2012).

<sup>22</sup>C. Lin and A. A. Demkov, *Phys. Rev. Lett.* **111**, 217601 (2013).

<sup>23</sup>S. M. George, *Chem. Rev.* **110**, 111 (2009).

<sup>24</sup>R.-S. Zhou and R. L. Snyder, *Acta Cryst. B* **47**, 617 (1991).

<sup>25</sup>S. W. Lee, J. Heo, and R. G. Gordon, *Nanoscale* **5**, 8940 (2013).

<sup>26</sup>F. Schoofs, M. Egilmez, T. Fix, J. L. MacManus-Driscoll, and M. G. Blamire, *Appl. Phys. Lett.* **100**, 081601 (2012).

## **Chapter 6: Atomic Layer Deposition of Photoactive CoO/SrTiO<sub>3</sub> and CoO/TiO<sub>2</sub> on Si(001) for Visible Light Driven Photoelectrochemical Water Oxidation**

### **6.1. INTRODUCTION**

Global climate change has prompted research into new technologies to produce clean and renewable energy. Hydrogen is a very attractive fuel due to its zero carbon emissions, high conversion efficiencies, and recyclability.<sup>1-4</sup> Hydrogen can be derived from various reactions of water or organic compounds such as hydrocarbons. At present, the majority of hydrogen is produced from natural gas by steam reforming,<sup>5,6</sup> which generates CO<sub>2</sub> that is typically released to the environment. Therefore, alternative methods for forming hydrogen from renewable, sustainable, and non-petroleum resources such as water need to be developed to achieve the benefits of a hydrogen economy while lowering greenhouse gas impact. Since the first study on water splitting using TiO<sub>2</sub> as a photoanode was reported,<sup>7</sup> photoelectrochemical (PEC) water splitting to generate hydrogen using semiconductor materials has been the subject of extensive research.<sup>3,8-12</sup> In PEC water splitting, light is absorbed in a semiconducting catalytic material, electrons are promoted to the conduction band, leaving holes in the valence band. Electrons and holes are then transported to the photocatalyst/water interface, to reduce and oxidize water, forming hydrogen and oxygen, respectively. In order to achieve the spontaneous water splitting reaction, the conduction band minimum and the valence band maximum of semiconductor materials must be more negative than the hydrogen evolution potential and more positive than the oxygen evolution potential, respectively. Titanates such as TiO<sub>2</sub> and SrTiO<sub>3</sub> (STO) have become well-known photocatalytic materials in solar energy

conversion because of their appropriate band edge positions, nontoxicity, water insolubility, chemical stability and photocatalytic activity under UV-illumination.<sup>3,8,13-18</sup>

However, the large band gap of TiO<sub>2</sub> (3.2 eV for anatase and brookite, 3.0 eV for rutile)<sup>13</sup> and STO (3.22 eV)<sup>19</sup> requires absorption of UV radiation, which is a relatively small fraction of the total solar spectrum, resulting in very poor conversion efficiency. (The solar spectrum consists of 5% UV, 43% visible, and 52% infrared<sup>13</sup> ). It would therefore be desirable to lower the effective band gap of TiO<sub>2</sub> and STO to shift the absorption spectrum to the visible region. Extensive research has been done on the modification of TiO<sub>2</sub> and STO by various methods such as coupling with narrow band gap semiconductors,<sup>20-23</sup> doping with various metal<sup>24-26</sup> or nonmetal ions,<sup>27-29</sup> surface treatments with organic compounds,<sup>30-32</sup> or inorganic metal complexes,<sup>33-35</sup> to promote greater visible light absorption.

Recently, Co-doping and Co treatment of semiconducting photoanodes have been studied, which have demonstrated a significantly higher photocatalytic activity in the visible light region compared to undoped or untreated photoanodes.<sup>36-40</sup> Among those, a study on Co treatment of TiO<sub>2</sub> has explained that Co treatment has a dual role of passivating the surface of TiO<sub>2</sub> to increase hole lifetime, and of forming a cobalt-based water oxidation catalyst layer.<sup>36</sup> Cobalt oxides (CoO<sub>x</sub>) have been suggested as catalysts for the oxidation half reaction to form oxygen in the photoanode.<sup>36-38</sup> Loading cobalt oxides onto the photoanode has been proposed as a method of providing a significant improvement in water splitting performance.<sup>36-40</sup> To date, the cobalt treatment or loading has been performed by dipping a photoanode into Co<sup>2+</sup> solutions, usually Co(NO<sub>3</sub>)<sub>2</sub>. There are reports on growing CoO<sub>x</sub> on different substrates using different techniques such as sputtering,<sup>41</sup> pulsed laser deposition,<sup>42</sup> molecular beam epitaxy (MBE),<sup>43</sup> chemical vapor deposition,<sup>44,45</sup> and atomic layer deposition (ALD).<sup>46,47</sup> Among these methods,

ALD offers several advantages such as uniform deposition over large area substrates, good conformality and compatibility at low deposition temperatures. To our knowledge, epitaxial ALD growth of CoO films has not been studied. While a considerable amount of work has been done for the CoO-based catalysts in the literature, a detailed understanding of the photocatalytic activity and the electronic structure of the cobalt oxide/titanate systems is lacking. Since such knowledge could suggest new ways of advancing current hydrogen production technology using sunlight, a detailed study based on a well-defined model system is crucial and timely.

To better understand the role of cobalt oxide in photocatalytic water splitting when it is coupled with a semiconductor material such as STO and TiO<sub>2</sub>, we synthesize model systems of CoO/STO and CoO/TiO<sub>2</sub> having a well-defined crystalline, epitaxial interface and analyze their composite electronic structure. Since direct epitaxial metal oxide growth on Si has not been demonstrated by ALD itself, in this study, 1.6 nm STO-buffered Si(001) substrates grown by MBE were used for low temperature ALD of TiO<sub>2</sub>, STO, and CoO. We show that PEC tests of both types of stacks, CoO/STO/Si and CoO/TiO<sub>2</sub>/STO/Si, have photoactivity in the visible light region. The band offsets of the two heterojunctions CoO/STO and CoO/TiO<sub>2</sub> have been measured using *in-situ* high-energy resolution core level and valence band X-ray photoelectron spectroscopy (XPS). To better understand the origin of the band offset at the heterointerfaces, we also calculated the electronic structure of the CoO/STO(001) heterostructure using density functional theory (DFT) and suggest a mechanism for the observed visible light photoactivity.

## 6.2. EXPERIMENTAL AND THEORETICAL DETAILS

Four unit cells of STO on Si(001) grown by MBE were prepared and used as substrates for ALD growth. The 0.5 mm-thick substrates were cut into  $20 \times 20 \text{ mm}^2$  from prime Si(001) wafers. The substrates were ultrasonically cleaned with acetone, isopropyl alcohol, and deionized water for 5 min each, followed by UV/ozone treatment for 15 min to remove residual carbon contamination. The degreased wafers were loaded into the MBE chamber where four unit cells of STO were deposited on Si(001) using a variant of the Motorola-developed process,<sup>48</sup> as described in more detail elsewhere.<sup>49,50</sup> After growth, the four unit cell STO-buffered Si(001) substrates were transferred *in vacuo* to the ALD system for subsequent deposition.

The ALD system is a custom-built, hot-wall stainless steel rectangular 20-cm long chamber, with a reactor volume of  $460 \text{ cm}^3$ .<sup>49</sup> Ultrahigh purity argon was used as a purge/carrier gas.  $\text{TiO}_2$  and STO films were grown using titanium tetraisopropoxide, and strontium bis(triisopropylcyclopentadienyl), with water as the oxidant. The substrates were maintained at  $250 \text{ }^\circ\text{C}$  throughout the deposition of  $\text{TiO}_2$  and STO. The substrate temperature was monitored with a reference thermocouple in the ALD chamber that was previously calibrated against an instrumented wafer. The deposition processes, film thicknesses, and growth rates of  $\text{TiO}_2$  and STO were described in our previous studies.<sup>49,51,52</sup>

$\text{CoO}$  films were grown on four unit cell MBE-grown STO, on ALD-grown STO, and on ALD-grown  $\text{TiO}_2$  using cobalt bis(diisopropylacetamidinate). Water was again used as the oxidant and was maintained at room temperature ( $26 \text{ }^\circ\text{C}$ ). During  $\text{CoO}$  growth, the Co precursor was held at  $56 \text{ }^\circ\text{C}$ , while the substrate was maintained at a temperature range of  $170\text{-}180 \text{ }^\circ\text{C}$ . This low temperature is used to minimize the potential reaction between  $\text{CoO}$  and Si due to oxygen diffusion through the four unit cell STO

layers. Attempts to deposit CoO films at higher ALD temperatures resulted in some reduced Co species. The water dosing was regulated using an in-line needle valve. Each cycle of CoO growth consisted of a 2 sec dose of Co, a 10 sec purge of Ar, a 2 sec dose of H<sub>2</sub>O, and a 10 sec purge of Ar.

X-ray reflectivity (XRR) was used to determine the CoO film thicknesses. The CoO growth rate was found to be 0.04 nm/cycle. The CoO film crystallinity and orientation were determined by reflection high-energy electron diffraction (RHEED) and X-ray diffraction (XRD). XRR and XRD were conducted using a Bruker-AXS D8 Advance Powder Diffractometer using a sealed tube Cu K $\alpha$  radiation source with the wavelength of 1.5406 Å while RHEED was performed using a Staib Instruments RHEED gun operated at 18 keV energy and 3° grazing incidence. A Veeco Multimode V atomic force microscope (AFM) was used to image the topography and measure the surface roughness of the CoO films. Cross-sectional transmission electron microscopy (TEM) was used to confirm the crystallinity and overall quality of the two stacks CoO/STO/Si and CoO/TiO<sub>2</sub>/STO/Si. The TEM analysis was carried out using an FEI TITAN G2 instrument. The TEM samples were prepared using FEI Helios 400 ML. To avoid the thermal reduction and amorphization of CoO films, a protecting layer including amorphous silicon (sputter deposition), carbon (sputter deposition), and platinum (*in-situ* e-beam induced deposition) was coated on the surface of CoO films. The TEM lamellae were treated with a low energy (1-2 keV) Ga<sup>+</sup> milling to remove damaged sidewalls, forming a final TEM sample thickness of about 20 nm. The *in-situ* VG Scienta R3000 XPS system with a monochromated Al K $\alpha$  source at 1486.6 eV was used to determine the stoichiometry and oxidation states of cobalt, and to measure the band alignment of two heterojunctions CoO/STO and CoO/TiO<sub>2</sub>. The absolute energy scale of the analyzer of

the XPS system is calibrated using a two-point measurement such that the Ag  $3d_{5/2}$  core level is at 368.26 eV and the Fermi edge of Ag is at 0.0 eV.

The PEC tests were performed using a three-electrode PEC cell with the three stacks TiO<sub>2</sub>/STO, CoO/STO, and CoO/TiO<sub>2</sub>/STO on Si(001) substrates as the working electrode, a Ag/AgCl (saturated KCl) reference electrode, a platinum wire counter electrode, and 1 M KOH electrolyte (pH=13.5). The working electrode with an exposed area of 0.205 cm<sup>2</sup> was illuminated by a solar simulator (Newport, Model 9600, 150 W xenon lamp) equipped with an AM 1.5 G filter (Newport, Model 81094). The light intensity was measured as 100 mW/cm<sup>2</sup> using a thermopile detector with the spectrum response from 0.19 to 10.6 μm (Newport, 818P-020-12). An UV filter that blocks all the wavelengths shorter than 420 nm was used for visible light experiments. A CHI 660D electrochemical station was used for linear sweep voltammetry (I-V) and chronoamperometry (I-t) measurements.

For the theoretical calculation of the band alignment of a CoO/STO heterojunction, we use DFT as implemented in the VASP code.<sup>53</sup> Local density approximation, using the Ceperley-Alder data parametrized by Perdew and Zunger,<sup>54</sup> is employed to treat the exchange-correlation energy along with projector augmented wave pseudopotentials<sup>55</sup> to describe Sr, Ti, Co, and O. The valence configurations for these elements are  $4s^2 4p^6 5s^2$  for Sr,  $3p^6 3d^2 4s^2$  for Ti,  $3d^7 4s^2$  for Co, and  $2s^2 2p^4$  for O. We use a cutoff energy of 600 eV for the plane-wave expansion. Each self-consistent electronic calculation is converged to  $10^{-6}$  eV/cell, and the ionic degrees of freedom are fully relaxed until the forces are less than 10 meV/Å. To describe the static electronic correlation effect in the  $3d$  orbital spaces of the transition metal ions and the local magnetic moment of Co<sup>2+</sup>, we use local spin density approximation with the Hubbard  $U$  correction (LSDA+ $U$ ) in the rotationally invariant formalism.<sup>56</sup> We apply  $U_{eff}$  ( $=U-J$ ) of

3.0 eV on the Co  $3d$ <sup>57</sup> and 4 eV on the Ti  $3d$  orbitals. A Gamma-point centered  $4 \times 4 \times 1$  Monkhorst-Pack  $k$ -point grid is used to sample the Brillouin zone of the CoO/STO (001) superlattice (dimensions =  $7.79 \text{ \AA} \times 7.79 \text{ \AA} \times 33.03 \text{ \AA}$ ).

## 6.3. RESULTS AND DISCUSSION

### 6.3.1. Cobalt oxidation state

The electronic structure of Co causes a characteristic satellite structure in the Co  $2p$  core level,<sup>58</sup> depending on the oxidation and even spin states. Figures 6.1a and 6.1b show the Co  $2p$  and O  $1s$  X-ray photoelectron (XP) spectra of an 8-nm ALD cobalt oxide film grown on four unit cell STO-buffered Si(001). The binding energies of the main peaks are at 780.4 eV and 796.5 eV for Co  $2p_{3/2}$  and Co  $2p_{1/2}$  levels, respectively, and at 786.7 eV and 803.0 eV for the Co  $2p_{3/2}$  and Co  $2p_{1/2}$  for satellite peaks, respectively. The  $2p$  binding energy position in conjunction with the very strong satellite at 6 eV higher binding energy is consistent with Co being in the +2 valence state with high spin.<sup>59</sup> The binding energy of O  $1s$  is at 530.2 eV. The atomic ratio Co:O in the films was found to be 1:1.07 confirming Co is in the +2 valence state. The Co  $2p$  and O  $1s$  spectra of CoO films grown on thicker ALD STO and on ALD anatase ( $\text{TiO}_2$ ) (not shown) were found to be the same as those of CoO films grown on four unit cell STO-buffered Si(001). In all cases, there was some residual (<2%) carbon contamination in the as-deposited CoO films.

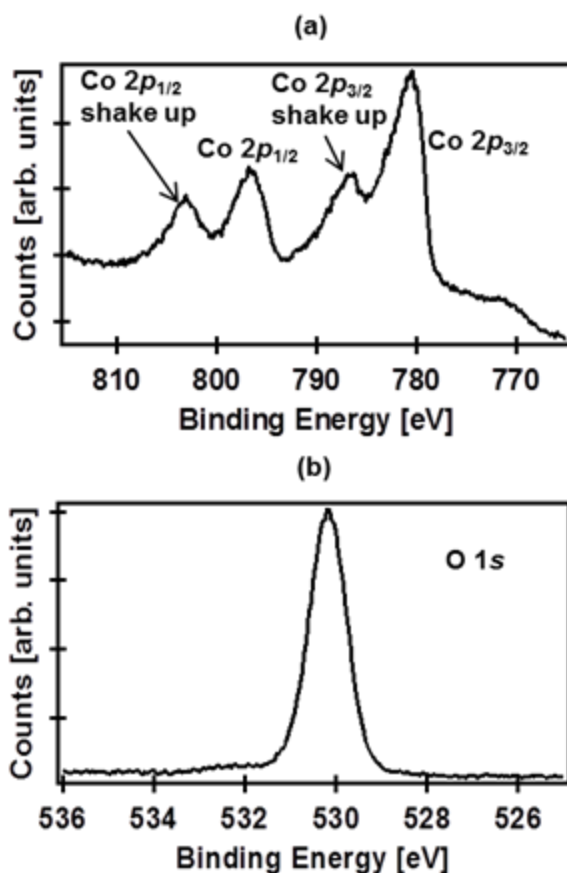


Figure 6.1. Core level Co  $2p$  (a) and O  $1s$  (b) XP spectra of an 8-nm ALD CoO film grown on four unit cell STO-buffered Si(001).

### 6.3.2. Crystallinity and roughness of CoO/STO and CoO/TiO<sub>2</sub> films

Figure 6.2a shows typical RHEED patterns of a four unit cell STO-buffered Si(001) substrate grown by MBE, indicating that the STO layer is highly crystalline with a flat surface. The RHEED patterns of a 10-nm TiO<sub>2</sub> film grown on four unit cell STO (Figures 6.2b) indicate the TiO<sub>2</sub> films are crystalline with some roughness, which is consistent with our previous work.<sup>52</sup> Figures 6.2c presents the RHEED patterns of a 4-nm CoO film grown on four unit cell STO indicating good crystallinity of CoO and an in-plane orientation that is in registry with the underlying STO layer. The RHEED patterns of CoO on a 10-nm TiO<sub>2</sub> film in Figure 6.2d shows transmission diffraction features,

indicating that the CoO film on TiO<sub>2</sub> is very rough, and appear the same at all azimuthal directions, indicating that the CoO film on TiO<sub>2</sub> is not epitaxial. Thicker STO films were grown on four unit cell STO-buffered Si(001) by ALD using the process described elsewhere.<sup>49</sup> CoO films grown on these thicker ALD STO layers also exhibit high crystallinity (see below), similar to CoO films grown on the four unit cell STO-buffered Si(001). All RHEED patterns in Figures 2(a-d) were taken along the <100> direction of STO.

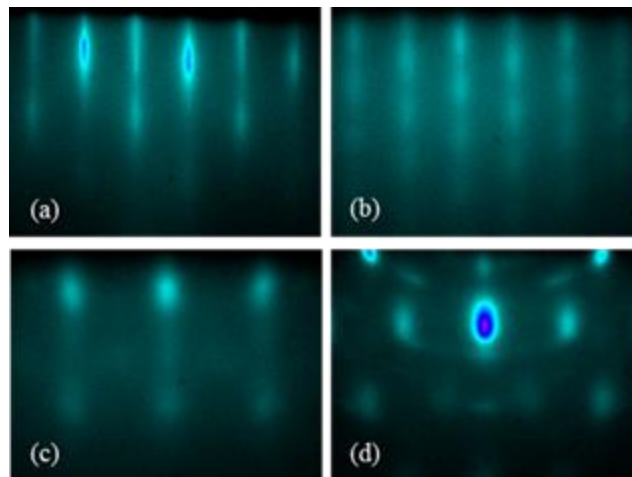


Figure 6.2. RHEED images of: (a) a four unit cell STO-buffered Si(001) grown by MBE, (b) a 10-nm ALD-grown TiO<sub>2</sub> on four unit cell STO-buffered Si(001), (c) a 4-nm ALD-grown CoO on four unit cell STO-buffered Si(001), and (d) a 4-nm CoO film on a 10-nm ALD-grown TiO<sub>2</sub> on four unit cell STO-buffered Si(001). All RHEED patterns were taken along <100> direction of STO.

Surface morphology of the CoO films was analyzed using AFM. The root-mean-square surface roughness of 8-nm thick CoO films on four unit cell STO (Figure 6.3a), on thicker ALD STO (10-nm) (not shown), and on ALD TiO<sub>2</sub> (10-nm) (Figure 6.3b) are 0.92 nm, 1.18 nm, 2.21 nm, respectively. This confirms the RHEED observation that

CoO films grown by ALD are rough, especially CoO films grown on ALD TiO<sub>2</sub>, compared to four unit cell STO layer grown by MBE.

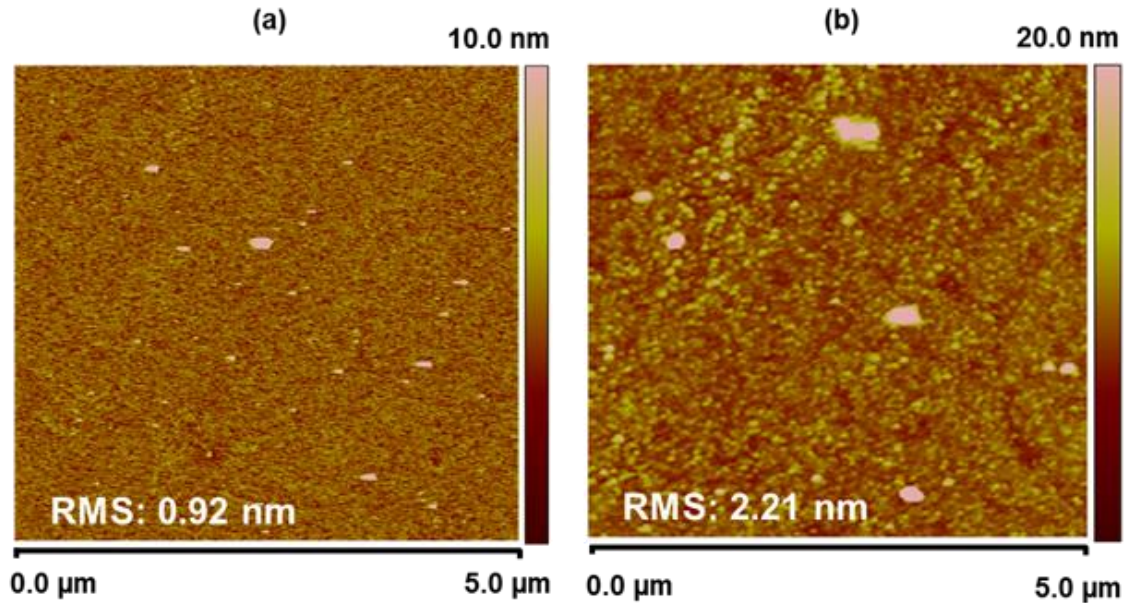


Figure 6.3. 2D AFM images of (a) an 8-nm thick ALD-grown CoO on four unit cell STO-buffered Si(001), and (b) an 8-nm thick ALD-grown CoO on 10-nm thick ALD-grown TiO<sub>2</sub> stack layer on four unit cell STO-buffered Si(001).

Figure 6.4a and the inset of Figure 6.4a represent the  $(\theta-2\theta)$  scan and the rocking curve of a 24-nm thick CoO film on four unit cell STO-buffered Si(001) as-deposited. The CoO(002) Bragg peak is dominant, appears at  $2\theta=42.60^\circ$ , and corresponds to an out-of-plane lattice constant of 4.24 Å. A very weak CoO(111) Bragg peak appears at  $2\theta=36.62^\circ$ . This confirms the predominantly *c*-axis orientation of the crystalline CoO films consistent with rock-salt CoO lattice constant of 4.26 Å. The XRD rocking curve around the (002) Bragg peak shows a full width at half maximum of 2.2°; this relatively large value is attributed to the lattice mismatch between CoO and Si (11.0%). Figure 6.4c shows the  $(\theta-2\theta)$  scan of an 8-nm CoO film on a 10 nm ALD STO on four unit cell STO-buffered Si(001). The CoO(002) Bragg peak also appears at 42.60°, while the STO(001)

and STO(002) peaks appear at 22.78 and 46.52°, respectively. The epitaxial relationships of CoO films with the Si substrate were verified by  $\phi$ -scans of the {113} reflections of CoO and the {115} reflections of silicon. The epitaxial alignment was found to be  $(001)_{\text{CoO}} \parallel (001)_{\text{STO}} \parallel (001)_{\text{Si}}$  and  $(100)_{\text{CoO}} \parallel (100)_{\text{STO}} \parallel (110)_{\text{Si}}$ . This shows that the CoO layer is aligned with the STO layer, which is rotated by 45° with respect to the silicon unit cell.<sup>52</sup> Figure 6.4b represents the ( $\theta$ -2 $\theta$ ) scan of a 10-nm thick CoO film on a 10 nm ALD TiO<sub>2</sub> (anatase) film. Similarly, the CoO(002) Bragg peak is dominant and appears at 2 $\theta$ =42.60°, with a weak CoO(111) Bragg peak that appears at 2 $\theta$ =36.62°, confirming the predominantly *c*-axis orientation of the CoO films on TiO<sub>2</sub>. However, a  $\phi$ -scan of CoO grown on TiO<sub>2</sub> shows that the CoO film on TiO<sub>2</sub> is not epitaxial. It is not yet clear why CoO grows epitaxially on STO but not on TiO<sub>2</sub>. The larger mismatch of CoO to TiO<sub>2</sub> may be a factor.

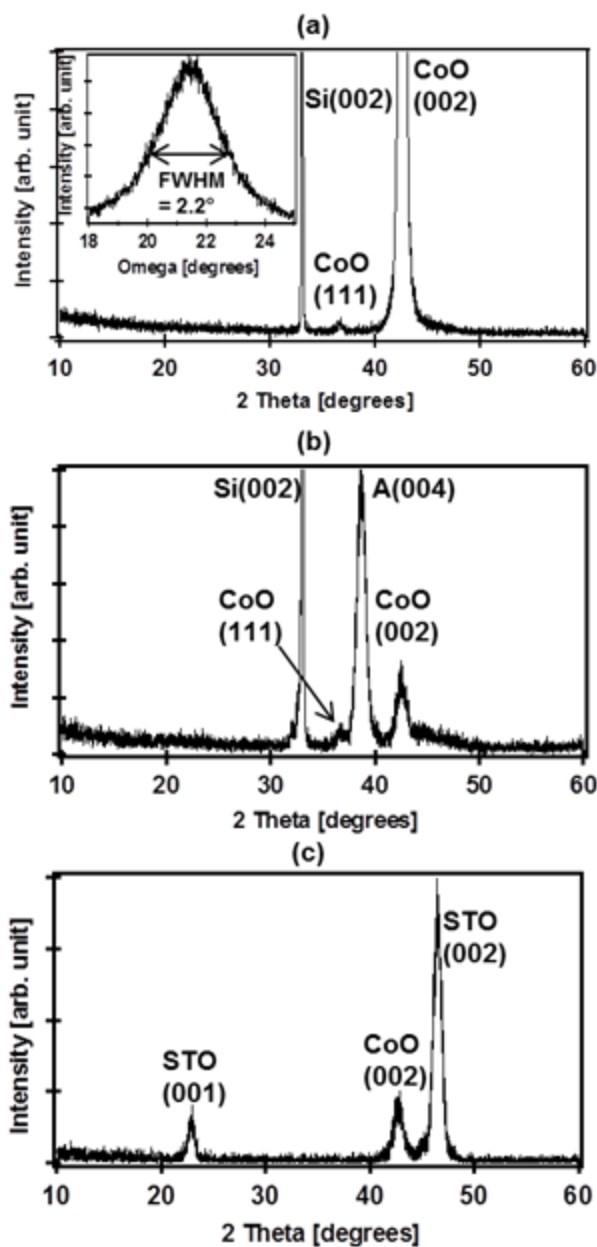


Figure 6.4. (a) XRD patterns of a 24-nm thick CoO film on four unit cell STO-buffered Si(001) and rocking curve pattern (inset) of the CoO(002) Bragg peak at a fixed  $2\theta=42.60^\circ$ , (b) XRD patterns of a 10-nm thick CoO film on ALD-grown 10-nm  $\text{TiO}_2$  stack layer on four unit cell STO-buffered Si(001), (c) XRD patterns of an 8-nm CoO film on a 10-nm ALD STO on four unit cell STO-buffered Si(001). Note: Si(002) peak was not observed in Figure 6.4c.

Figure 6.5a shows a cross-sectional Z-contrast high resolution scanning transmission electron microscopy (STEM) image of a 24-nm CoO film on four unit cell STO-buffered Si(001), showing little to no amorphous layer at the STO/Si interface and the high degree of crystallinity of all the deposited layers with very sharp interfaces. The out-of-plane lattice constant of CoO film was found to be 4.26 Å, which is consistent with the XRD data and bulk value of rock-salt CoO, indicating CoO film is fully relaxed. TEM analysis also shows that the STO/Si interface is very unstable and is partially amorphized by the E-beam during the TEM analysis. Figure 6.5b shows a cross-sectional Z-contrast high resolution STEM image of a 13-nm CoO film on ALD TiO<sub>2</sub>, confirming that the crystalline CoO is not epitaxial, but highly oriented. Figure 6.5b also shows that the CoO films grown by ALD have a rough top surface, which is consistent with the RHEED images and AFM data.

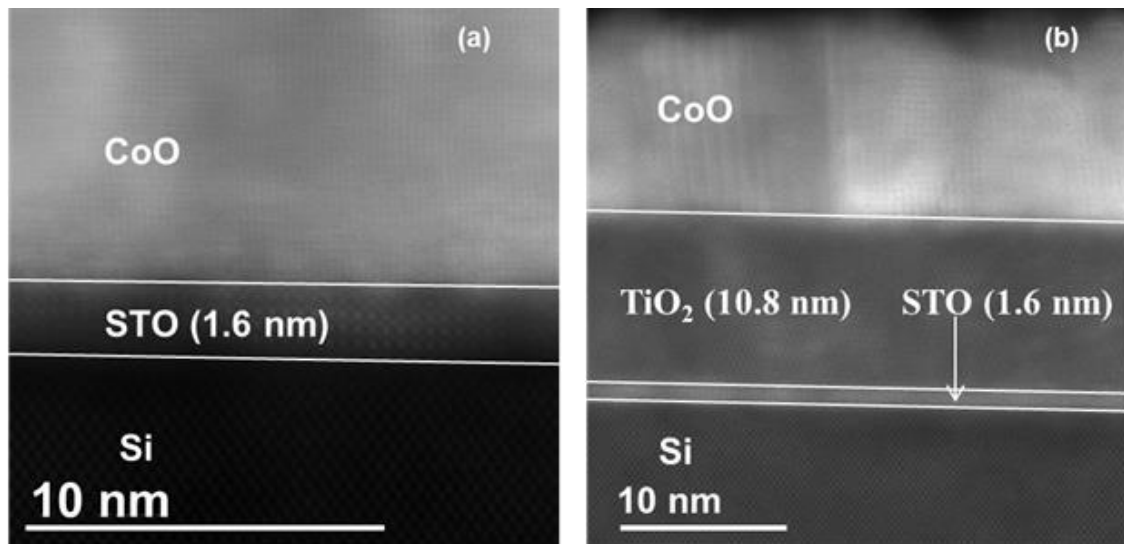


Figure 6.5. Cross-sectional STEM images of: (a) a 24-nm CoO film on four unit cell STO-buffered Si(001) grown by MBE, and (b) 13-nm CoO film on a 10.8 nm ALD-grown TiO<sub>2</sub> stack layer on four unit cell STO-buffered Si(001).

### 6.3.3. Visible light performance for water photooxidation

Figure 6.6 shows linear sweep voltammetry (scan rate of 25 mV/s) under dynamic light chopping illumination of three stacks TiO<sub>2</sub>(25 nm)/STO(1.6 nm)/Si(001), CoO(12 nm)/STO(13.6 nm)/Si, and CoO(12 nm)/TiO<sub>2</sub>(14 nm)/STO(1.6nm)/Si(001). To exclude the influence of the TiO<sub>2</sub> layer, the light source was coupled with an ultraviolet filter that blocks all wavelengths below 420 nm. We did not observe any PEC response for the TiO<sub>2</sub>/STO/Si sample (black curve) as expected since TiO<sub>2</sub> has a wide band gap (3.2 eV) and cannot absorb visible light photons. On the other hand, the CoO/STO and CoO/TiO<sub>2</sub>/STO/Si stacks clearly suggest visible light water photooxidation activity (blue curve and red curve, respectively). XPS was used to check the Co oxidation state of these three stacks before and after PEC testing. Co 2*p* XP spectra showed a slight difference of the area ratio of Co 2*p* main peaks: Co 2*p* satellite peaks (2-8%) for these stacks before and after PEC testing (not shown). This is due to the CoO on the surface reacting with O<sub>2</sub> to form a very thin layer of Co<sub>3</sub>O<sub>4</sub> as the CoO films were exposed to air. It also gives further indication that the photocurrent observed is due to the water photooxidation potential, rather than some other photooxidation process. The demonstration of photocurrent in visible light with CoO/TiO<sub>2</sub>(STO)/Si heterostructures is a promising result, although, the photocurrent density is still quite low (on the order of μA/cm<sup>2</sup>). We note that our planar CoO thin films have significantly fewer active sites than nanostructured TiO<sub>2</sub> materials for electrocatalysis and, additionally, our films are quite thin and do not allow for the absorption of a large fraction of the incident photons. We believe that conformally coating CoO on one dimensional nanostructured TiO<sub>2</sub> materials such as nanotubes, nanowires etc., could greatly enhance the visible light water splitting activity of the materials.

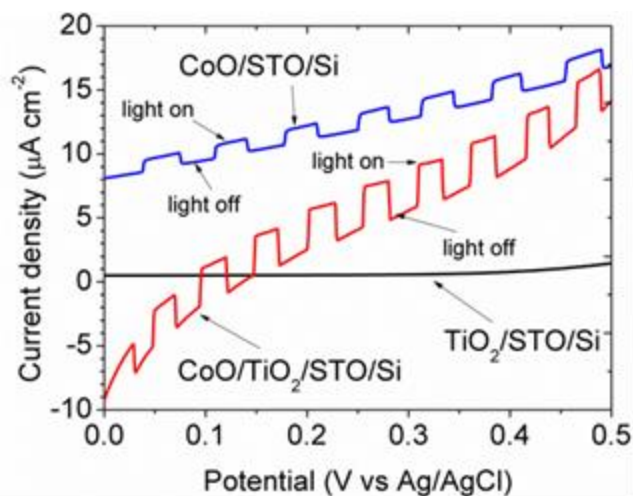


Figure 6.6. Linear sweep voltammetry (25 mV/s) of CoO(12 nm)/TiO<sub>2</sub>(14 nm)/STO(1.6 nm)/Si ( red curve), CoO(12 nm)/STO(13.6 nm)/Si (blue curve), and TiO<sub>2</sub>(25 nm)/STO(1.6 nm)/Si (black curve). An UV filter that blocked all wavelengths < 420 nm was used as the light source.

### 6.3.4. Band offsets of the CoO/STO and CoO/TiO<sub>2</sub> heterojunctions

#### 6.3.4.1. Experimental measurements

The band alignment of the layers in the entire structure is crucial to understanding the increased photoactivity of the CoO/STO and CoO/TiO<sub>2</sub> heterostructures compared to plain STO or TiO<sub>2</sub>. To study the band offset of the two heterojunctions, thick STO (16 nm), thick TiO<sub>2</sub> (12 nm), and thick CoO (14 nm) films were first grown on four unit cell STO-buffered Si(001) and transferred *in vacuo* to the XPS chamber. The valence band XP spectra (Figures 6.7a, 7c, and 7e) were used to determine the valence band maxima (VBM) for the individual materials by using a linear extrapolation method.<sup>60,61</sup> VBM were found to be  $2.93 \pm 0.05$ ,  $3.45 \pm 0.05$ , and  $1.12 \pm 0.05$  eV for STO, TiO<sub>2</sub>, and CoO, respectively. The binding energies were found to be 458.79, 459.49, and 780.82 eV for STO Ti 2p<sub>3/2</sub>, TiO<sub>2</sub> Ti 2p<sub>3/2</sub>, and CoO Co 2p<sub>3/2</sub>, respectively (Figures 6.7b, 7d and 7f). The Ti 2p<sub>3/2</sub> to VBM separation measured is consistent (a 0.09 eV difference) with the value

obtained by Chambers *et al.* for Nb-doped single crystal STO.<sup>62</sup> The binding energy difference between the core levels and the VBMs were used to reference the VBM of each material in the two heterojunctions CoO/STO and CoO/TiO<sub>2</sub> to the associated core level. To determine the binding energy difference between the Ti 2p<sub>3/2</sub> and Co 2p<sub>3/2</sub> levels for each of the two heterojunctions CoO/STO and CoO/TiO<sub>2</sub>, a thin layer of CoO (2.0 nm) was grown on thick ALD STO (14 nm) and TiO<sub>2</sub> (12 nm) samples. *In-situ* XPS was again used to check the binding energy differences. The core level positions and VBM of individual materials combined with core level differences of heterojunctions were used to calculate the valence band offset (VBO) as shown in Equations 1 and 2 (VBM of individual materials and core level binding energies associated with the two equations are listed in Table 6.1):

$$\Delta E_v (\text{CoO/STO}) = (E_{\text{Co}2p} - E_{\text{VBM}})_{\text{CoO}} - (E_{\text{Ti}2p} - E_{\text{VBM}})_{\text{STO}} - (E_{\text{Co}2p} - E_{\text{Ti}2p})_{\text{CoO/STO}} \quad (1)$$

$$\Delta E_v (\text{CoO/TiO}_2) = (E_{\text{Co}2p} - E_{\text{VBM}})_{\text{CoO}} - (E_{\text{Ti}2p} - E_{\text{VBM}})_{\text{TiO}_2} - (E_{\text{Co}2p} - E_{\text{Ti}2p})_{\text{CoO/TiO}_2} \quad (2)$$

The VBOs of the two heterojunctions CoO/STO and CoO/TiO<sub>2</sub> were determined to be 1.21 ± 0.10 and 1.61 ± 0.10 eV, respectively, with the CoO valence band maximum higher in energy than the STO or TiO<sub>2</sub> valence band maximum. Using the experimental VBOs from this work, the conduction band offsets were calculated according to Equations 3 and 4:

$$\Delta E_c (\text{CoO/STO}) = \Delta E_v (\text{CoO/STO}) - E_{\text{g}(\text{STO})} + E_{\text{g}(\text{CoO})} \quad (3)$$

$$\Delta E_c (\text{CoO/TiO}_2) = \Delta E_v (\text{CoO/TiO}_2) - E_{\text{g}(\text{TiO}_2)} + E_{\text{g}(\text{CoO})} \quad (4)$$

where E<sub>g(STO)</sub>, E<sub>g(TiO<sub>2</sub>)</sub>, and E<sub>g(CoO)</sub> are the band gap of STO, TiO<sub>2</sub>, and CoO films, respectively. Taking the band gaps for STO, TiO<sub>2</sub>, and CoO to be 3.22, 3.20, and 2.40 eV, respectively,<sup>13,19</sup> the values for conduction band offsets ΔE<sub>c</sub> (CoO/STO) and ΔE<sub>c</sub> (CoO/TiO<sub>2</sub>) are found to be 0.39 eV ± 0.10 and 0.81 ± 0.10 eV, respectively, with the CoO conduction band minimum higher in energy than the STO or TiO<sub>2</sub> conduction band

minimum. Figure 6.8c summarizes the measured band alignment for the two types of heterojunctions CoO/STO and CoO/TiO<sub>2</sub>.

Materials	CoO	STO	TiO <sub>2</sub>	CoO/STO	CoO/TiO <sub>2</sub>
Co $2p_{3/2}$ (eV)	780.82	-	-	781.25	781.39
Ti $2p_{3/2}$ (eV)	-	458.79	459.49	458.62	459.34
VBM (eV)	1.12	2.93	3.45	-	-

Table 6.1. VBMs of pure CoO, STO, TiO<sub>2</sub> and associated core level binding energies

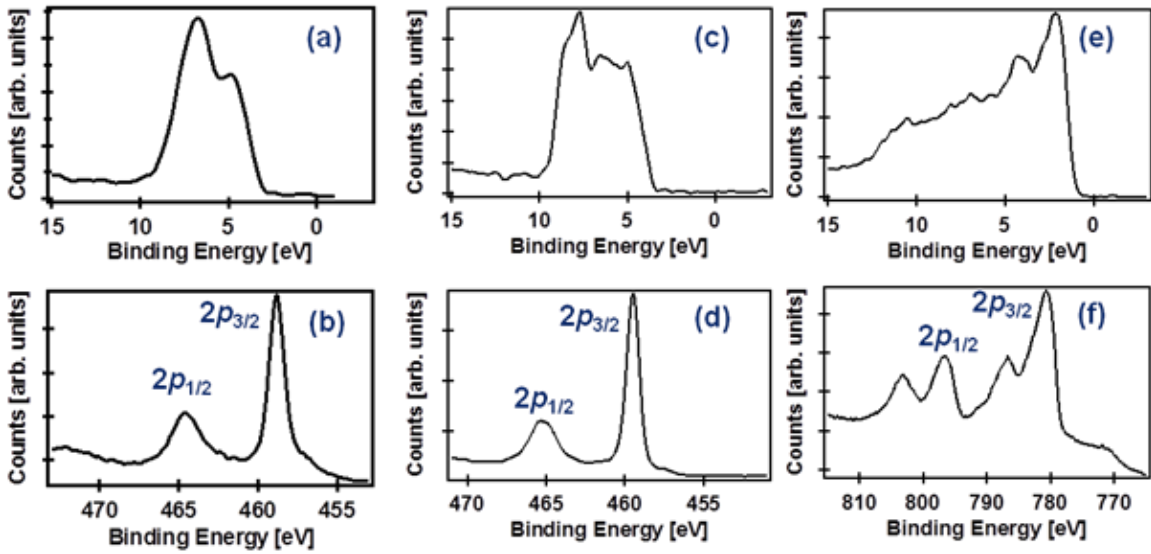


Figure 6.7. Valence band XP spectra for STO (a), TiO<sub>2</sub> (c), and CoO (e), core level XP spectra for STO Ti 2p (b), TiO<sub>2</sub> Ti 2p (d), and CoO Co 2p (f).

#### 6.3.4.2. Theoretical calculations

Density functional calculations using the local spin density approximation with the Hubbard  $U$  correction (LSDA+ $U$ ) were carried out to determine the valence band offsets expected from an ideal CoO/STO (001) interface. The CoO overlayer is assumed to be in the type-II antiferromagnetic state, which is the ground state of CoO bulk

crystal.<sup>57</sup> We first calculate the valence band offset in the Schottky limit where no interaction is present between the two oxides to be 1.84 eV, with the CoO valence band maximum inside the band gap of STO. To calculate the offset at the heterointerface, a STO/CoO interface with a lateral size of  $2 \times 2$  unit cells is constructed with the CoO strained to match STO. Note, the CoO overlayer is strained due to computational resource limitations. In Figure 6.8a, we plot the constructed heterostructure and calculated layer-by-layer projected density of states. The states at the top of the valence band in STO are mainly O  $2p$  states, while they are mainly the Co  $3d t_{2g}$  states in CoO. By comparing the valence band maximum position in the bulk-like region of STO and the bulk-like region of CoO, we calculate the valence band offset to be 1.85 eV, with the CoO valence band maximum positioned at higher energy. The theoretical result is larger than the measured value (1.21 eV) which may be a result of the large strain in STO in the theoretical calculation and the assumption of a defect-free interface. The presence of defects such as oxygen vacancies have been known to reduce experimentally measured band offsets from the ideal, theoretical values.<sup>63</sup> The actual calculated band offset using the heterostructure is close to that in the Schottky limit because the charge transfer from CoO to STO is largely screened by O lattice polarization at the interface.<sup>55</sup> In Figure 6.8b, we show a schematic of the carrier generation, separation, and reaction with water that occur in the CoO/STO heterostructure. Since the Co  $t_{2g}$  states are positioned inside the band gap of STO, it effectively reduces the band gap of the entire system and allows absorption of visible light by exciting electrons from the Co  $t_{2g}$  states to the empty Ti  $3d$  states at the interface. As a result of the band alignment, with the CoO conduction band being higher in energy than the STO conduction band, the photogenerated electrons are swept into the STO layer, through the Si substrate (zero conduction band offset to STO<sup>64</sup>)

and into the Pt counter electrode to reduce water. The photogenerated holes on the other hand, can move to the surface of CoO and react with water to form oxygen molecules.

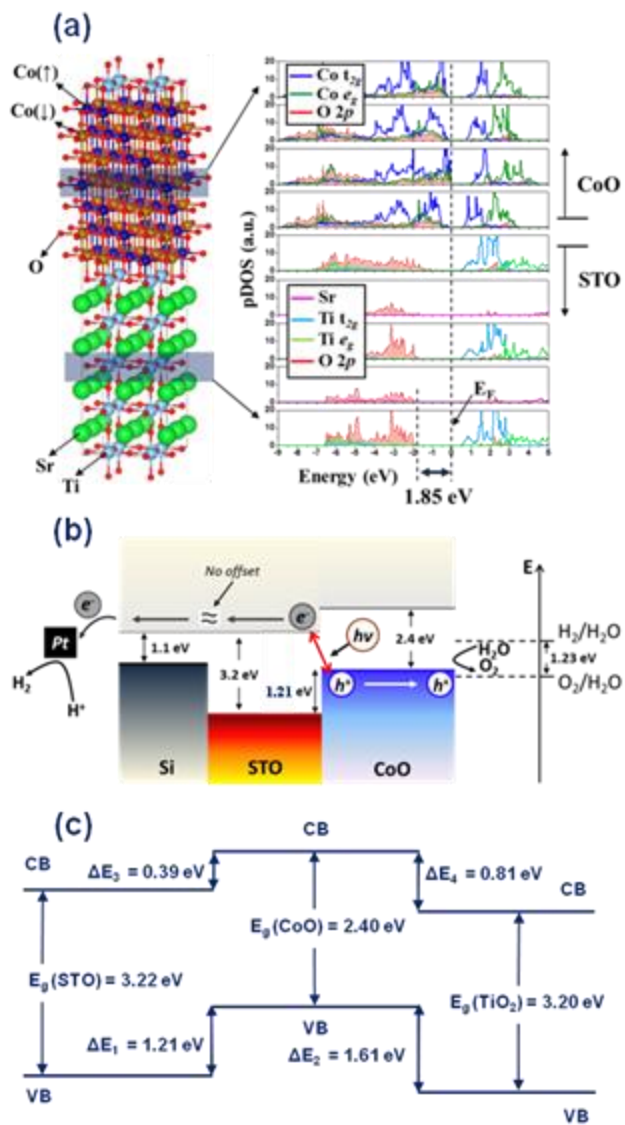


Figure 6.8. (a) Ball-and-stick model and layer-by-layer projected density of states (pDOS) of the CoO/STO (001) heterostructure. The STO layer is 4 unit cells thick and the CoO layer is 3 unit cells thick with a (2×2) in-plane cell size (dimension = 7.79 Å × 7.79 Å). The type-II antiferromagnetic phase is considered for the CoO layer with spin-up (↑) Co<sup>2+</sup> and spin-down (↓) Co<sup>2+</sup> represented with dark-blue and orange balls. (b) Schematic of band alignment of the Si/STO/CoO (001) heterostructure, generation and separation of electron-hole pair across the interface, and oxidation and reduction of water to form oxygen and hydrogen at the surfaces. (c) Band alignment for two types of heterojunctions CoO/STO and CoO/TiO<sub>2</sub> determined experimentally using *in-situ* high-energy resolution core level and valance band XPS.

## 6.4. SUMMARY

The band alignment of CoO and two widely used photocatalysts TiO<sub>2</sub> and STO hold promise of catalytic activity in the visible region of the spectrum. Epitaxial CoO films were grown on STO-buffered Si(001) and on ALD STO, while highly oriented CoO films were grown on ALD TiO<sub>2</sub> by ALD at a temperature range of 170-180 °C. The crystallinity was determined by RHEED, XRD and TEM. The low temperature was used to minimize the reaction between CoO and Si due to the oxygen diffusion through four unit cell STO. The two heterostructures CoO/STO/Si and CoO/TiO<sub>2</sub>/STO/Si indeed demonstrate the visible light water photooxidation activity. The band alignment of two heterostructures CoO/STO and CoO/TiO<sub>2</sub> was measured using *in-situ* XPS, and the electronic structure was calculated using DFT with the assumption of a defect-free interface. The band alignment clearly suggests a mechanism for visible light water photooxidation activity. We believe that conformal deposition of CoO on one dimensional nanostructured TiO<sub>2</sub> materials will greatly enhance the visible light water photooxidation activity of the materials.

## 6.5. REFERENCES

- <sup>1</sup>J. Overpeck, K. Huguen, D. Hardy, R. Bradley, R. Case, M. Douglas, B. Finney, K. Gajewski, G. Jacoby, A. Jennings, S. Lamoureux, A. Lasca, G. MacDonald, J. Moore, M. Retelle, S. Smith, A. Wolfe, and G. Zielinski, *Science* **278**, 1251 (1997).
- <sup>2</sup>E. Chornet and S. Czernik, *Nature* **418**, 928 (2002).
- <sup>3</sup>J. Ng, S. Xu, X. Zhang, H. Y. Yang, and D. D. Sun, *Adv. Funct. Mater.* **20**, 4287 (2010).
- <sup>4</sup>J. Rothstein, *Internatl. J. Hydrogen Energy* **21**, 137 (1996).
- <sup>5</sup>G. W. Crabtree, M. S. Dresselhaus, and M. V. Buchanan, *Phys. Today* **39** (2004).
- <sup>6</sup>S. Czernik, R. French, C. Feik, and E. Chornet, U.S. DOE Hydrogen Program Review, UREL/CP-610, 32405 (2002).

- <sup>7</sup>A. Fujishima and K. Honda, *Nature* **238**, 37 (1972).
- <sup>8</sup>J. G. Mavroides, J. A. Kafalas, and D. F. Kolesar, *Appl. Phys. Lett.* **28**, 141 (1976).
- <sup>9</sup>A. J. Bard and M. A. Fox, *Acc. Chem. Res.* **28**, 141(1995).
- <sup>10</sup>Z. Zou, J. Ye, K. Sayama, and H. Arakawa, *Nature* **414**, 625 (2001).
- <sup>11</sup>S. Y. Reece, J. A. Hamel, K. Sung, T. D. Jarvi, A. J. Esswein, J. J. H. Pijpers, and D. G. Nocera, *Science* **334**, 645 (2011).
- <sup>12</sup>S. Yamane, N. Kato, S. Kojima, A. Imanishi, S. Ogawa, N. Yoshida, S. Nonomura, and Y. Nakato, *J. Phys. Chem. C* **113** (32), 14575 (2009).
- <sup>13</sup>S. G. Kumar and L. G. Devi, *J. Phys. Chem. A* **115**, 13211 (2011).
- <sup>14</sup>S. Hara, M. Yoshimizu, S. Tanigawa, L. Ni, B. Ohtani, and H. Irie, *J. Phys. Chem. C* **116**, 17458 (2012).
- <sup>15</sup>J. Jitputti, S. Pavasupree, Y. Suzuki, and S. Yoshikawa, *J. Solid State Chem.* **180**, 1743 (2007).
- <sup>16</sup>A. Fujishima, T. N. Rao, and D. A. Tryk, *J. Photochem. Photobiol. C: Photochem. Rev.* **1**, 1 (2000).
- <sup>17</sup>J. Tang, J. R. Durrant, and D. R. Klug, *J. Am. Chem. Soc.* **130**, 13885 (2008).
- <sup>18</sup>K. Hashimoto, H. Irie, and A. Fujishima, *Japan. J. Appl. Phys.* **44**, 8269 (2005).
- <sup>19</sup>J. H. Ma, Z. M. Huang, X. J. Meng, S. J. Liu, X. D. Zhang, J. L. Sun, J. Q. Xue, and J. H. Chu, *J. Appl. Phys.* **99**, 033515 (2006).
- <sup>20</sup>R. Vogel, K. Pohl, and H. Weller, *Chem. Phys. Lett.* **174**, 241 (1990).
- <sup>21</sup>H. Kim, M. Seol, J. Lee, and K. Yong, *J. Phys. Chem. C* **115**, 25429 (2011).
- <sup>22</sup>J. Zhang, H. Zhu, S. Zheng, F. Pan, and T. Wang, *Appl. Mater. Inter.* **1**, 2111 (2009).
- <sup>23</sup>L. J. Diguna, Q. Shen, J. Kobayashi, and T. Toyoda, *Appl. Phys. Lett.* **91**, 023116 (2007).
- <sup>24</sup>L. G. Devi, N. Kottam, and S. G. Kumar, *J Phys. Chem. C* **113**, 15593 (2009).

- <sup>25</sup>S. Binham and W. A. Daoud, *J. Mater. Chem.* **21**, 2041 (2011).
- <sup>26</sup>S. Kawasaki, K. Nakatsuji, J. Yoshinobu, F. Komori, R. Takahashi, M. Lippmaa, K. Mase, and A. Kudo, *Appl. Phys. Lett.* **101**, 033910 (2012).
- <sup>27</sup>S. U. M. Khan, M. Al-Shahry, and W. B. Ingler, *Science* **297**, 2243 (2002).
- <sup>28</sup>T. Hirakawa and Y. Nosaka, *J. Phys. Chem. C*, **112**, 15818 (2008).
- <sup>29</sup>D. Li, H. Haneda, N. K. Labhestwar, S. Hishita, and N. Ohashi, *Chem. Phys. Lett.* **401**, 579 (2005).
- <sup>30</sup>G. Benko, J. Kallioinen, J. E. I. K. Tommola, A. P. Yarstev, and V. Sundstrom, *J. Am. Chem. Soc.* **124**, 489 (2002).
- <sup>31</sup>M. Yin, Z. Li, J. Kou, and Z. Zou, *Environ. Sci. Technol.* **43**, 8361 (2009).
- <sup>32</sup>H. S. Hilal, L. Z. Majjad, N. Zaatar, and A. E. Hamouz, *Solid State Sci.* **9**, 9 (2007).
- <sup>33</sup>L. Zhang, C. Lange, I. Abraham, S. Storck, W. F. Maier, and H. Kisch, *J. Phys. Chem. B* **102**, 10765 (1998).
- <sup>34</sup>H. Kisch, L. Zhang, C. Lange, W. F. Maier, C. Antonius, and D. Meissner, *Angew. Chem. Int. Ed.* **37**, 3034 (1998).
- <sup>35</sup>G. Burgeth and H. Kisch, *Coord. Chem. Rev.* **230**, 41 (2002).
- <sup>36</sup>S. Hoang, S. Guo, N. T. Hahn, A. J. Bard, and C. B. Mullins, *Nano Lett.* **12**, 26 (2012).
- <sup>37</sup>A. Kay, I. Cesar and M. Grätzel, *J. Am. Chem. Soc.* **128**, 15714 (2006).
- <sup>38</sup>M. W. Kanan and D. G. Nocera, *Science* **321**, 1072 (2008).
- <sup>39</sup>D. K. Zhong and D. R. Gamelin, *J. Am. Chem. Soc.* **132**, 4202 (2010).
- <sup>40</sup>D. K. Zhong, S. Choi, and D. R. Gamelin, *J. Am. Chem. Soc.* **133**, 18370 (2011).
- <sup>41</sup>H. Yamamoto, T. Naito, M. Terao, and T. Shintani, *Thin Solid Films* **411**, 289 (2002).
- <sup>42</sup>T. Warang, N. Patel, A. Santini, N. Bazzanella, A. Kale, A. Miotello, *Appl. Catal.* **213-214**, 21 (2012).

- <sup>43</sup>C. A. F. Vaz, D. Brabhakaran, E. I. Altman, and V. E. Henrich, *Phys. Rev. B* **80**, 155457 (2009).
- <sup>44</sup>M. Burriel, G. Garcia, J. Santiso, A. Abruits, Z. Saltyte, and A. Figueras, *Chem. Vap. Deposition* **11**, 106 (2005).
- <sup>45</sup>J. Tyczkowski, R. Kapica, and J. Lojewska, *Thin Solid Films* **515**, 6590 (2007).
- <sup>46</sup>M. Diskus, O. Nilsen, and H. Fjellvåg, *Chem. Vap. Deposition* **17**, 135 (2011).
- <sup>47</sup>M. E. Donders, H. C. M. Knoop, M. C. M. Van de Sanden, W. M. M. Kessels, and P. H. L. Notten, *J. Electrochem. Soc.* **158**, G92 (2011).
- <sup>48</sup>Z. Yu, J. Ramdani, J. A. Curless, J. M. Finder, C. D. Overgaard, R. Droopad, K. W. Eisenbeiser, J. A. Hallmark, W. J. Ooms, J. R. Conner, and V. S. Kaushik, *J. Vac. Sci. Technol. B* **18**, 1653 (2008).
- <sup>49</sup>M. D. McDaniel, A. Posadas, T. Wang, A. A. Demkov, and J. G. Ekerdt, *Thin Solid Films* **520**, 6525 (2012).
- <sup>50</sup>M. Choi, A. Posadas, R. Dargis, C.-K. Shih, A. A. Demkov, D. H. Triyoso, N. D. Theodore, C. Dubourdieu, J. Bruley, and J. Jordan-Sweet, *J. Appl. Phys.* **111**, 064112 (2012).
- <sup>51</sup>M. D. McDaniel, A. Posadas, T. Q. Ngo, A. Dhamdhare, D. J. Smith, A. A. Demkov, and J. G. Ekerdt, *J. Vac. Sci. Technol. A* **31**, 01A136 (2013).
- <sup>52</sup>M. D. McDaniel, A. Posadas, T. Q. Ngo, A. Dhamdhare, D. J. Smith, A. A. Demkov, and J. G. Ekerdt, *J. Vac. Sci. Technol. B* **30**, 04E111 (2012).
- <sup>53</sup>G. Kresse and J. Furthmüller, *Phys. Rev. B* **54**, 11169 (1996).
- <sup>54</sup>J. P. Perdew and A. Zunger, *Phys. Rev. B* **23**, 5048 (1981).
- <sup>55</sup>P. E. Blöchl, *Phys. Rev. B* **50**, 17953 (1994).
- <sup>56</sup>S. L. Dudarev, G. A. Botton, S. Y. Savrasov, C. J. Humphreys, and A. P. Sutton, *Phys. Rev. B* **57**, 1505 (1998).

- <sup>57</sup>C. Rödl, F. Fuchs, J. Furthmüller, and F. Bechstedt, *Phys. Rev. B* **79**, 235114 (2009).
- <sup>58</sup>S. C. Petitto, E. M. Marsh, G. A. Carson, M. Langell, and J. Mole. *Catal. A Chem.* **281**, 49 (2008).
- <sup>59</sup>T. J. Chuang, C. R. Brundle, and D. W. Rice, *Surf. Sci.* **59**, 413 (1976).
- <sup>60</sup>S. A. Chambers, Y. Liang, Z. Yu, R. Droopad, J. Ramdani, and K. Eissenbeiser, *Appl. Phys. Lett.* **77**, 1662 (2000).
- <sup>61</sup>L. F. Edge, D. G. Schlom, S. A. Chambers, E. Cicerrella, J. L. Freeouf, B. Holländer, and J. Schubert, *Appl. Phys. Lett.* **84**, 726 (2004).
- <sup>62</sup>S. A. Chambers, M. H. Engelhard, V. Shutthanandan, Z. Zhu, T. C. Droubay, L. Qiao, P. V. Sushko, T. Feng, H. D. Lee, T. Gustafsson, E. Garfunkel, and A. B. Shah, *Surf. Sci. Rep.* **65**, 317 (2010).
- <sup>63</sup>H. Seo, A. Posadas, C. Mitra, A. V. Kvit, J. Ramdani, and A. A. Demkov, *Phys. Rev. B* **86**, 075301 (2012).
- <sup>64</sup>S. A. Chambers, Y. Liang, Z. J. Zu, R. Droopad, J. Ramdani, and K. Eisenbeiser, *J. Vac. Sci. Technol. A* **19**, 934 (2001).

## **Chapter 7: Atomic layer deposition of CoO on SrTiO<sub>3</sub>-buffered Si(001), SiO<sub>2</sub>/Si, and MgO(001) substrates and methods to form thin magnetic Co metal films**

### **7.1. INTRODUCTION**

Cobalt oxides have a wide range of applications, such as optical sensors, magnetic detectors, catalytic membranes, photocatalysis, and batteries, etc.<sup>1-6</sup> Thin films of cobalt oxides have been grown on different substrates exhibiting a variety of properties.<sup>1-6</sup> Cobalt (II) oxide has a band gap of 2.4 eV, which has been used for visible light driven for photoelectrochemical water oxidation.<sup>5</sup> Cobalt spinel, Co<sub>3</sub>O<sub>4</sub>, a semiconductor with a band gap of 1.6 eV has been used for sensing, spintronics, and catalysis applications.<sup>1,3,6,7</sup> The growth of CoO and Co<sub>3</sub>O<sub>4</sub> have been performed using different growth techniques, such as molecular beam epitaxy (MBE),<sup>8-10</sup> pulsed laser deposition,<sup>11,12</sup> chemical vapor deposition (CVD),<sup>13-15</sup> and atomic layer deposition (ALD).<sup>5,16-18</sup> Among them, ALD offers great film uniformity and conformality over large substrates, which are desired for most of applications. There have been a number of reports on the growth and characterization of cobalt oxides using ALD.<sup>5,16-20</sup>

Compared to cobalt oxides, cobalt metal is a widely-studied material for microelectronic and memory applications. Co is well-known to have a good adhesion on the Cu surface, Co and Co alloys thin films have been studied as a capping layer material in the back end of line (BEOL) interconnects as a Cu electromigration barrier.<sup>21-24</sup> Attempts to deposit Co metal on SiO<sub>2</sub>, carbon-doped oxide, and Cu has been reported by ALD using bis(N-tert butyl, N'-ethylpropionamidinato) cobalt (II) and H<sub>2</sub>. The levels of C and N incorporation into the resultant cobalt thin film becomes problematic when it is used for BEOL interconnect applications.<sup>25,26</sup>

Recently, Co and Co alloys, such as CoFe and CoFeB have been proposed as potential magnetic materials for the magnetic tunneling junction (MTJ).<sup>27-32</sup> A basic MTJ is composed of two ferromagnetic layers (known as the fixed and free layers) separated by an ultra-thin insulating tunneling barrier. While magnetic moment orientation of fixed layer remains unchanged, the magnetic moment orientation of free layer can be switched during device-functioning. Crystallographic structure, particle size, and texture deeply effect magnetic properties, such as anisotropy, coercivity, and the magnetization reversal process. Therefore, the study of magnetic behavior of Co and Co alloys has attracted considerable attention.<sup>33-35</sup> Co metal can be used as either the fixed or free layer depending on its structure and particle size.<sup>33-38</sup> The deposition of Co and Co alloys thin films has been performed by both physical vapor deposition<sup>30-37</sup> and CVD<sup>38</sup> techniques. However, with down-scaling feature sizes of electronic devices thin film uniformity and conformality become very important. As such, ALD is a very attractive technique for magnetic films deposition. The advantages of ALD are precise thickness control at the Ångstrom level because the precursors will adsorb and subsequently desorb from the surface areas where reaction has reached completion to form a monolayer.<sup>39</sup> The self-limiting behavior of ALD also produces very smooth and conformal films to the underlying substrates.

More recently, the spin-transfer torque random-access memory (STT-RAM) structure has been proposed.<sup>40-43</sup> A basic STT-RAM cell is composed of a transistor, an MTJ, a word line (WL), a bit line (BL), and a source line as shown in Figure 7.1a. STT-RAM is currently being developed by Everspin, Grandis, Hynix, IBM, Samsung, TDK, and Toshiba. Figure 7.1b shows a schematic of a STT-RAM cell structure proposed by NASCENT. There are many challenges in forming a memory element and in connecting the elements electrically along the close-spaced word line (WL) direction and ultimately

in the transverse bit line (BL) direction with a magnetic material. Our study is to explore chemical routes to the growth of Co thin films in the desired BL direction without the need for subsequent etching to remove excess or undesired material because there will be difficult to align etch masks once the WLs are formed. Then selective area deposition becomes one of critical steps for the STT-RAM fabrication. This makes ALD an ideal technique for fabricating the STT-RAM device.

Since ALD film growth necessarily involves a film nucleation step, it is possible to engineer the surface energy of the substrate to cause preferential wetting and nucleation in only desired areas, resulting in area selective ALD. Unlike conventional photolithography-based fabrication, such a bottom-up patterning approach could eliminate the need for subsequent etch steps, reducing the cost of fabrication and overcoming down-scaling limitations in manufacturing devices. This project explored the first steps toward a sufficiently conductive and magnetic bit line.

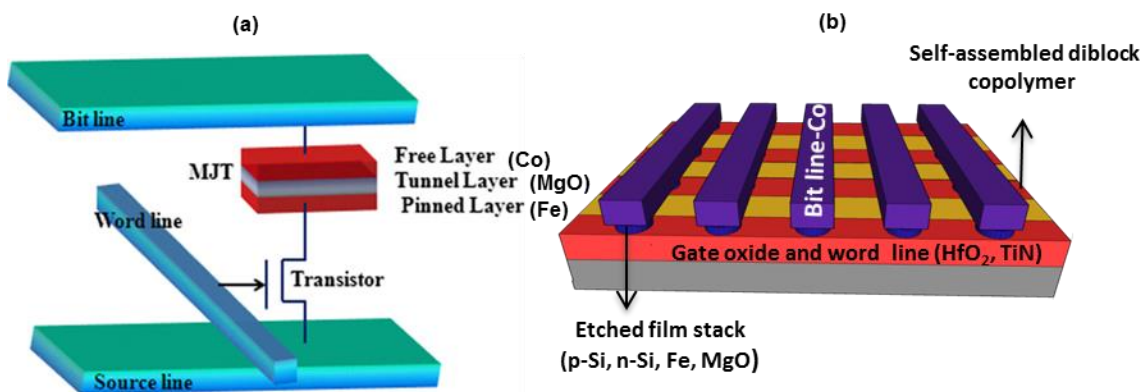


Figure 7.1: (a) Basic STT-RAM cell structure (Adapted from Ref. 43), (b) A schematic of STT-RAM structure proposed by NASCENT.

In Chapter 6 I explored the growth of CoO as a thin film for photocatalytic water splitting.<sup>5</sup> CoO films were grown on four unit cell MBE-grown SrTiO<sub>3</sub> using cobalt bis(diisopropylamidinate) and water. During CoO growth, the Co precursor and water

were held at 56 and 26 °C, respectively, while the substrate was maintained at a temperature range of 170–180 °C. This low temperature is used to minimize the potential reaction between CoO and Si due to the oxygen diffusion through four unit cell SrTiO<sub>3</sub>. Attempts to deposit CoO films at higher ALD temperatures resulted in some reduced Co species.<sup>5</sup>

In this study, we report the deposition of CoO on SrTiO<sub>3</sub>-buffered Si(001), SiO<sub>2</sub>/Si, and single crystal MgO(001) substrates at a temperature range of 170–270 °C by ALD using bis(N-tert butyl, N'-ethylpropionamidinato) cobalt (II) and water as co-reactants. Growth at temperatures above 305 °C results in C-incorporated Co films. *In situ* x-ray photoelectron spectroscopy (XPS) is used to determine the oxidation state of cobalt and film stoichiometry. Reflection high energy electron diffraction (RHEED) is used to determine crystallinity and film structure. While the CoO thin films grown on SiO<sub>2</sub>/Si are polycrystalline, the CoO thin films grown on SrTiO<sub>3</sub>-buffered Si(001) and single crystal MgO(001) substrates are crystalline and epitaxial. Our study also shows that poly(trimethylsilylstyrene) deposited on MgO by spin-coating inhibits the nucleation of CoO. This suggests an area selective deposition of CoO may be possible for fabricating the STT-RAM structure. The transformation of CoO to Co<sub>3</sub>O<sub>4</sub> is also presented in this report. We demonstrate the reduction of CoO forming carbon-free Co metal by using Al and Sr metals to scavenge oxygen from CoO. Scanning superconducting quantum interference device (SQUID) is used to determine the magnetization and magnetic coercivity of the resultant cobalt thin films.

## 7.2. EXPERIMENTAL

Four-inch wafers of SiO<sub>2</sub>/Si were prepared by a thermal oxidation method. The 0.5 mm-thick wafers were then cut into 20 × 20 mm<sup>2</sup> pieces. MgO (001) substrates 10 mm × 10 mm × 0.5 mm are commercially available from MTI corporation. The substrates were ultrasonically cleaned with acetone, isopropyl alcohol, and deionized water for 5 min each, followed by UV/ozone treatment for 15 min to remove residual carbon contamination. The substrates were loaded into the system and vacuum annealed at a temperature of 650 °C and pressures lower than 1×10<sup>-8</sup> Torr for 30 min. The SrTiO<sub>3</sub>-buffered Si(001) substrates were prepared by MBE.<sup>44</sup> The substrates were then *in-situ* transferred to the ALD chamber for CoO deposition. The ALD system is a custom-built, hot-wall stainless steel rectangular 20-cm long chamber, with a reactor volume of 460 cm<sup>3</sup>. Ultrahigh purity argon was used as a purge/carrier gas. The substrate temperature was monitored with a reference thermocouple in the ALD chamber that was previously calibrated against an instrumented wafer.

Bis(N-tert butyl, N'-ethylpropionamidinato) cobalt (II) and water were used as co-reactants for the ALD growth. During CoO growth, the Co precursor and water were held at 80 °C and room temperature (26 °C), respectively, while the substrate was maintained at a temperature range of 170–270 °C. The water dosing was regulated using an in-line needle valve. Each cycle of CoO growth consisted of a 2 sec dose of Co, a 10 sec purge of Ar, a 2 sec dose of H<sub>2</sub>O, and a 10 sec purge of Ar. The deposition of Sr and Al metals was performed in a customized DCA 600 MBE system with a base pressure of 5×10<sup>-9</sup> Torr.<sup>44</sup>

X-ray reflectivity (XRR) was used to determine the CoO film thicknesses and growth rate. The growth rate of CoO was found to be 0.03 nm/cycle on SrTiO<sub>3</sub>-buffered Si(001), SiO<sub>2</sub>/Si and MgO(001) substrates. The CoO film crystallinity and orientation

were determined by RHEED. XRR was conducted by a Panalytical X'PERT Pro diffractometer using a sealed tube Cu K $\alpha$  radiation source ( $\lambda \sim 1.5406 \text{ \AA}$ ) operating at 40 kV and 30 mA. RHEED was performed using a Staib Instruments RHEED gun operated at 18 keV energy and 3 $^\circ$  grazing incidence. The *in-situ* VG Scienta R3000 XPS system with a monochromated Al K $\alpha$  source at 1486.6 eV was used to determine film stoichiometry and composition, and the oxidation states of cobalt. The absolute energy scale of the analyzer of the XPS system is calibrated using a two-point measurement such that the Ag 3d $_{5/2}$  core level is at 368.26 eV and the Fermi edge of Ag is at 0.0 eV.

### 7.3. RESULTS AND DISCUSSION

#### 7.3.1. Growth of CoO on amorphous SiO $_2$ /Si and single crystal MgO(001) substrates

Figure 7.2a shows the Co 2p x-ray photoelectron (XP) spectra of 3-nm-thick CoO films grown on SiO $_2$  (red color) and on MgO(001) (blue color) at a temperature of 180  $^\circ$ C. All XPS peak positions were shifted by taking the CoO O 1s elemental peak to be at 530 eV. The binding energies of the main peaks are at 780.5 eV and 796.5 eV for Co 2p $_{3/2}$  and Co 2p $_{1/2}$  levels, respectively, and at 786.4 eV and 803.0 eV for the Co 2p $_{3/2}$  and Co 2p $_{1/2}$  for satellite peaks, respectively. The 2p binding energy position in conjunction with the very strong satellite at  $\sim 6$  eV higher binding energy is consistent with Co being in the +2 valence state with high spin.<sup>45</sup> Figures 7.2b and 7.2c show RHEED images of CoO thin films grown on SiO $_2$  and MgO(001) substrates, respectively. The centered-ring patterns (as shown in Fig. 7.2b) indicate that the CoO thin films grown on SiO $_2$  have polycrystalline microstructure. The RHEED images in Fig. 7.2c show clear dotted streaks, which means that the CoO films grown on single crystal MgO(001) are epitaxial with the

underlying substrate and have some surface roughness. The growth rate of CoO was found to be  $\sim 0.3 \text{ \AA/cycle}$  on both  $\text{SiO}_2/\text{Si}$  and  $\text{MgO}(001)$  substrates.

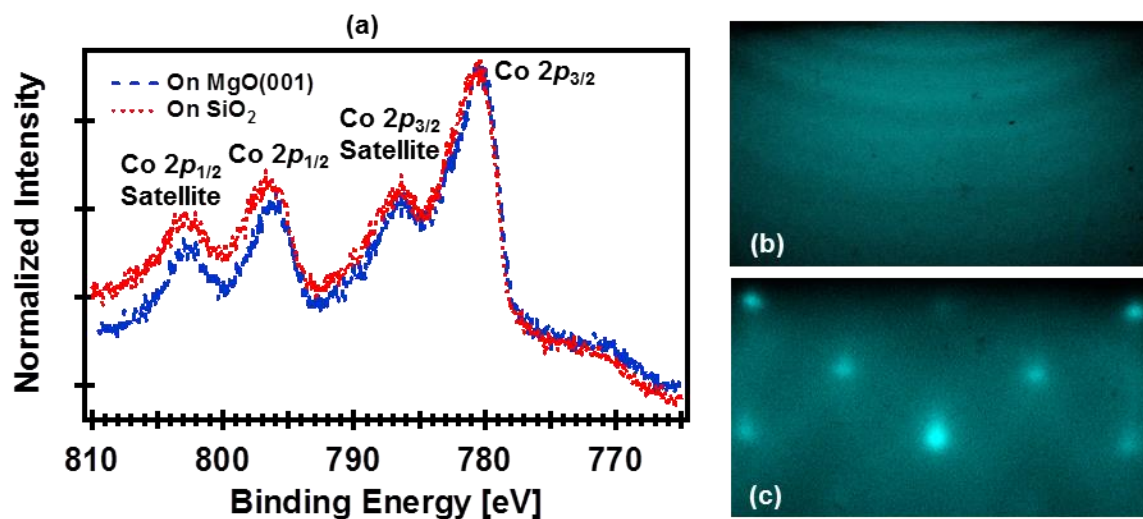


Figure 7.2: Co  $2p$  XP-spectra of 3-nm-thick CoO films on  $\text{SiO}_2/\text{Si}$  and  $\text{MgO}(001)$  substrates grown by ALD at  $\sim 180 \text{ }^\circ\text{C}$  [Fig. 7.2a (red color) and Fig. 7.2b (blue color), respectively]. RHEED images of a 3-nm-thick CoO film grown on  $\text{SiO}_2$  (Fig. 7.2b) and a 15-nm-thick CoO film grown on  $\text{MgO}(001)$  (Fig. 7.2c).

The formation of CoO films on four unit cell  $\text{SrTiO}_3$ -buffered  $\text{Si}(001)$  was observed in a temperature range of  $170\text{--}190 \text{ }^\circ\text{C}$  in our previous study.<sup>5</sup> The formation of CoO films on  $\text{MgO}(001)$  is observed in a wider temperature range of  $170\text{--}270 \text{ }^\circ\text{C}$  in this study. In the growth of CoO on  $\text{SrTiO}_3$ -buffered  $\text{Si}(001)$ , CoO reacts with Si due to the O diffusion through four unit cell of  $\text{SrTiO}_3$ , while there is no reaction between MgO and CoO in the CoO growth on  $\text{MgO}(001)$ . At temperatures higher than  $305 \text{ }^\circ\text{C}$ , cobalt metal formation was observed instead of CoO. We note the growth above  $270 \text{ }^\circ\text{C}$  may not be a true ALD process. Figure 7.3(a) displays Co  $2p$  XP-spectra of 200 cycles of CoO films grown at temperatures of  $270$  (black color),  $305$  (red color), and  $345 \text{ }^\circ\text{C}$  (blue color).

While the film grown at 270 °C still shows the presence of CoO, the films grown at 305 and 345 °C show the presence of Co metal. However, there is ~ 31 % of carbon incorporated into the 305 and 345 °C cobalt films as estimated using XPS (Fig. 7.4). The C 1s XPS intensity remains the same after a 15 min vacuum anneal at 500 °C (Fig. 7.4a). This is different from the residual C (<2%) detected on the surface of as-deposited CoO films, which disappears after a slight vacuum anneal. Carbon incorporation into Co films has also been reported using the same precursor (bis(N-tert butyl, N'-ethylpropionamidinato) cobalt (II)) and hydrogen as a reducing agent.<sup>25,26</sup> Figures 7.3b and 7.3c represent RHEED images of Co metal grown on MgO(001) substrate at 345 and 305 °C, respectively. The ring centered-patterns shown in Figs. 7.3b and 7.3c indicate that the thin Co films grown at 305 and 345 °C are polycrystalline on MgO(001). However, the spotty patterns are in well-ordered meaning that the Co films have a certain orientation preference.

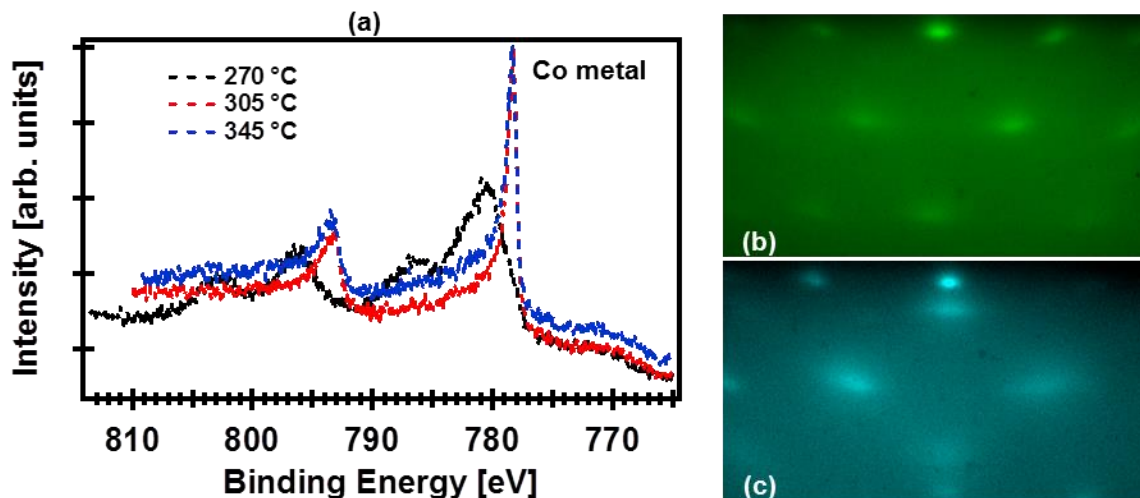


Figure 7.3: (a) Co 2p XP-spectra of 200 cycles of CoO films on single crystal MgO(001) substrates grown by ALD at ~ 270 (black color), 305 (red color), and 345 °C (blue color). (b) and (c) RHEED images of 200 cycles of CoO films on MgO(001) grown by ALD at 345 and 305 °C, respectively.

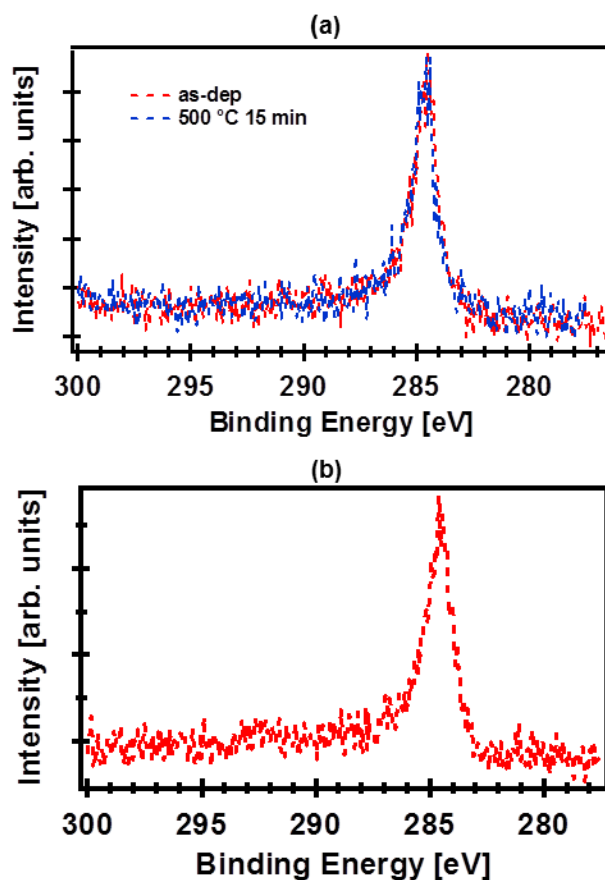


Figure 7.4: (a) C 1s XP-spectra of a 200 ALD cycles of CoO film on MgO(001) grown at 345 °C as-deposited (red color) and after a 15 min vacuum anneal at 500 °C (blue color). (b) C 1s XP-spectra of an as-deposited 200 ALD cycles of CoO film on MgO(001) grown at 305 °C.

In addition to the growth of CoO on SiO<sub>2</sub>/Si and MgO substrates, the deposition of CoO was explored on poly(trimethylsilylstyrene) at 180 °C using ALD was also performed in this study. A 50-nm-thick poly(trimethylsilylstyrene) was deposited (by the Willson group) on amorphous MgO/SiO<sub>2</sub>/Si by spin-coating. The sample was *ex-situ* transferred to the ALD chamber for the deposition of 300 cycles of CoO. There was no detectable Co 2p or O 1s XP-spectra after 300 ALD cycles of CoO (Fig. 7.5). This indicates that poly(trimethylsilylstyrene) inhibits the nucleation of CoO. The result could

enable the selective area ALD of CoO on STT-RAM structure at mild conditions in future work.

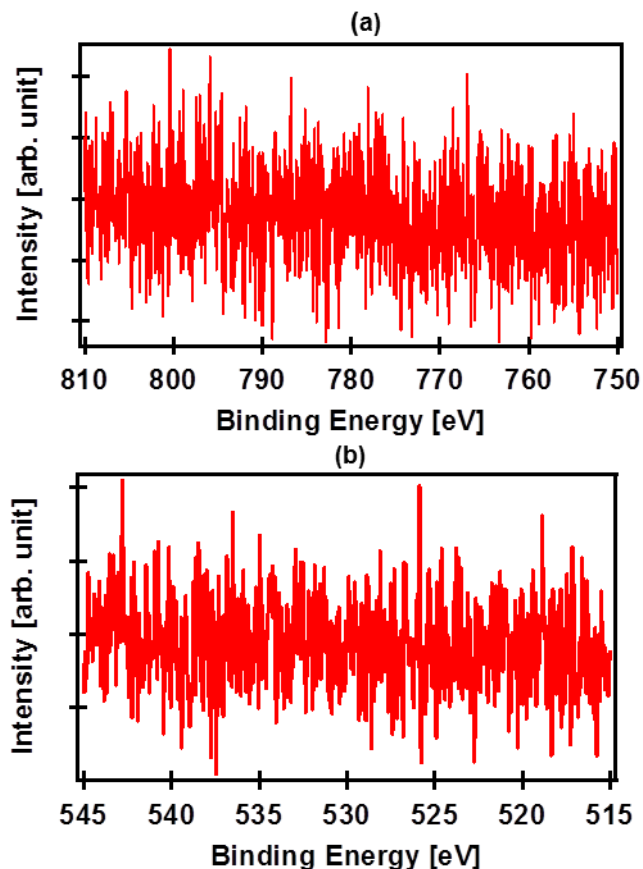


Figure 7.5: (a) Co 2*p* and (b) O 1*s* XP-spectra after 300 ALD cycles of CoO film on 50-nm-thick poly(trimethylsilylstyrene) on amorphous MgO/SiO<sub>2</sub>/Si.

### 7.3.2. Transformation of CoO to Co spinel, Co<sub>3</sub>O<sub>4</sub>

The CoO was found to oxidize to form Co<sub>3</sub>O<sub>4</sub> in air upon being exposed to mercury ultraviolet (Hg UV) light with a wavelength of ~ 200 nm for 30 min. The red color in Fig. 7.6a represents the Co 2*p* XP-spectra of a 4.5-nm-thick CoO film grown on MgO(001) substrate at 180 °C. The as-deposited CoO film was unloaded from the ultra-high vacuum and exposed to the Hg UV light for 30 min at room temperature. The film was reloaded into the analysis system. XPS and RHEED were used to re-characterize the

film after exposing it to the Hg UV light. Figure 7.6a shows Co 2*p* XP-spectra of the film before (red color) and after exposing it to the Hg UV light (blue color). Co 2*p* XP-spectrum shows characteristic strongly suppressed shake-up satellite peaks at 786.4 eV and 803.0 eV as compared to CoO.<sup>46</sup> Figure 7.6b confirms the crystalline quality of the 4.5-nm-thick CoO film grown on MgO(001) with bright streaks along with clear Kikuchi lines. After exposing the CoO film to Hg UV light, extra streaks appear in between the original CoO streaks (Fig. 7.6c) indicating the in-plane lattice constant of new cobalt oxide structure is twice as the CoO in-plane lattice constant. This is consistent with the Co spinel XPS data and consistent with the lattice constant of both CoO and Co<sub>3</sub>O<sub>4</sub>.<sup>47,48</sup> The formation of epitaxial Co<sub>3</sub>O<sub>4</sub> from epitaxial CoO films should motivate further studies on Co<sub>3</sub>O<sub>4</sub> for magnetic and catalytic applications.

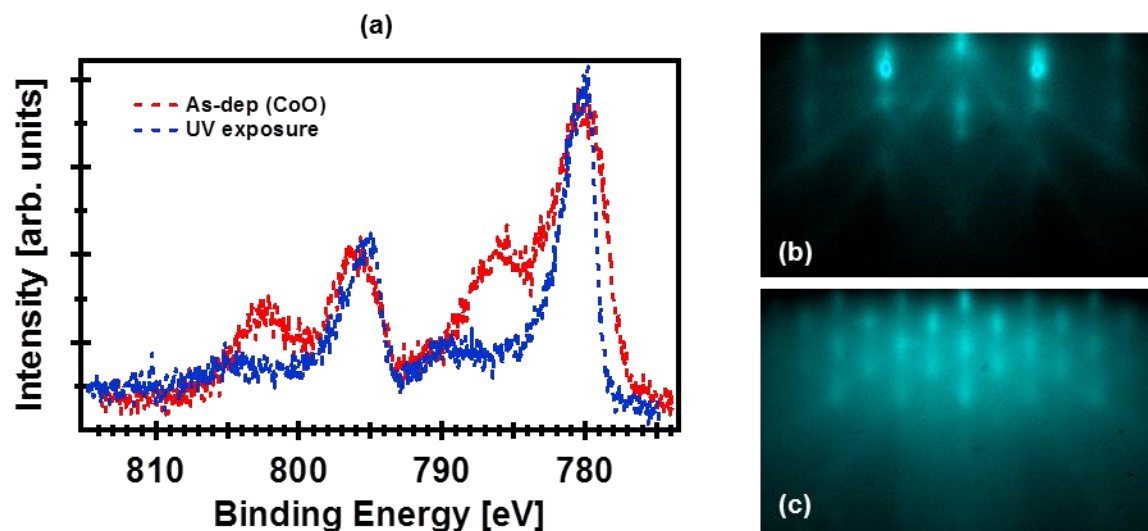


Figure 7.6: (a) Co 2*p* XP-spectra of a 4.5-nm-thick as-deposited CoO film on MgO(001) substrate grown by ALD at 180 °C (red color) and the CoO film after exposing to Hg UV light for 30 min at room temperature (blue color). The Co 2*p* XP-spectrum shows characteristic strongly suppressed shake-up satellite peaks at 6 eV and +22 eV as compared to CoO indicating the formation of Co<sub>3</sub>O<sub>4</sub>. (b) and (c) are RHEED images of the as-deposited CoO and after exposing to Hg UV light for 30 min at room temperature, respectively.

### 7.3.3. Transformation of CoO to Co metal and magnetization of Co films

Our previous study<sup>5</sup> showed that CoO films grow epitaxially on SrTiO<sub>3</sub>-buffered Si(001) at a temperatures from 170–190 °C using ALD. The as-deposited CoO films have some residual carbon contamination (<2%), which disappears after a slight vacuum anneal. During the vacuum anneal, the heterostructure CoO/SrTiO<sub>3</sub> (1.6 nm)/Si also produced Co metal species due to the reaction between CoO and Si. We surmised oxygen diffuses through 1.6 nm SrTiO<sub>3</sub> and reacts with Si to form Co and SiO<sub>x</sub>.<sup>5</sup> Figure 7.7a shows Co 2*p* XP-spectra of a 4-nm-thick CoO film grown on four unit cell SrTiO<sub>3</sub>-buffered Si(001) as-deposited (red color), after a 30 min vacuum anneal at 500 °C (green color), and after an additional 30 min vacuum anneal at 550 °C (black color). The formation of Co metal after the vacuum anneals was observed by the appearance of the Co 2*p* metal peaks at ~ 778 eV. Figures 7.7b and 7.7c show Si 2*p* and O 1*s* XP-spectra, respectively, of the same CoO film as-deposited and throughout the annealing process. Significant increases in the Si 2*p* oxide peak at the binding energy of ~ 103.5 eV and the appearance of another O 1*s* peak at the binding energy of 533 eV after the vacuum anneals are consistent with the appearance of Co metal peak. These demonstrate the reaction between Si, which is acting as a strong oxygen-gettering substrate, and CoO to form SiO<sub>x</sub> and Co metal.

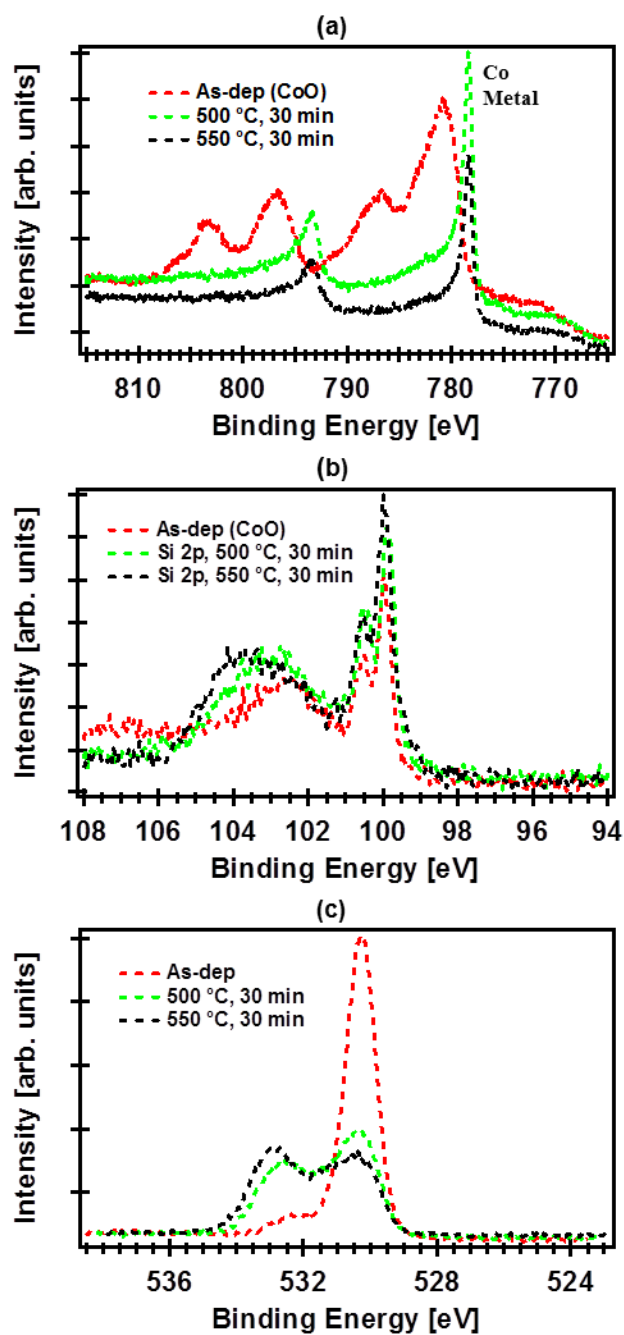


Figure 7.7: (a) Co 2p, (b) Si 2p, and (c) O 1s XP-spectra of a 4-nm-thick CoO film grown on four unit cell SrTiO<sub>3</sub>-buffered Si(001) as-deposited (red color), after a 30 min vacuum anneal at 500 °C (green color), and after an additional 30 min vacuum anneal at 550 °C (black color).

To better understand the reaction between Si and CoO, thicker SrTiO<sub>3</sub> (~ 15 nm) on Si(001) was grown by MBE. Another 4-nm-thick CoO film was grown by ALD on top of it. The CoO/SrTiO<sub>3</sub>(~15 nm)/Si(001) heterostructure was *in vacuo* transferred to an annealing chamber. After 30 min vacuum anneal at 500 °C, there was a very small feature of Co metal in the Co 2*p* XP-spectrum. An additional 90 min vacuum anneal at 600 °C was performed on the heterostructure and Co 2*p* XP-spectrum remain unchanged (Fig. 7.8a). The small increase in the O 1*s* XP-spectra as shown in Fig. 7.8b after vacuum anneals is consistent with the appearance of the small feature of Co metal. The results suggest that a ~ 15-nm-thick SrTiO<sub>3</sub> is a good O diffusion barrier. This study demonstrates that CoO is thermally unstable only if there is a sink that is readily available for the O.

Based on this observation, we develop a chemical method to form C-free Co films by reducing ALD-grown CoO films. We cap the CoO with metals that have a high affinity for oxidation, such as Al and Sr, and will form a capping oxide on the Co storage layer.

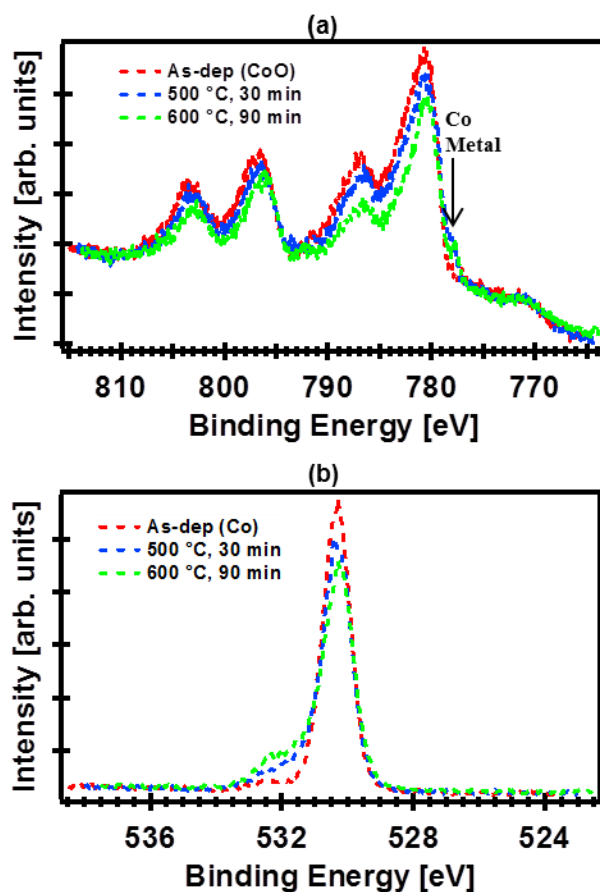


Figure 7.8: (a) Co  $2p$  and (b) O  $1s$  XP-spectra of a 4-nm-thick CoO film grown on  $\sim 15$ -nm-thick SrTiO<sub>3</sub>-buffered Si(001) as-deposited (red color), after a 30 min vacuum anneal at 500 °C (green color), and after an additional 30 min vacuum anneal at 550 °C (black color).

Figure 7.9a shows Co  $2p$  XP-spectrum of an as-deposited 3-nm-thick CoO grown on SiO<sub>2</sub> substrate by ALD at 180 °C (red color). The as-deposited film was transferred *in vacuo* to the annealing chamber and vacuum-annealed at 500 °C for 30 min. Co  $2p$  XP-spectrum of the CoO film after vacuum-annealing (blue color) is roughly coincident with that of as-deposited CoO film, indicating that CoO/SiO<sub>2</sub> is thermally stable in vacuum at 500 °C and is consistent with the preceding results. The sample was then *in-situ* transferred to the MBE chamber where a 3-nm-thick of Sr metal was deposited on it at

the substrate temperature of 200 °C. Co 2*p* XP-spectrum (green color) shows the appearance of Co metal species at the binding energy of 778 eV. This suggests that the Sr reacts with CoO to form SrO and Co. The heterostructure was vacuum-annealed at 500 °C for 30 min. Only the Co metal peak with higher intensity for the Co 2*p* XP-spectrum (black color) is observed meaning that more Sr reacts with CoO forming more SrO and Co. At 500 °C, SrO starts evaporating<sup>41,42</sup> and that is why the intensity of Co 2*p* peak becomes higher after the vacuum anneal. The reaction between Sr and CoO is also demonstrated by the Sr 3*d* XP-spectra as shown in Fig. 7.9b. The broad Sr peak [Fig. 7.9b (green color)] of the as-deposited Sr on CoO/SiO<sub>2</sub>/Si indicates the presence of a mixture of Sr and SrO. After the vacuum anneal, the Sr 3*d* XPS peak becomes narrower and appears at the binding energy at ~ 134 eV for Sr 3*d*<sub>5/2</sub> indicating more SrO formed via the reaction between Sr and CoO. This demonstrates a method to reduce CoO forming Co using Sr as an oxygen scavenger. The SrO formed could then be removed by annealing the heterostructure in vacuum at high temperature.<sup>49,50</sup>

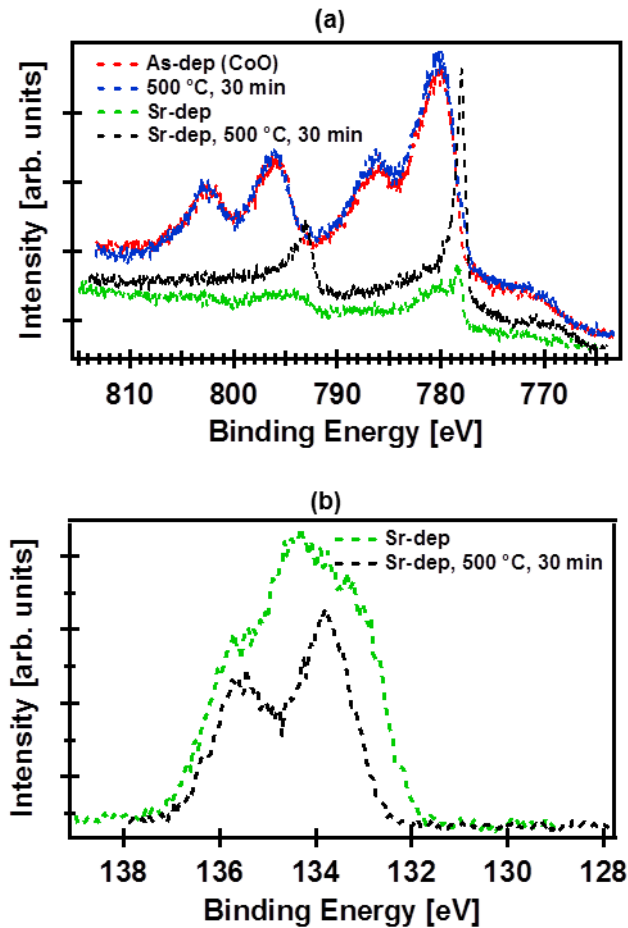


Figure 7.9: (a) Co  $2p$  XP-spectra of: an as-deposited 3-nm-thick CoO film on SiO<sub>2</sub> grown by ALD at 180 °C (red color), the CoO film after a 30 min vacuum anneal at 500 °C (blue color), the CoO film after a deposition of 3-nm-thick Sr on it (green color), and the Sr/CoO/SiO<sub>2</sub>/Si heterostructure after a 30 min vacuum anneal at 500 °C. (b) Sr  $3d$  XP-spectra of the Sr/CoO/SiO<sub>2</sub>/Si heterostructure as-deposited (green color) and after a 30 min vacuum anneal at 500 °C (black color).

Likewise, Al metal can be used as another scavenger to reduce CoO forming Co. Figure 7.10a again represents the Co  $2p$  XP-spectra of a 3-nm-thick CoO on SiO<sub>2</sub> grown by ALD at 180 °C. A 3-nm-thick Al metal was deposited on it at 200 °C using MBE. The blue color in Fig. 7.10a shows that Co formation is observed after the deposition of Al metal. The result demonstrates that Al reacts with CoO at a temperature of 200 °C. A 30

min vacuum anneal at 500 °C is also performed for the heterostructure. The green color in Fig. 7.10a is roughly coincident with the blue color, which means that majority of CoO reacts with Al before the vacuum anneal. This is also confirmed by the Al 2*p* XPS-spectra in Fig. 7.10b. The small feature at a binding energy of ~ 73 eV is for Al metal, while the bigger feature at a binding energy of 75.5 eV is for Al<sub>2</sub>O<sub>3</sub>.<sup>51</sup> After the vacuum anneal, there is more Al<sub>2</sub>O<sub>3</sub> and less Al metal formed in the heterostructures. Unlike SrO, Al<sub>2</sub>O<sub>3</sub> is very stable. For some applications, the presence of Al<sub>2</sub>O<sub>3</sub> may be undesired and the use of Sr might be preferred.

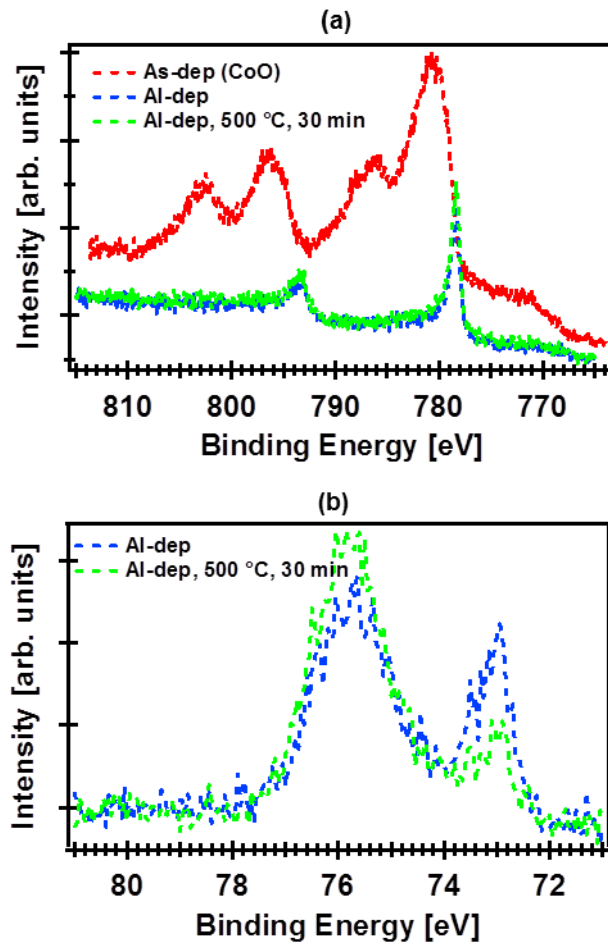


Figure 7.10: (a) Co  $2p$  XP-spectra of: an as-deposited 3-nm-thick CoO film on SiO<sub>2</sub> grown by ALD at 180 °C (red color), after a deposition of 3-nm-thick Sr on the CoO/SiO<sub>2</sub> (blue color), and the Sr/CoO/SiO<sub>2</sub>/Si heterostructure after a 30 min vacuum anneal at 500 °C. (b) Al  $2p$  XP-spectra of the Al/CoO/SiO<sub>2</sub>/Si heterostructure as-deposited (blue color) and after a 30 min vacuum anneal at 500 °C (green color).

Magnetic properties of the Co metal films were measured using a Quantum Design SQUID magnetometer. The magnetization as a function of applied magnetic field was measured at 300K. Figure 7.11 shows the magnetization for both SrO/Co/SiO<sub>2</sub>/Si and Al<sub>2</sub>O<sub>3</sub>/Co/SiO<sub>2</sub>/Si heterostructures at room temperature. The hysteresis loops of

magnetization are observed with the direction of applied magnetic field showing ferromagnetic behavior at room temperature for both heterostructures. Interestingly, a magnetic coercivity for the SrO/Co/SiO<sub>2</sub>/Si heterostructure was found to be ~ 250 Oe (Fig. 7.11a), while the one for Al<sub>2</sub>O<sub>3</sub>/Co/SiO<sub>2</sub>/Si was found to be ~ 30 Oe (Fig. 7.11b), which is 8–9 times lower. Further study is on-going into what leads to the different coercivity between the two heterostructures.

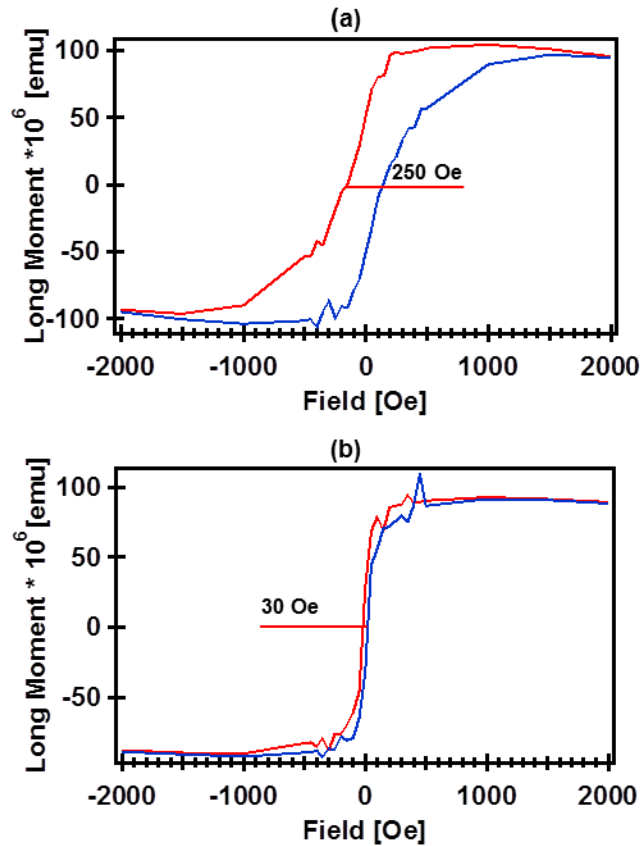


Figure 7.11: Magnetization of: (a) SrO/Co/SiO<sub>2</sub>/Si and Al<sub>2</sub>O<sub>3</sub>/Co/SiO<sub>2</sub>/Si heterostructures as a function of applied magnetic field measure at 300K. The sample size of 10×5×0.5 mm<sup>3</sup> was used for the measurement. The applied magnetic field was parallel to the substrates.

The use of Sr metal as a O scavenger is also explored for the epitaxial heterostructure CoO/MgO(001). Figure 7.12 presents the Co 2p XP-spectra of CoO films

with different thicknesses (3 and 15 nm) grown on MgO(001) as-deposited (red color), after a 3-nm-thick Sr deposition (blue color), and after a 30 min vacuum anneal at 500 °C of heterostructures (green color). The deposition of Sr metal was also performed in the MBE chamber at a substrate temperature of 200 °C. As shown by blue color on both Figs. (Figs. 7.12a and 7.12b), the reaction between Sr and CoO is observed as the Sr layer deposited on CoO at 200 °C (indicated by the appearance of a peak at a binding energy of  $\sim 778$  eV in the Co  $2p$  XPS). Figure 7.12a shows a complete reduction of 3-nm CoO to SrO/Co/MgO (green color) after the vacuum anneal, while Fig. 7.12b shows an incomplete reduction of 15-nm CoO to SrO/Co/CoO/MgO (green color) after the vacuum anneal. Figure 7.13 displays the magnetization of the two heterostructures as a function of magnetic field applied. The SrO/Co/MgO shows the coercivity of  $\sim 250$  Oe, which is consistent with the Co formed on SiO<sub>2</sub> as discussed above. However, the SrO/Co/CoO/MgO shows the coercivity of  $\sim 1,000$  Oe. The presence of CoO layer or differences of Co microstructure may effect the coercivity is under current investigation.

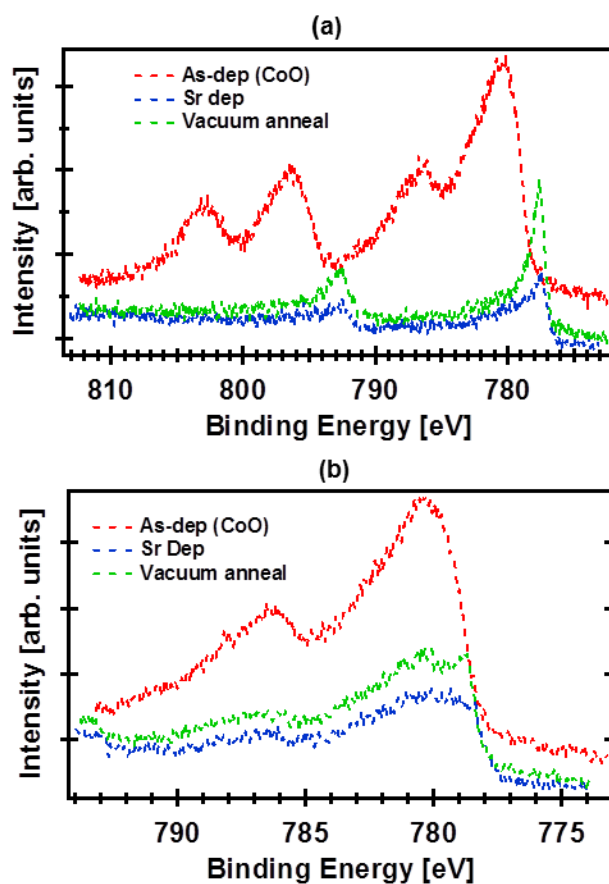


Figure 7.12: (a) Co 2p XP-spectra of: a 3-nm-thick CoO on MgO(001) grown by ALD at 180 °C (red color), after a deposition of a 3-nm-thick Sr on top of the 3-nm CoO (blue color), and after a 30 min vacuum anneal of the Sr/CoO/MgO(001) heterostructures at 500 °C. (b) Co 2p XP-spectra of: a 15-nm-thick CoO on MgO(001) grown by ALD at 180 °C (red color), after a deposition of a 3-nm-thick Sr on top of the 15-nm CoO (blue color), and after a 30 min vacuum anneal of the Sr/CoO/MgO(001) heterostructures at 500 °C.

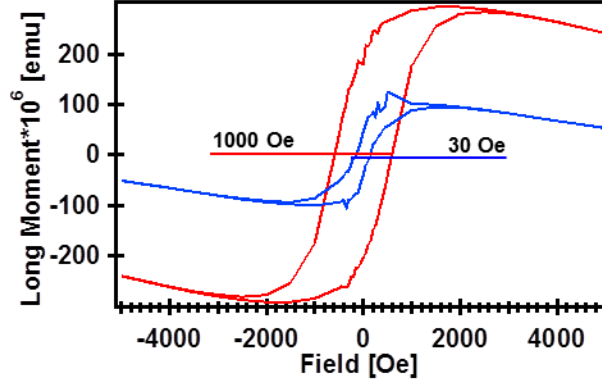


Figure 7.13: Magnetization of: SrO/Co/MgO(001) (blue color), and SrO/Co/CoO/MgO(001) (red color) heterostructures as a function of applied magnetic field measured at 300K. The sample size of  $10 \times 5 \times 0.5 \text{ mm}^3$  was used for the measurement. The magnetic field was applied parallel to the substrates.

#### 7.4. SUMMARY

We show the growth of CoO on SiO<sub>2</sub>/Si and MgO(001) substrates by ALD in a temperature range of 170–270 °C. While the CoO films grown on SiO<sub>2</sub>/Si are polycrystalline, the CoO films grown on single crystal substrate MgO(001) are crystalline and epitaxial. Attempts to grow CoO at temperatures higher than 305 °C result in ~ 31 % C-incorporated Co films. The transformation of CoO to spinel Co<sub>3</sub>O<sub>4</sub> is observed by exposing CoO films to Hg UV light at room temperature for 30 min. We demonstrate the reduction of CoO forming carbon-free Co metal using Al and Sr metals to scavenge oxygen from CoO. The room temperature ferromagnetic behavior of the resultant Co films is observed. However, further studies are needed to explore the change in coercivity of the Co films and the ability to control it. We will also perform further study on the reduction of CoO by thermal reducing in the presence of carbon monoxide and hydrogen.

## 7.5. REFERENCES

- <sup>1</sup>W. Y. Li, L. N. Xu, and J. Chen, *Adv. Func. Mater.* **5**, 851–857 (2005).
- <sup>2</sup>X.-Y. Yu, Q.-Q. Meng, T. Luo, Y. Jia, B. Sun, Q.-X. Li, J.-H. Liu, and X.-J. Huang, *Scientific Reports* **3**, 2886 (2013).
- <sup>3</sup>C. Hou, Q. Xu, L. Yin, and X. Hu, *Analyst*, **137**, 5803–5808 (2012).
- <sup>4</sup>G.A. Niklasson and C. G. Granqvist, *J. Mater. Chem.* **17**, 127 (2006).
- <sup>5</sup>T. Q. Ngo, A. Posadas, H. Seo, S. Hoang, M. D. McDaniel, D. Utes, D. H. Triyoso, C. B. Mullins, A. A. Demkov, and J. G. Ekerdt, *J. Appl. Phys.* **114**, 084901 (2013).
- <sup>6</sup>Y. Liang, Y. Li, H. Wang, J. Zhou, J. Wang, T. Regier, and H. Dai, *Nat. Mater.* **10**, 780–786 (2011).
- <sup>7</sup>M. M. Natile and A. Glisenti, *Chem. Mater.* **14** (7), 3090–3099 (2002).
- <sup>8</sup>K. J. Kormondy, A. B. Posadas, A. Slepko, A. Dhamdhere, D. J. Smith, K. N. Mitchell, T. I. Willett-Gies, S. Zollner, L. G. Marshall, J. Zhou, and A. A. Demkov, *J. Appl. Phys.* **115**, 243708 (2014).
- <sup>9</sup>C. A. F. Vaz, H.-Q. Wang, C. H. Ahn, V. E. Henrich, M. Z. Baykara, T. C. Schwendemann, N. Pilet, B. J. Albers, U. D. Schwarz, L. H. Zhang, Y. Zhu, J. Wang, and E. I. Altman, *Surf. Sci.* **603**, 291–297 (2009).
- <sup>10</sup>C. A. F. Vaz, E. I. Altman, and V. E. Henrich, *Phys. Rev. B* **81**, 104428 (2010).
- <sup>11</sup>L. Qiao, H. Y. Xiao, H. M. Meyer, J. N. Sun, C. M. Rouleau, A. A. Puretzky, D. B. Geohegan, I. N. Ivanov, M. Yoon, W. J. Webber, and M. D. Biegalski, *J. Mater. Chem. C*, **1**, 4628–4633 (2013).
- <sup>12</sup>R. J. Kennedy, *IEEE Trans. Magn.* **31**, 3829–3831 (1995).
- <sup>13</sup>K. Shalini, A. U. Mane, S. A. Shivashankar, M. Rajeswari, and S. Choopun, *J. Cryst. Growth* **231**, 242 (2001).

- <sup>14</sup>E. Fujii, H. Torii, A. Tomozawa, R. Takayama, and T. Hirao, *J. Mater. Sci.* **30**, 6013 (1995).
- <sup>15</sup>A. U. Mane, K. Shalini, and A. Wohlfart, *J. Cryst. Growth* **240**, 157 (2002).
- <sup>16</sup>K. B. Klepper, O. Nilsen, and H. Fjellvåg, *Thin Solid Films* **515**, 7772 (2007).
- <sup>17</sup>M. E. Donders, H. C. M. Knoop, M. C. M. Van, W. M. M. Kessels, and P. H. L. Notten, *J. Electrochem. Soc.* **158**, G92 (2011).
- <sup>18</sup>K. B. B. Klepper, O. Nilsen, and H. Fjellvåg, *J. Cryst. Growth* **307**, 457 (2007).
- <sup>19</sup>M. Diskus, O. Nilsen, and H. Fjellvåg, *Chem. Vap. Deposition* **17**, 135 (2011).
- <sup>20</sup>M. E. Donders, H. C. M. Knoop, M. C. M. Van de Sanden, W. M. M. Kessels, and P. H. L. Notten, *J. Electrochem. Soc.* **158**, G92 (2011).
- <sup>21</sup>A. Kohn, M. Eizenberg, and Y. Shacham-Diamand, *J. Appl. Phys.* **94**, 3015–3024 (2003).
- <sup>22</sup>P. Moon, V. Dubin, S. Johnston, J. Leu, K. Raol, and C. Wu, *IEEE Int. Electron Devices Meet.* 841 (2003).
- <sup>23</sup>R. G. Gordon, H. Kim, and H. Bhandari, *US Patent* 7, 973,789 B2, 2011.
- <sup>24</sup>O. Aibel, C. Hennesthal, M. Hauschildt, A. Beyer, J. Poppe, G. Talut, M. Gall, J. Hahn, J. Boemmels, M. Nopper, and R. Seidel, *IEEE*, 26–28 (2011).
- <sup>25</sup>T. D.-M. Elko-Hansen, A. Dolocan, and J. G. Ekerdt, *J. Phys. Chem. Lett.* **5**, 1091–1095 (2014).
- <sup>26</sup>T. D.-M. Elko-Hansen and J. G. Ekerdt, *Chem. Mater.* **26**, 2642–2646 (2014).
- <sup>27</sup>C. T. Horng and R.-Y. Tong, *US Patent*, US20130175644 A1 (2013).
- <sup>28</sup>C. T. Horng, R.-Y. Tong, C.-J. Torng, W. Kula, *US Patent*, US8372661 B2 (2013).
- <sup>29</sup>S. Yuasa and D. D. Djayaprawira, *J. Phys. D: Appl. Phys.* **40**, R337–R354 (2007).
- <sup>30</sup>S. Ikeda, K. Miura, H. Yamamoto, K. Mizunuma, H. G. Gan, M. Endo, S. Kanai, J. Hayakawa, F. Matsukura, and H. Ohno, *Nature Mater.* **9**, 721–724 (2010).

- <sup>31</sup>K.-M. Wu, K.-W. Cheng, C.-Y. Tsai, and C.-S. Tsai, US2014/0048893 A1(2012).
- <sup>32</sup>S. Parkin, X. Jiang, C. Kaiser, A. Panchula, K. Rochie, and M. Samant, *Proc. IEEE*, **91**, 661–680 (2003).
- <sup>33</sup>D. Schmidt, A. C. Kjerstad, T. Hofmann, R. Skomski, E. Schubert, and M. Schubert, *J. Appl. Phys.* **105**, 113508 (2009).
- <sup>34</sup>I. Bergenti, A. Riminucci, E. Arisi, M. Murgia, M. Cavallini, M. Solzi, F. Casoli, V. Dediu, *J. Magn. Magn. Mater.* **316**, e987–e989 (2007).
- <sup>35</sup>B. Presa, R. Matarranz, C. Clavero, J. M. García-Martín, J. F. Calleja, and M. C. Contreras, *J. Appl. Phys.* **102**, 053901 (2007).
- <sup>36</sup>C. G. Zimmermann, M. Yeadon, K. Nordlund, J. M. Gibson, R. S. Averback, U. Herr, and K. Samwer, *Phys. Rev. Lett.* **83**, 1163 (1999)
- <sup>37</sup>F. Tang, D.-L. Liu, D.-X. Ye, Y.-P. Zhao, T.-M. Lu, G.-C. Wang, and A. Vijayaraghavan, *J. Appl. Phys.* **93**, 4194 (2003).
- <sup>38</sup>N. Deo, M. F. Bain, J. H. Montgomery, H. S. Gamble, *J. Mater. Sci. Mater. Electron.* **16**, 387–392 (2005).
- <sup>39</sup>S. M. George, *Chem. Rev.* **110**, 111–131 (2010).
- <sup>40</sup>A. Driskill-Smith, D. Apalkov, V. Nikitin, X. Tang, S. Watts, D. Lottis, K. Moon, A. Khvalkovskiy, R. Kawakami, X. Luo, A. Ong, E. Chen, and M. Krounbi, *3<sup>rd</sup> IEEE International* 1–3, (2011).
- <sup>41</sup>U. Roy, T. Pramanik, M. Tsoi, L. F. Register, and S. Banerjee, *J. Appl. Phys.* **113**, 223904 (2013).
- <sup>42</sup>[http://www.flashmemorysummit.com/English/Collaterals/Proceedings/2009/20090813\\_ThursPlenary\\_Tabrizi.pdf](http://www.flashmemorysummit.com/English/Collaterals/Proceedings/2009/20090813_ThursPlenary_Tabrizi.pdf).
- <sup>43</sup>J. S. Meena, S. M. Sze, U. Chand, and T.-Y. Tseng, *Nanoscale Res. Lett.* **9**, 526 (2014).

- <sup>44</sup>M. Choi, A. Posadas, R. Dargis, C.-K. Shih, A. A. Demkov, D. H. Triyoso, N. D. Theodore, C. Dubourdieu, J. Bruley, and J. Jordan-Sweet, *J. Appl. Phys.* **111**, 064112 (2012).
- <sup>45</sup>T. J. Chuang, C. R. Brundle, and D. W. Rice, *Surf. Sci.* **59**, 413 (1976).
- <sup>46</sup>S. C. Petitto and M. A. Langell, *J. Vac. Sci. Technol. A* **22**, 1690 (2004).
- <sup>47</sup>T. Bredow and A. R. Gerson, *Phys. Rev. B* **61**, 5194–5201 (2000).
- <sup>48</sup>A. Walsh, S.-H. Wei, Y. Yan, M. M. Al-Jassim, J. A. Turner, M. Woodhouse, and B. A. Parkinson, *Phys. Rev. B* **76**, 165119 (2007).
- <sup>49</sup>L. V. Goncharova, D. G. Starodub, E. Garfunkel, T. Gustafsson, V. Vaithyanathan, J. Lettieri, D. G. Schlom, *J. Appl. Phys.* **100**, 014912 (2006).
- <sup>50</sup>Y. Wei, X. Hu, Y. Liang, D. C. Jordan, B. Crago, R. Droopad, Z. Yu, A. Demkov, J. L. Edwards Jr., and W. J. Ooms, *J. Vac. Sci. Technol. B* **20**, 1402 (2002).
- <sup>51</sup>S. Verdier, L. El Ouatani, R. Dedryvère, F. Bonhomme, P. Biensan, and D. Gonbeau, *J. Electrochem. Soc.* **154**, A1088–A1099 (2007).

## Chapter 8: Research Summary

### 8.1. CONCLUSION

Lanthanum aluminate (LAO) films were grown epitaxially on Si(001) by atomic layer deposition (ALD) using a buffer layer of strontium titanate (STO) grown by molecular beam epitaxy. The ALD growth of LAO was done at 250 °C by using tris(N,N'-diisopropylformamidinate)-lanthanum, trimethylaluminum, and water as co-reactants. Reflection high-energy electron diffraction, X-ray diffraction and transmission electron microscopy were used to determine film crystallinity. The as-deposited LAO films were amorphous and became crystalline after vacuum annealing at 600 °C for 2 h. *In-situ* X-ray photoelectron spectroscopy (XPS) was used to characterize the LAO/STO/Si interfaces at various stages throughout the growth and annealing process. XPS analysis showed minimal Si-O bonding at the STO/Si interface after the ALD process and after post-deposition annealing at 600 °C for 2 h. The results demonstrate a method to integrate epitaxial LAO films on Si(001) substrates by ALD.

Crystalline lanthanum aluminate (LAO) films were grown epitaxially on SrTiO<sub>3</sub>(001) and on Si(001) with a buffer layer of four unit cells of SrTiO<sub>3</sub> by atomic layer deposition. The SrTiO<sub>3</sub> buffer layer was grown by molecular beam epitaxy. Tris(N,N'-diisopropylformamidinate)-lanthanum, trimethylaluminum, and water as co-reactants were employed at 250 °C for atomic layer deposition. Films were characterized using *ex-situ* reflection high-energy electron diffraction, X-ray diffraction and *in-situ* X-ray photoelectron spectroscopy. The as-deposited LAO films were amorphous. Different annealing conditions were necessary to realize crystalline films because of different degrees of tensile strain between crystalline LAO and the SrTiO<sub>3</sub> or the Si(001) substrate. When grown on SrTiO<sub>3</sub>(001), with a lattice mismatch of 2.9%, annealing temperatures of 750 °C for 2 h were necessary. Crystalline films were realized at 600 °C under vacuum at

2 h for SrTiO<sub>3</sub>-buffered Si(001), with a lattice mismatch of 1.3%. By keeping the annealing temperature relatively low (2 h at 600 °C under vacuum), the interfacial amorphous layer at the STO/Si interface was minimized to about one monolayer and an abrupt interface between SrTiO<sub>3</sub> and LAO was maintained.

Atomic layer deposition (ALD) of epitaxial *c*-axis oriented BaTiO<sub>3</sub> (BTO) on Si(001) using a thin (1.6 nm) buffer layer of SrTiO<sub>3</sub> (STO) grown by molecular beam epitaxy is reported. The ALD growth of crystalline BTO films at 225 °C used barium bis(triisopropylcyclopentadienyl), titanium tetraisopropoxide, and water as co-reactants. X-ray diffraction (XRD) reveals a high degree of crystallinity and *c*-axis orientation of as-deposited BTO films. Crystallinity is improved after vacuum annealing at 600 °C. Two-dimensional XRD confirms the tetragonal structure and orientation of 7-20-nm thick films. The effect of the annealing process on the BTO structure is discussed. A clean STO/Si interface is found using *in-situ* X-ray photoelectron spectroscopy and confirmed by cross-sectional scanning transmission electron microscopy. The capacitance-voltage characteristics of 7-20 nm-thick BTO films are examined, and show an effective dielectric constant of ~660 for the heterostructure.

We report the formation of a quasi-two-dimensional electron gas (2-DEG) at the interface of  $\gamma$ -Al<sub>2</sub>O<sub>3</sub>/TiO<sub>2</sub>-terminated SrTiO<sub>3</sub> (STO) grown by atomic layer deposition (ALD). The ALD growth of Al<sub>2</sub>O<sub>3</sub> on STO(001) single crystal substrates was performed at temperatures in the range of 200–345 °C. Trimethylaluminum and water were used as co-reactants. *In situ* reflection high energy electron diffraction, *ex situ* x-ray diffraction, and *ex situ* cross-sectional transmission electron microscopy were used to determine the crystallinity of the Al<sub>2</sub>O<sub>3</sub> films. As-deposited Al<sub>2</sub>O<sub>3</sub> films grown above 300 °C were crystalline with the  $\gamma$ -Al<sub>2</sub>O<sub>3</sub> phase. *In situ* x-ray photoelectron spectroscopy was used to characterize the Al<sub>2</sub>O<sub>3</sub>/STO interface, indicating that a Ti<sup>3+</sup> feature in the Ti 2*p* spectrum

of STO was formed after 2–3 ALD cycles of Al<sub>2</sub>O<sub>3</sub> at 345 °C and even after the exposure to trimethylaluminum alone at 300 and 345 °C. The interface quasi-2-DEG exhibits moderately high mobility, with measured values of ~ 30 and 3,000 cm<sup>2</sup>V<sup>-1</sup>s<sup>-1</sup> at room temperature and 15 K, respectively. The interfacial conductivity depended on the thickness of the Al<sub>2</sub>O<sub>3</sub> layer. The Ti<sup>3+</sup> signal originated from the near interfacial region and vanished after annealing in an oxygen environment.

Cobalt oxide (CoO) films are grown epitaxially on Si(001) by atomic layer deposition (ALD) using a thin (1.6 nm) buffer layer of strontium titanate (STO) grown by molecular beam epitaxy. The ALD growth of CoO films is done at low temperature (170–180 °C), using cobalt bis(diisopropylacetamidinate) and water as co-reactants. Reflection high-energy electron diffraction, X-ray diffraction, and cross-sectional scanning transmission electron microscopy are performed to characterize the crystalline structure of the films. The CoO films are found to be crystalline as-deposited even at the low growth temperature with no evidence of Co diffusion into Si. The STO-buffered Si (001) is used as a template for ALD growth of relatively thicker epitaxial STO and TiO<sub>2</sub> films. Epitaxial and polycrystalline CoO films are then grown by ALD on the STO and TiO<sub>2</sub> layers, respectively, creating thin-film heterostructures for photoelectrochemical (PEC) testing. Both types of heterostructures, CoO/STO/Si and CoO/TiO<sub>2</sub>/STO/Si, demonstrate water photooxidation activity under visible light illumination. *In-situ* X-ray photoelectron spectroscopy is used to measure the band alignment of the two heterojunctions, CoO/STO and CoO/TiO<sub>2</sub>. The experimental band alignment is compared to electronic structure calculations using density functional theory.

We show the growth of CoO on SiO<sub>2</sub>/Si and MgO(001) substrates by ALD in a temperature range of 170–270 °C. Reflection high-energy electron diffraction is used to determine crystallinity and surface morphology of the films growth. While the CoO films

grown on SiO<sub>2</sub>/Si are poly-crystalline, the CoO films grown on single crystal substrate MgO(001) are crystalline and epitaxial. Attempts to grow CoO at temperatures higher than 305 °C result in ~ 31 % C-incorporated Co films. Polytrimethylsilylstyrene inhibits the nucleation of CoO on MgO, enabling selective area ALD on the proposed spin-transfer torque random access memory structure. The transformation of CoO to spinel Co<sub>3</sub>O<sub>4</sub> is observed by exposing CoO films to Hg UV light at room temperature for 30 min. We demonstrate the reduction of CoO forming carbon-free Co metal using Al and Sr metals to scavenge oxygen from CoO. The room temperature ferromagnetic behavior of the resultant Co films is observed. The magnetic coercivity of the resultant Co films varies from 30 to 1000 Oe depending on the method of reducing CoO. However, further studies are needed to explore the change in coercivity of the Co films and the ability to control it.

## **8.2. RECOMMENDATION FOR FUTURE WORK**

The successful integration of *c*-axis orientation BaTiO<sub>3</sub> on SrTiO<sub>3</sub>-buffered Si(001) demonstrates potential for integrating epitaxial oxides on Si(001) for use as a ferroelectric field effect transistor (FeFET). BaTiO<sub>3</sub> can also be integrated epitaxially on Ge(001), which will allow for the fabrication of the FeFET by an all chemical route. A graduate study in the Ekerdt group is researching the fabrication of FeFETs.

To continue exploring the two-dimensional electron gas (2DEG), different material systems, such as LaTiO<sub>3</sub>/SrTiO<sub>3</sub> and Eu-doped SrTiO<sub>3</sub>/LaAlO<sub>3</sub> will be studied. A better understanding of 2DEG mechanisms is necessary to further support which mechanism for 2DEG formation is most probable. If oxygen vacancies are majority

carriers in the case of amorphous oxides/SrTiO<sub>3</sub>, why the SrTiO<sub>3</sub> termination matters is still questionable.

For magnetic Co thin film work, the investigation of resultant cobalt film microstructure is being studied using x-ray diffraction to understand the correlation between structure and/or crystalline size of Co and magnetic property. This will give us ability to control the magnetic property of Co. Thermal reduction of CoO is also being studied using carbon monoxide and hydrogen. Selective area ALD of CoO will be further explored to enable selective deposition of CoO on spin-transfer torque random access memory structure. Additional ferromagnetic materials, such as Fe, Ni and alloys will also be studied in this research.

## Appendix

### FIRST-AUTHOR PUBLICATIONS

<sup>1</sup>T. Q. Ngo, A. Posadas, S. N. Chopra, M. D. McDaniel, J. Zhou, A. A. Demkov, and J. G. Ekerdt, “Atomic layer deposition of CoO and methods to form Co metal for STT-RAM applications,” **in preparation**.

<sup>2</sup>T. Q. Ngo, N. Goble, A. Posadas, K. J. Kormondy, S. Lu, M. D. McDaniel, J. Jordan-Sweet, D. J. Smith, X. P. A. Gao, A. A. Demkov, and J. G. Ekerdt, “Quasi-two-dimensional electron gas at the interface of  $\gamma$ -Al<sub>2</sub>O<sub>3</sub>/SrTiO<sub>3</sub> heterostructures grown by atomic layer deposition,” **under review**, J. Appl. Phys. (2015).

<sup>3</sup>T. Q. Ngo, M. D. McDaniel, A. Posadas, A. A. Demkov, and J. G. Ekerdt, “Oxygen Vacancies at the  $\gamma$ -Al<sub>2</sub>O<sub>3</sub>/STO Heterointerface Grown by Atomic Layer Deposition,” Mater. Res. Soc. Symp. Proc. **1730**, 294 (2015).

<sup>4</sup>T. Q. Ngo, A. B. Posadas, M. D. McDaniel, C. Hu, J. Bruley, E. T. Yu, A. A. Demkov, and J. G. Ekerdt, “Epitaxial c-axis oriented BaTiO<sub>3</sub> thin films on SrTiO<sub>3</sub> thin films on SrTiO<sub>3</sub>-buffered Si(001) by atomic layer deposition,” Appl. Phys. Lett. **104**, 082910 (2014).

<sup>5</sup>T. Q. Ngo, M. D. McDaniel, A. Posadas, A. A. Demkov, and J. G. Ekerdt, “Growth of crystalline LaAlO<sub>3</sub> by atomic layer deposition,” (invited) Proc. SPIE, **8987**, 898712 (1–10) (2014).

<sup>6</sup>T. Q. Ngo, A. Posadas, H. Seo, S. Hoang, M. D. McDaniel, D. Utes, D. H. Triyoso, C. B. Mullins, A. A. Demkov, and J. G. Ekerdt, “Atomic Layer Deposition of Photoactive CoO/SrTiO<sub>3</sub> and CoO/TiO<sub>2</sub> on Si(001) for Visible Light Driven Photoelectrochemical Water Oxidation,” J. Appl. Phys. **114**, 084901 (2013).

<sup>7</sup>T. Q. Ngo, A. Posadas, M. D. McDaniel, D. A. Ferrer, J. Bruley, C. Breslin, A. A. Demkov, and J. G. Ekerdt, “Epitaxial growth of LaAlO<sub>3</sub> on SrTiO<sub>3</sub>-buffered Si(001) substrates by atomic layer deposition,” J. Cryst. Growth. **363**, 150–157 (2013).

## CO-AUTHOR PUBLICATIONS

<sup>1</sup>M. D. McDaniel, C. Hu, S. Lu, T. Q. Ngo, A. Posadas, A. Jiang, D. J. Smith, E. T. Yu, A. A. Demkov, and J. G. Ekerdt, “Atomic layer deposition of crystalline SrHfO<sub>3</sub> directly on Ge (001) for high-k dielectric applications,” *J. Appl. Phys.* **117**, 054101 (2015).

<sup>2</sup>M. D. McDaniel, T. Q. Ngo, A. Posadas, C. Hu, S. Lu, D. J. Smith, E. T. Yu, A. A. Demkov, J. G. Ekerdt, “A chemical route to monolithic integration of crystalline oxides on semiconductors,” *Adv. Mater. Interfaces*, **1**, 140008 (2014).

<sup>3</sup>K. J. Kornondy, A. B. Posadas, T. Q. Ngo, S. Lu, N. Goble, J. Jordan-Sweet, X. P. A. Gao, D. J. Smith, M. R. McCartney, J. G. Ekerdt, and A. A. Demkov, *J. Appl. Phys.* **117**, 095303 (2015).

<sup>4</sup>M. D. McDaniel, A. Posadas, T. Q. Ngo, C. Karako, J. Bruley, V. Narayanan, A. A. Demkov, and J. G. Ekerdt, “Incorporation of La in epitaxial SrTiO<sub>3</sub> thin films grown by atomic layer deposition on SrTiO<sub>3</sub>-buffered Si (001) substrates,” *J. Appl. Phys.* **115**, 224108 (2014).

<sup>5</sup>A. A. Demkov, A. B. Posadas, H. Seo, M. Choi, K. J. Kornondy, P. Ponath, R. C. Hatch, M. D. McDaniel, T. Q. Ngo, and J. G. Ekerdt, “Monolithic integration of oxides on semiconductors,” (invited) *ECS Transactions*, 2013, **54**, 255–269 (2013).

<sup>6</sup>M. D. McDaniel, A. Posadas, T. Q. Ngo, A. Dhamdhere, D. J. Smith, A. A. Demkov, and J. G. Ekerdt, “Epitaxial strontium titanate films grown by atomic layer deposition on SrTiO<sub>3</sub>-buffered Si(001) substrates,” *J. Vac. Sci. Technol. A* **31**, 01A136 (2013).

<sup>7</sup>M. D. McDaniel, A. Posadas, T. Q. Ngo, A. Dhamdhere, D. J. Smith, A. A. Demkov, and J. G. Ekerdt, “Growth of epitaxial oxides on silicon using atomic layer deposition: Crystallization and annealing of TiO<sub>2</sub> on STO-buffered Si(001),” *J. Vac. Sci. Technol. B* **30**, 04E111 (2012).

<sup>8</sup>S. Hoang, T. Q. Ngo, S. P. Berglund, R. R. Fullon, J. G. Ekerdt, and C. B. Mullins, “Improvement of Solar Energy Conversion with Nb-incorporated TiO<sub>2</sub> Hierarchical Micro-spheres,” *ChemPhysChem.* **14**, 2270-2276 (2013).

## TECHNICAL PRESENTATIONS

<sup>1</sup>(Presentation) *Two-dimensional electron gas at the  $\gamma$ -Al<sub>2</sub>O<sub>3</sub>/SrTiO<sub>3</sub> heterostructures grown by ALD*, 2014 Materials Research Society (MRS) Fall meeting, Boston, Massachusetts, December 03, 2014.

<sup>2</sup>(Presentation) *Integration of ferroelectric perovskites on Ge(001) by atomic layer deposition: A case study of BaTiO<sub>3</sub>*, American Vacuum Society (AVS) Fall 2014 meeting, Baltimore, Maryland; November 10, 2014.

<sup>3</sup>(Invited Presentation) *Epitaxial growth of LaAlO<sub>3</sub> on SrTiO<sub>3</sub>-buffered Si(001) substrates by Atomic Layer Deposition*, SPIE, Oxide-based Materials and Devices International Conference, San Francisco, California; February 2014.

<sup>4</sup>(Poster) *Integration of Ferroelectric Perovskites on Si(001) and Ge(001) by ALD: A case study of BaTiO<sub>3</sub>*, 32<sup>nd</sup> International Conference on the Physics of Semiconductors (ICPS), Austin, Texas; August 12, 2014.

<sup>5</sup>(Presentation) *Integration of functional perovskite (ABO<sub>3</sub>) layers on Si(001) by ALD using a thin SrTiO<sub>3</sub> buffer layer*, 13<sup>th</sup> International Conference on Atomic Layer Deposition (ALD2013), San Diego, California; July 30, 2013. This presentation was awarded as one of finalists for Best Paper Award at the Conference.

## Bibliography

S. Abel, M. Sousa, C. Rossel, D. Caimi, M. D. Rossell, R. Erni, J. Fompeyrine, and C. Marchiori, *Nanotechnol.* **24**, 285701 (2013).

S. Abel, T. Stöferle, C. Marchiori, C. Rossel, M. D. Rossell, R. Erni, D. Caimi, M. Sousa, A. Chelnokov, B. J. Offrein, and J. Fompeyrine, *Nat. Commun.* **4**, 1671 (2013).

Ariando, X. Wang, G. Baskaran, Z. Q. Liu, J. Huijben, J. B. Yi, A. Annadi, A. Roy Barman, A. Rusydi, S. Dhar, Y. P. Feng, J. Ding, H. Hilgenkamp, and T. Venkatesan, *Nat. Comm.* **2**, 188 (2011).

P. R. Arya , P. Jha, G. N. Subbanna, and A. K. Ganguli, *Mater. Res. Bull.* **38**, 617 (2003).

O. Aubel, C. Hennesthal, M. Hauschildt, A. Beyer, J. Poppe, G. Talut, M. Gall, J. Hahn, J. Boemmels, M. Nopper, and R. Seidel, *IEEE*, 26–28 (2011).

A. J. Bard, M. A. Fox, *Acc. Chem. Res.* **28**, 141 (1995).

G. Benko, J. Kallioinen, J. E. I. K. Tommola, A. P. Yarstev, V. Sundstrom, *J. Am. Chem. Soc.* **124**, 489 (2002).

I. Bergenti, A. Riminucci, E. Arisi, M. Murgia, M. Cavallini, M. Solzi, F. Casoli, V. Dediu, *J. Magn. Magn. Mater.* **316**, e987–e989 (2007).

G. W. Berkstresser, A. J. Valentino, and C. D. Brandle, *J. Cryst. Growth* **109**, 457–466 (1991).

J. A. Bert, B. Kalisky, C. Bell, M. Kim, Y. Hikita, H. Hwang, and K. A. Moler, *Nat. Phys.* **7**, 767–771 (2011).

S. Binham and W. A. Daoud, *J. Mater. Chem.* **21**, 2041 (2011).

P. E. Blöchl, *Phys. Rev. B* **50**, 17953 (1994).

T. Bredow and A. R. Gerson, *Phys. Rev. B* **61**, 5194–5201 (2000).

- G. Burgeth and H. Kisch, *Coord. Chem. Rev.* **230**, 41 (2002).
- M. Burriel, G. Garcia, J. Santiso, A. Abruits, Z. Saltyte, and A. Figueras, *Chem. Vap. Deposition* **11**, 106 (2005).
- A. D. Caviglia, S. Gariglio, N. Reyren, D. Jaccard, T. Schneider, M. Gabay, S. Thiel, G. Hammerl, J. Mannhart, and J. -M. Triscone, *Nature* **456**, 624–627 (2008).
- S. A. Chambers, *Adv. Mater.* **22**, 219 (2010).
- S. A. Chambers, M. H. Engelhard, V. Shutthanandan, Z. Zhu, T. C. Droubay, L. Qiao, P. V. Sushko, T. Feng, H. D. Lee, T. Gustafsson, E. Garfunkel, and A. B. Shah, *Surf. Sci. Rep.* **65**, 317 (2010).
- S.A. Chambers, Y. Liang, Z. Yu, R. Droopad, J. Ramdani, and K. Eissenbeiser, *Appl. Phys. Lett.* **77**, 1662 (2000).
- S.A. Chambers, Y. Liang, Z.J. Zu, R. Droopad, J. Ramdani, and K. Eisenbeiser, *J. Vac. Sci. Technol. A* **19**, 934 (2001).
- Y. Z. Chen, N. Bovet, F. Trier, D. V. Christensen, F. M. Qu, N. H. Andersen, T. Kasama, W. Zhang, R. Giraud, J. Dufouleur, T. S. Jespersen, J. R. Sun, A. Smith, J. Nygård, L. Lu, B. Büchner, B. G. Shen, S. Linderoth, and N. Pryds, *Nat. Commun.* **4**, 1371 (2012).
- Y. Z. Chen, N. Bovet, T. Kasama, W. W. Gao, S. Yazdi, C. Ma, N. Pryds, and S. Linderoth, *Adv. Mater.* **26**, 1462 (2013).
- Y. Chen, N. Pryds, J. E. Kleibeuker, G. Koster, J. Sun, E. Stamate, B. Shen, G. Rijnders, and S. Linderoth, *Nano Lett.* **11**, 3774 (2011).
- M. Choi, A. Posadas, R. Dargis, C. -K. Shih, A. A. Demkov, D. H. Triyoso, N. D. Theodore, C. Dubourdieu, J. Bruley, and J. Jordan-Sweet, *J. Appl. Phys.* **111**, 064112 (2012).
- E. Chornet and S. Czernik, *Nature* **418**, 928 (2002).
- T. J. Chuang, C. R. Brundle, and D. W. Rice, *Surf. Sci.* **59**, 413 (1976).

R. D. Clark, *Materials* **7**, 2913–2944 (2014).

S. Coh, T. Heeg, J. H. Haeni, M. D. Biegalski, J. Lettieri, L. F. Edge, K. E. O'Brien, M. Bernhagen, P. Reiche, R. Uecker, S. Trolrier-McKinstry, D. G. Schlom, and D. Vanderbilt, *Phys. Rev. B* **82**, 064101 (2010).

G. Congedo, S. Spiga, L. Lamagna, A. Lamperti, Y. Lebedinskii, Y. Matveyev, A. Zenkevich, P. Chernykh, and M. Fanciulli, *Microelectro. Engin.* **86**, 1696–1699 (2009).

Crabtree G. W., M. S. Dresselhaus, and M. V. Buchanan, *Phys. Today* **39** (2004).

S. Czernik, R. French, C. Feik, and E. Chornet, U.S. DOE Hydrogen Program Review, UREL/CP-**610**, 32405 (2002).

N. Deo, M. F. Bain, J. H. Montgomery, H. S. Gamble, *J. Mater. Sci. Mater. Electron.* **16**, 387–392 (2005).

L. G. Devi, N. Kottam, and S. G. Kumar, *J Phys. Chem. C* **113**, 15593 (2009).

M. J. Dicken, K. Diest, Y. B. Park, and H. A. Atwater, *J. Cryst. Growth* **300**, 330–335 (2007).

L. J. Diguna, Q. Shen, J. Kobayashi, and T. Toyoda, *Appl. Phys. Lett.* **91**, 023116 (2007).

M. Diskus, O. Nilsen, and H. Fjellvåg, *Chem. Vap. Deposition* **17**, 135 (2011).

M. E. Donders, H. C. M. Knoop, M. C. M. Van de Sanden, W. M. M. Kessels, and P. H. L. Notten, *J. Electrochem. Soc.* **158**, G92 (2011).

A. Driskill-Smith, D. Apalkov, V. Nikitin, X. Tang, S. Watts, D. Lottis, K. Moon, A. Khvalkovskiy, R. Kawakami, X. Luo, A. Ong, E. Chen, and M. Krounbi, 3<sup>rd</sup> IEEE International 1–3, (2011).

R. Droopad, Z. Yu, H. Li, Y. Liang, C. Overgaard, A. Demkov, X. Zhang, K. Moore, K. Eisenbeiser, M. Hu, J. Curless, and J. Funder, *J. Cryst. Growth* **251**, 638–644 (2003).

C. Dubourdieu, J. Bruley, T. M. Arruda, A. Posadas, J. Jordan-Sweet, M. M. Frank, E. Cartier, D. J. Frank, S. V. Kalinin, A. A. Demkov, and V. Narayanan, *Nature Nanotechnology* **8**, 748 (2013).

S. L. Dudarev, G. A. Botton, S. Y. Savrasov, C. J. Humphreys, and A. P. Sutton, *Phys. Rev. B* **57**, 1505 (1998).

L. F. Edge, D. G. Schlom, P. Sivasubramani, R. M. Wallance, B. Holländer, and J. Schubert, *Appl. Phys. Lett.* **88**, 112907 (2006).

L. F. Edge, D. G. Schlom, S. A. Chambers, E. Cicerrella, J. L. Freeouf, B. Holländer, and J. Schubert, *Appl. Phys. Lett.* **84**, 726 (2004).

M. El Kazzi, G. Delhayé, C. Merckling, E. Bergignat, Y. Robach, G. Grenet, and G. Hollinger, *J. Vac. Sci. Technol. A* **25**, 1505–1511 (2007).

T. D.-M. Elko-Hansen and J. G. Ekerdt, *Chem. Mater.* **26**, 2642–2646 (2014).

T. D.-M. Elko-Hansen, A. Dolocan, and J. G. Ekerdt, *J. Phys. Chem. Lett.* **5**, 1091–1095 (2014).

D. Eom, C. S. Hwang, H. J. Kim, M.-H. Cho, and K. B. Chung, *Electrochem. Solid-State Lett.* **11**, G33-G36 (2008).

E. Fortunato, P. Barquinha, and R. Martins, *Adv. Mater.* **24**, 2945 (2012).

E. Fujii, H. Torii, A. Tomozawa, R. Takayama, and T. Hirao, *J. Mater. Sci.* **30**, 6013 (1995).

A. Fujishima and K. Honda, *Nature* **238**, 37 (1972).

A. Fujishima, T. N. Rao, and D. A. Tryk, *J. Photochem. Photobiol. C: Photochem. Rev.* **1**, 1 (2000).

J. P. George, J. Beeckman, W. Woestenborghs, P. F. Smet, W. Bogaerts, and K. Neyts, *Nanoscale Res. Lett.* **8**:62, 1–7 (2013).

- S. M. George, *Chem. Rev.* **110**, 111–131 (2010).
- D. T. Gillaspie, R. C. Tenent, and A. C. Dillon, *J. Mater. Chem.* **20**, 9585 (2010).
- L. V. Goncharova, D. G. Starodub, E. Garfunkel, T. Gustafsson, V. Vaithyanathan, J. Lettieri, and D. G. Schlom, *J. Appl. Phys.* **100**, 014912 (2006).
- R. G. Gordon, H. Kim, and H. Bhandari, US Patent 7, 973,789 B2 (2011).
- S. Hara, M. Yoshimizu, S. Tanigawa, L. Ni, B. Ohtani, and H. Irie, *J. Phys. Chem. C* **116**, 17458 (2012).
- K. Hashimoto, H. Irie, and A. Fujishima, *Japan. J. Appl. Phys.* **44**, 8269 (2005).
- H.S. Hilal, L.Z. Majjad, N. Zaatari, and A.E. Hamouz, *Solid State Sci.* **9**, 9 (2007).
- T. Hirakawa and Y. Nosaka, *J. Phys. Chem. C*, **112**, 15818 (2008).
- S. Hoang, S. Guo, N. T. Hahn, A. J. Bard, and C. B. Mullins, *Nano Lett.* **12**, 26 (2012).
- C. T. Horng and R.-Y. Tong, US Patent, US20130175644 A1 (2013).
- C. T. Horng, R.-Y. Tong, C.-J. Torng, and W. Kula, US Patent, US8372661 B2 (2013).
- C. Hou, Q. Xu, L. Yin, and X. Hu, *Analyst*, **137**, 5803–5808 (2012).
- C. S. Hwang, *Atomic layer deposition for semiconductors*, Springer (2014).
- H. Y. Hwang, Y. Iwasa, M. Kawasaki, B. Keimer, N. Nagaosa, and Y. Tokura, *Nat. Mater.* **11**, 103 (2012).
- S. Ikeda, K. Miura, H. Yamamoto, K. Mizunuma, H. G. Gan, M. Endo, S. Kanai, J. Hayakawa, F. Matsukura, and H. Ohno, *Nature Mater.* **9**, 721–724 (2010).
- N. Izyumskaya, Y. Alivov, and H. Morkoç, *Crit. Rev. Sol. Stat. Mater. Sci.* **34**, 89–179 (2009).

J. Jitputti, S. Pavasupree, Y. Suzuki, and S. Yoshikawa, *J. Solid State Chem.* **180**, 1743 (2007).

J. Y. Jo, Y. S. Kim, T. W. Noh, J.-G. Yoon, and T. K. Song, *Appl. Phys. Lett.* **89**, 232909 (2006).

R. W. Johnson, A. Hultqvist, and S. F. Bent, *Mater. Today* **17**, 236–246 (2014).

J. H. Jun and D. J. Choi, *Jpn. J. Appl. Phys.* **43**, 7576–7578 (2004).

J. H. Jun, J. Jun, and D. J. Choi, *Electrochem. Solid-State Lett.* **6**, F37–F39 (2003).

M.W. Kanan, D.G. Nocera, *Science* **321**, 1072 (2008).

S. Kawasaki, K. Nakatsuji, J. Yoshinobu, F. Komori, R. Takahashi, M. Lippmaa, K. Mase, and A. Kudo, *Appl. Phys. Lett.* **101**, 033910 (2012).

A. Kay, I. Cesar and M. Grätzel, *J. Am. Chem. Soc.* **128**, 15714 (2006).

R. J. Kennedy, *IEEE Trans. Magn.* **31**, 3829–3831 (1995).

A. I. Khan, D. Bhowmik, P. Yu, S. J. Kim, X. Pan, R. Ramesh, and S. Salahuddin, *Appl. Phys. Lett.* **99**, 113501 (2011).

S. U. M. Khan, M. Al-Shahry, and W. B. Ingler, *Science* **297**, 2243 (2002).

H. Kim, *J. Vac. Sci. Technol. B* **21**, 2231 (2003).

H. Kim, M. Seol, J. Lee, and K. Yong, *J. Phys. Chem. C* **115**, 25429 (2011).

H. Kisch, L. Zhang, C. Lange, W. F. Maier, C. Antonius, and D. Meissner, *Angew. Chem. Int. Ed.* **37**, 3034 (1998).

K. B. Klepper, O. Nilsen, and H. Fjellvåg, *J. Cryst. Growth* **307**, 457 (2007).

- K. B. Klepper, O. Nilsen, and H. Fjellvåg, *Thin Solid Films* **515**, 7772 (2007).
- A. Kohn, M. Eizenberg, and Y. Shacham-Diamand, *J. Appl. Phys.* **94**, 3015–3024 (2003).
- K. J. Kormondy, A. B. Posadas, A. Slepko, A. Dhamdhere, D. J. Smith, K. N. Mitchell, T. I. Willett-Gies, S. Zollner, L. G. Marshall, J. Zhou, and A. A. Demkov, *J. Appl. Phys.* **115**, 243708 (2014).
- K. J. Kormondy, A. B. Posadas, T. Q. Ngo, S. Lu, N. Goble, J. Jordan-Sweet, X. P. A. Gao, D. J. Smith, M. R. McCartney, J. G. Ekerdt, and A. A. Demkov, *J. Appl. Phys.* **117**, 095303 (2015).
- G. Kresse and J. Furthmüller, *Phys. Rev. B* **54**, 11169 (1996).
- K. Kukli, M. Ritala, V. Pore, M. Leskelä, T. Sajavaara, R. I. Hegde, D. C. Gilmer, P. J. Tobin, A. C. Jones, and H. C. Aspinall, *Chem. Vap. Deposition* **12**, 158–164 (2006).
- S.G. Kumar and L.G. Devi, *J. Phys. Chem. A*, **115**, 13211 (2011).
- J. Lee and A. A. Demkov, *Phys. Rev. B* **78**, 193104 (2008).
- S. W. Lee, J. Heo, and R. G. Gordon, *Nanoscale* **5**, 8940 (2013).
- S. W. Lee, Y. Liu, J. Heo, and R. G. Gordon, *Nano Lett.* **12**, 4775 (2012).
- M. Leskelä, M. Ritala, and O. Nilsen, *MRS Bulletin* **36**, 877–884 (2011).
- A. D. Li, J. B. Cheng, Q. Y. Shao, H. Q. Ling, D. Wu, Y. Wang, M. Wang, Z. G. Liu, N. B. Ming, C. Wang, H. W. Zhou, and B. Y. Nguyen, *Ferroelec.* **329**, 73–77 (2005).
- D. Li, H. Haneda, N.K. Labhestwar, S. Hishita, and N. Ohashi, *Chem. Phys. Lett.* **401**, 579 (2005).
- H. Li, X. Hu, Y. Wei, Z. Yu, X. Yang, R. Droopad, A. A. Demkov, J. Erwards, K. Moore, W. Ooms, J. Kulik, and P. Fejes, *J. Appl. Phys.* **39**, 4521–4525 (2003).
- L. Li, C. Richter, J. Mannhart, and R. C. Ashoori, *Nat. Phys.* **7**, 762–766 (2011).

- W. Y. Li, L. N. Xu, and J. Chen, *Adv. Func. Mater.* **5**, 851–857 (2005).
- X. L. Li, H. B. Lu, M. Li, Z. Mai, H. Kim, and Q. J. Jia, *Appl. Phys. Lett.* **92**, 012902 (2008).
- Y. Liang, Y. Li, H. Wang, J. Zhou, J. Wang, T. Regier, and H. Dai, *Nat. Mater.* **10**, 780–786 (2011).
- B. S. Lim, A. Rahtu, and R. G. Gordon, *Nat. Mater.* **2**, 749 (2003).
- C. Lin and A. A. Demkov, *Phys. Rev. Lett.* **111**, 217601 (2013).
- C. Lin, C. Mitra, and A. A. Demkov, *Phys. Rev. B* **86**, 161102(R) (2012).
- H. Ling, X. Lu, A. Li, D. Wu, Q. Shao, J. Sheng, Z. Liu, N. Ming, X. Wang, B. Y. Nguyen, and H. Zhou, *Appl. Phys. A* **80**, 641–644 (2005).
- K. -C. Liu, W. -H. Tzeng, K. -M. Chang, J. -J. Huang, Y. -J. Lee, P. -H Yeh, P. -S. Chen, H. -Y. Lee, F. Chen, and M. -J. Tsai, *Thin Solid Film* **520**, 1246–1250 (2011).
- Z. Q. Liu, C. J. Li, W. M. Lü, X. H. Huang, Z. Huang, S. W. Zeng, X. P. Qiu, L. S. Huang, A. Annadi, J. S. Chen, J. M. D. Coey, T. Venkatesan, and Ariando, *Phys. Rev. X* **3**, 021010 (2013).
- X. B. Lu, Z. G. Liu, Y. P. Wang, Y. Yang, X. P. Wang, H. W. Zhou, and B. Y. Nguyen, *J. Appl. Phys.* **94**, 1229 (2003).
- X. Luo and B. Wang, *J. Appl. Phys.* **104**, 073518 (2008).
- J. H. Ma, Z. M. Huang, X. J. Meng, S. J. Liu, X. D. Zhang, J. L. Sun, J. Q. Xue, and J. H. Chu, *J. Appl. Phys.* **99**, 033515 (2006).
- S. B. Majumder, M. Jain, A. Martinez, R. S. Katiyar, F. W. van Keuls, and F. A. Miranda, *J. Appl. Phys.* **90**, 896–903 (2001).
- A. U. Mane, K. Shalini, and A. Wohlfart, *J. Cryst. Growth* **240**, 157 (2002).

- J. Mannhart and D. G. Schlom, *Science* **327**, 1607 (2010).
- R. Mantovan, M. Georgieva, M. Perego, H. L. Lu, S. Cocco, A. Zenkevich, G. Scarel, and M. Fanciulli, *Acta Physica Polonica A*, **112**, 1271–1280 (2007).
- J. G. Mavroides, J. A. Kafalas, and D. F. Kolesar, *Appl. Phys. Lett.* **28**, 141 (1976).
- A. McCollam, S. Wenderich, M. K. Kruize, V. K. Guduru, H. J. A. Molegraaf, M. Huijben, G. Koster, D. H. A. Blank, G. Rijnders, A. Brinkman, H. Hilgenkamp, U. Zeitler, and J. C. Maan, *Appl. Phys. Lett.* **2**, 022102 (2014).
- M. D. McDaniel, T. Q. Ngo, A. Posadas, C. Hu, S. Lu, D. J. Smith, E. T. Yu, A. A. Demkov, and J. G. Ekerdt, *Adv. Mater. Interfaces*, **1**, 1400081 (2015).
- M. D. McDaniel, C. Hu, S. Lu, T. Q. Ngo, A. Posadas, A. Jiang, D. J. Smith, E. T. Yu, A. A. Demkov, and J. G. Ekerdt, *J. Appl. Phys.* **117**, 054101 (2015).
- M. D. McDaniel, A. Posadas, T. Q. Ngo, A. Dhamdhare, D. J. Smith, A. A. Demkov, and J. G. Ekerdt, *J. Vac. Sci. Technol. A* **31**, 01A136 (2013).
- M. D. McDaniel, A. Posadas, T. Q. Ngo, A. Dhamdhare, D. J. Smith, A. A. Demkov, and J. G. Ekerdt, *J. Vac. Sci. Technol. B* **30**, 04E111 (2012).
- M. D. McDaniel, A. Posadas, T. Wang, A. A. Demkov, and J. G. Ekerdt, *Thin Solid Film* **520**, 6525–6530 (2012).
- R. A. McKee, F. J. Walker, and M. F. Chisholm, *Phys. Rev. Lett.* **81**, 3014 (1998).
- R. A. McKee, F. J. Walker, and M. F. Chisholm, *Science* **293**, 468 (2001).
- J. S. Meena, S. M. Sze, U. Chand, and T.-Y. Tseng, *Nanoscale Res. Lett.* **9**, 526 (2014).
- C. Merckling, G. Delhaye, M. El-Kazzi, S. Gaillard, Y. Rozier, L. Rapenne, B. Chenevier, O. Marty, G. Saint-Girons, M. Gendry, Y. Robach, and G. Hollinger, *Microelectro. Relia.* **47**, 540–543 (2007).

C. Merckling, G. Saint-Girons, C. Botella, G. Hollinger, M. Heyns, J. Dekoster, and M. Caymax, *Appl. Phys. Lett.* **98**, 092901 (2011).

W. J. Merz, *Phys. Rev.* **95**, 690 (1954).

Y.Y. Mi, Z. Yu, S. J. Wang, P. C. Lim, Y. L. Foo, A. C. H. Huan, and C. K. Ong, *Appl. Phys. Lett.* **90**, 181925 (2007).

V. Miikkulainen, M. Leskelä, M. Ritala, and R. L. Puurunen, *J. Appl. Phys.* **113**, 021301 (2013).

C. Mitra, C. Lin, J. Robertson, and A. A. Demkov, *Phys. Rev. B* **86**, 155105 (2012).

E. Montoya, S. Bals, M. D. Rossell, D. Schryvers, and G. V. Tendeloo, *Microsc. Res. Tech.* **70**, 1060–1071 (2007).

P. Moon, V. Dubin, S. Johnston, J. Leu, K. Raol, and C. Wu, *IEEE Int. Electron Devices Meet.* 841 (2003).

N. Nakagawa, H. Y. Hwang, and D. A. Muller, *Nat. Mater.* **5**, 204 (2006).

M. M. Natile and A. Glisenti, *Chem. Mater.* **14** (7), 3090–3099 (2002).

J. Ng, S. Xu, X. Zhang, H. Y. Yang, and D. D. Sun, *Adv. Funct. Mater.* **20**, 4287 (2010).

J. H. Ngai, F. J. Walker, and C. H. Ahn, *Annu. Rev. Mater. Res.* **44**, 1 (2014).

T. Q. Ngo, M. D. McDaniel, A. Posadas, A. A. Demkov, and J. G. Ekerdt, *Proc. of SPIE*, **8987**, 898712 (2014).

T. Q. Ngo, A. B. Posadas, M. D. McDaniel, C. Hu, J. Bruley, E. T. Yu, A. A. Demkov, and J. G. Ekerdt, *Appl. Phys. Lett.* **104**, 082910 (2014).

T. Q. Ngo, A. Posadas, H. Seo, S. Hoang, M. D. McDaniel, D. Utess, D. H. Triyoso, C. B. Mullins, A. A. Demkov, and J. G. Ekerdt, *J. Appl. Phys.* **114**, 084901 (2013).

T. Q. Ngo, A. Posadas, M. D. McDaniel, D. A. Ferrer, J. Bruley, C. Breslin, A. A. Demkov, and J. G. Ekerdt, *J. Cryst. Growth*, **363**, 150–157 (2013).

M. Nieminen, T. Sajavaara, E. Rauhala, M. Putkonen, and L. Niinistö, *J. Mater. Chem.* **11**, 2340-2345 (2011).

G.A. Niklasson and C. G. Granqvist, *J. Mater. Chem.* **17**, 127 (2006).

F. Niu and B. W. Wessels, *J. Vac. Sci. Technol. B* **25**, 1053 (2007).

G. Niu, S. Yin, G. Saint-Girons, B. Gautier, P. Lecoœur, V. Pillard, G. Hollinger, and B. Vilquin, *Microelectron. Eng.* **88**, 1232 (2011).

A. Ohtomo and H. Y. Hwang, *Nature* **427**, 423 (2004).

J. Overpeck, K. Huguen, D. Hardy, R. Bradley, R. Case, M. Douglas, B. Finney, K. Gajewski, G. Jacoby, A. Jennings, S. Lamoureux, A. Lasca, G. MacDonald, J. Moore, M. Retelle, S. Smith, A. Wolfe, and G. Zielinski, *Science* **278**, 1251 (1997).

F. Pan, D. Olaya, J. C. Price, and C. T. Rogers, *Appl. Phys. Lett.* **84**, 1573–1575 (2004).  
S. Parkin, X. Jiang, C. Kaiser, A. Panchula, K. Rochie, and M. Samant, *Proc. IEEE*, **91**, 661–680 (2003).

G. N. Parsons, J. W. Elam, S. M. George, S. Haukka, H. Jeon, W. M. M. Kessels, M. Leskelä, P. Poodt, M. Ritala, and S. M. Rossnagel, *J. Vac. Sci. Technol. A* **31**, 050818 (2013).

S. A. Pauli, S. J. Leake, B. Delley, M. Bjorck, C. W. Schneider, C. M. Schlepütz, D. Martoccia, S. Paetel, J. Mannhart, and P. R. Willmott, *Phys. Rev. Lett.* **106**, 023101 (2011).

J. P. Perdew and A. Zunger, *Phys. Rev. B* **23**, 5048 (1981).

S. C. Petitto and M. A. Langell, *J. Vac. Sci. Technol. A* **22**, 1690 (2004).

S. C. Petitto, E. M. Marsh, G. A. Carson, M. Langell, *J. Mole. Catal. A Chem.* **281**, 49 (2008).

J. S. Ponraj, G. Attolini, and M. Bosi, *Crit. Rev. Solid State Mater. Sci.* **38**, 203–233 (2013).

A. Posadas, M. Berg, H. Seo, D. J. Smith, H. Celio, A. P. Kirk, D. Zhernokletov, R. M. Wallace, A. de Lozanne, and A. A. Demkov, *Appl. Phys. Lett.* **98**, 055104 (2011).

A. Posadas, R. Dargis, M. Choi, A. Slepko, J. J. Kim, D. J. Smith, and A. A. Demkov, *J. Vac. Sci. Technol. B* **29**, 1071 (2011).

B. Presa, R. Matarranz, C. Clavero, J. M. García-Martín, J. F. Calleja, and M. C. Contreras, *J. Appl. Phys.* **102**, 053901 (2007).

L. Qiao, H. Y. Xiao, H. M. Meyer, J. N. Sun, C. M. Rouleau, A. A. Puretzky, D. B. Geohegan, I. N. Ivanov, M. Yoon, W. J. Webber, and M. D. Biegalski, *J. Mater. Chem. C*, **1**, 4628–4633 (2013).

S. Y. Reece, J. A. Hamel, K. Sung, T. D. Jarvi, A. J. Esswein, J. J. H. Pijpers, and D. G. Nocera, *Science* **334**, 645 (2011).

J. W. Reiner, A. M. Kolpak, Y. Segal, K. F. Garrity, S. Ismail-Beigi, C. H. Ahn, and F. J. Walker, *Adv. Mater.* **22**, 2919 (2010).

J. W. Reiner, A. Posadas, M. Wang, M. Sidorov, Z. Krivokapic, F. J. Walker, T. P. Ma, and C. H. Ahn, *J. Appl. Phys.* **105**, 124501 (2009).

N. Reyren, M. Bibes, E. Lesne, J.-M. George, C. Deranlot, S. Collin, A. Barthélémy, and H. Jaffrès, *Phys. Rev. Lett.* **108**, 186802 (2012).

L. C. Richter, J. Mannhart, and R. C. Ashoori, *Nat. Phys.* **7**, 762–766 (2011).

J. Robertson, *Rep. Prog. Phys.* **69**, 327–396 (2006).

C. Rödl, F. Fuchs, J. Furthmüller, and F. Bechstedt, *Phys. Rev. B* **79**, 235114 (2009).

C. Rossel, M. Sousa, C. Marchiori, J. Fompeyrine, D. Webb, D. Caimi, B. Mereu, A. Ispas, J. P. Locquet, H. Siegwart, R. Germann, A. Tapponnier, and K. Babich, *Microelectro. Eng.* **84**, 1869–1873 (2007).

- J. Rothstein, *Internatl. J. Hydrogen Energy* **21**, 137 (1996).
- U. Roy, T. Pramanik, M. Tsoi, L. F. Register, and S. Banerjee, *J. Appl. Phys.* **113**, 223904 (2013).
- S. Salahuddin and S. Datta, *Nano Lett.* **8**, 405 (2008).
- H. K. Sato, C. Bell, Y. Hikita, and H. Y. Hwang, *Appl. Phys. Lett.*, **102**, 251602 (2013).
- N. M. Sbrockey, M. Luong, E. M. Gallo, J. D. Sloppy, G. Chen, C. R. Winkler, S. H. Johnson, M. L. Taheri, G. S. Tompa, and J. E. Spanier, *J. Electro. Mater.* **41**, 819–823 (2012).
- D. Schmidt, A. C. Kjerstad, T. Hofmann, R. Skomski, E. Schubert, and M. Schubert, *J. Appl. Phys.* **105**, 113508 (2009).
- H. Schneidewind and G. Bruchlos, *Trans. Appl. Supercond.* **13**, 2766–2768 (2003).
- H. Schneidewind, M. Manzel, G. Bruchlos, and K. Kirsch, *Supercond. Sci. Technol.* **14**, 200–212 (2001).
- F. Schoofs, M. Egilmez, T. Fix, J. L. MacManus-Driscoll, and M. G. Blamire, *Appl. Phys. Lett.* **100**, 081601 (2012).
- H. Seo, A. B. Posadas, C. Mitra, A. V. Kvit, J. Ramdani, and A. A. Demkov, *Phys. Rev. B* **86**, 075301 (2012).
- J. W. Seo, Ch. Dieker, A. Tapponnier, C. Marchiori, M. Sousa, J. -P. Locquet, J. Fompeyrine, A. Ispas, C. Rossel, Y. Panayiotatos, A. Sotiropoulos, and A. Dimoulas, *Microelectro. Eng.* **84**, 2328–2331 (2007).
- K. Shalini, A. U. Mane, S. A. Shivashankar, M. Rajeswari, and S. Choopun, *J. Cryst. Growth* **231**, 242 (2001).
- W. Siemons, G. Koster, H. Yamamoto, W. A. Harrison, G. Lucovsky, T. H. Geballe, D. H. A. Blank, and M. R. Beasley, *Phys. Rev. Lett.* **98**, 196802 (2007).

- T. Suntola, J. Antson, U.S. Patent 4,058,430 (1977).
- T. Suntola, A. Pakkala, S. Lindfors, U.S. Patent 4,389,97 (1983).
- P. D. Tall, C. Coupeau, and J. Rabier, and *Scripta Materialia* **49**, 903–908 (2003).
- F. Tang, D.-L. Liu, D.-X. Ye, Y.-P. Zhao, T.-M. Lu, G.-C. Wang, and A. Vijayaraghavan, *J. Appl. Phys.* **93**, 4194 (2003).
- J. Tang, J. R. Durrant, and D. R. Klug, *J. Am. Chem. Soc.* **130**, 13885 (2008).
- G. H. Thomas, E. D. Specht, J. Z. Larese, Z. B. Xue, and D. B. Beach, *J. Mater. Res.* **12**, 3281–3287 (2008).
- D. H. Triyoso, H. Li, R.I. Hegde, Z. Yu, K. Moore, J. Grant, B. E. White, and P. J. Tobin, *J. Vac. Sci. Technol. B* **23**, 2480 (2005).
- D. H. Triyoso, R. I. Hegde, J. M. Grant, J. K. Schaeffer, D. Roan, B. E. White, and P. J. Tobin, *J. Vac. Sci. Technol. B* **23**, 288 (2005).
- J. Tyczkowski, R. Kapica, and J. Lojewska, *Thin Solid Films* **515**, 6590 (2007).
- V. Vaithyanathan, J. Lettieri, W. Tian, A. Sharan, A. Vasudevarao, Y. L. Li, A. Kochhar, H. Ma, J. Levy, P. Zschack, J. C. Woicik, L. Q. Chen, V. Gopalan, and D. G. Schlom, *J. Appl. Phys.* **100**, 024108 (2006).
- C. A. F. Vaz, E. I. Altman, and V. E. Henrich, *Phys. Rev. B* **81**, 104428 (2010).
- C. A. F. Vaz, H.-Q. Wang, C. H. Ahn, V. E. Henrich, M. Z. Baykara, T. C. Schwendemann, N. Pilet, B. J. Albers, U. D. Schwarz, L. H. Zhang, Y. Zhu, J. Wang, and E. I. Altman, *Surf. Sci.* **603**, 291–297 (2009).
- C. A. F. Vaz, D. Brabhakaran, E. I. Altman, and V. E. Henrich, *Phys. Rev. B* **80**, 155457 (2009).

M. Vehkamäki, T. Hatanpää, T. Hänninen, M. Ritala, and M. Leskelä, *Electrochem. Solid-State Lett.* **2**, 504 (1999).

M. Vehkamäki, T. Hänninen, M. Ritala, M. Leskelä, T. Sajavaara, E. Rauhala, and J. Keinonen, *Chem. Vapor Deposition* **7**, 75 (2001).

S. Verdier, L. El Ouatani, R. Dedryvère, F. Bonhomme, P. Biensan, and D. Gonbeau, *J. Electrochem. Soc.* **154**, A1088–A1099 (2007).

R. Vogel, K. Pohl, and H. Weller, *Chem. Phys. Lett.* **174**, 241 (1990).

A. Walsh, S.-H. Wei, Y. Yan, M. M. Al-Jassim, J. A. Turner, M. Woodhouse, and B. A. Parkinson, *Phys. Rev. B* **76**, 165119 (2007).

Z. L. Wang, *Sur. Sci.* **360**, 180–186 (1996).

T. Warang, N. Patel, A. Santini, N. Bazzanella, A. Kale, and A. Miotello, *Appl. Catal.* **21**, 213–214 (2012).

M. P. Warusawithana, C. Cen, C. R. Sleasman, J. C. Woicik, Y. Li, L. F. Kourkoutis, J. A. Klug, H. Li, P. Ryan, L. P. Wang, M. Bedzyk, D. A. Muller, L. Q. Chen, J. Levy, and D. G. Schlom, *Science* **324**, 367–370 (2009).

M. P. Warusawithana, C. Richter, J. A. Mundy, P. Roy, J. Ludwig, S. Paetel, T. Heeg, A. A. Pawlicki, M. Zheng, M. Lee, B. Mulcahy, W. Zander, Y. Zhu, J. Schubert, J. N. Eckstein, D. A. Muller, C. S. Hellberg, J. Mannhart, and D. G. Schlom, *Nature Comm.* **4**, 2351 (2013).

Y. Wei, X. Hu, Y. Liang, D. C. Jordan, B. Crago, R. Droopad, Z. Yu, A. Demkov, J. L. Edwards Jr., and W. J. Ooms, *J. Vac. Sci. Technol. B* **20**, 1402 (2002).

P. R. Willmott, S. A. Pauli, R. Herger, C. M. Schlepütz, D. Martoccia, B. D. Patterson, B. Delley, R. Clarke, D. Kumah, C. Cionca, and Y. Yacoby, *Phys. Rev. Lett.* **99**, 155502 (2007).

K.-M. Wu, K.-W. Cheng, C.-Y. Tsai, and C.-S. Tsai, US2014/0048893 A1 (2012).

W. F. Xiang, H. B. Lu, Z. H. Chen, X. B. Lu, M. He, H. Tian, Y. L. Zhou, C. R. Li, and X. L. Ma, *J. Cryst. Growth* **271**, 165–170 (2004).

H. Yamamoto, T. Naito, M. Terao, and T. Shintani, *Thin Solid Films* **411**, 289 (2002).

S. Yamane, N. Kato, S. Kojima, A. Imanishi, S. Ogawa, N. Yoshida, S. Nonomura, and Y. Nakato, *J. Phys. Chem. C* **113** (32), 14575 (2009).

M. Yin, Z. Li, J. Kou, and Z. Zou, *Environ. Sci. Technol.* **43**, 8361 (2009).

X.-Y. Yu, Q.-Q. Meng, T. Luo, Y. Jia, B. Sun, Q.-X. Li, J.-H. Liu, and X.-J. Huang, *Scientific Reports* **3**, 2886 (2013).

Z. Yu, J. Ramdani, J. A. Curless, C. D. Overgaard, J. M. Finder, R. Droopad, K. W. Eisenbeiser, J. A. Hallmark, W. J. Ooms, and V. S. Kaushik, *J. Vac. Sci. Technol. B* **18**, 2139 (2000).

Z. Yu, J. Ramdani, J. A. Curless, J. M. Finder, C. D. Overgaard, R. Droopad, K. W. Eisenbeiser, J. A. Hallmark, W. J. Ooms, J. R. Conner, and V. S. Kaushik, *J. Vac. Sci. Technol. B* **18**, 1653 (2000).

S. Yuasa and D. D. Djayaprawira, *J. Phys. D: Appl. Phys.* **40**, R337–R354 (2007).

J. Zhang, H. Zhu, S. Zheng, F. Pan, and T. Wang, *Appl. Mater. Inter.* **1**, 2111 (2009).

L. Zhang, C. Lange, I. Abraham, S. Storck, W.F. Maier, and H. Kisch, *J. Phys. Chem. B* **102**, 10765 (1998).

C. Zhao, C. Z. Zhao, M. Werner, S. Taylor, and P. R. Chalker, *ISRN Nanotechnol.* **2012**, 689023 (2011).

D. K. Zhong and D. R. Gamelin, *J. Am. Chem. Soc.* **132**, 4202 (2010).

D. K. Zhong, S. Choi, and D. R. Gamelin, *J. Am. Chem. Soc.* **133**, 18370 (2011).

R.-S. Zhou and R. L. Snyder, *Acta Cryst. B* **47**, 617 (1991).

C. G. Zimmermann, M. Yeadon, K. Nordlund, J. M. Gibson, R. S. Averback, U. Herr, and K. Samwer, Phys. Rev. Lett. **83**, 1163 (1999)

Z. Zou, J. Ye, K. Sayama, and H. Arakawa, Nature **414**, 625 (2001).

P. Zubko, S. Gariglio, M. Gabay, P. Ghosez, and J.-M. Triscone, Annu. Rev. Condens. Matter Phys. **2**, 141 (2011).

[http://www.flashmemorysummit.com/English/Collaterals/Proceedings/2009/20090813\\_ThursPlenary\\_Tabrizi.pdf](http://www.flashmemorysummit.com/English/Collaterals/Proceedings/2009/20090813_ThursPlenary_Tabrizi.pdf).

<http://www.itrs.net/Links/2011ITRS/Home2011.htm>

M. T. Bohr, R. S. Chau, T. Ghani and K. Mistry,  
<http://spectrum.ieee.org/semiconductors/design/the-highk-solution>, (2007)

## Vita

Thong Quang Ngo was born and raised in Binh Dinh, Vietnam. He attended the Petroleum-Gas University of Ploiest, Romania, from 2004–2009 at which he attained his Bachelor of Science degree in Chemical Engineering. He received the Vietnam Education Foundation Scholarship in September 2009. Thong married his wife, Van, in January 2014.

Thong joined Dr. John G. Ekerdt's research group at The University of Texas at Austin in the Fall of 2010. Then he started his research on depolymerization of lignin and model compounds under the supervision of Dr. John G. Ekerdt. In August 2011, Thong switched his graduate research and began researching advanced functional materials under the supervision of Dr. John G. Ekerdt. His research focused on chemical routes to integrate functional materials on semiconductors for various applications. During his graduate study, Thong interned at Micron technology Inc. Boise, ID in the Summer of 2013 where he developed high work-function materials for metal-insulator-metal DRAM cell capacitors. His work has been published internally in a technical leadership program journal at Micron.

Thong has authored and co-authored 13 journal articles (five first-author and eight co-author) that are currently printed in refereed journals. One first-author article is currently under review and one first-author and more than three additional co-author articles are in preparation for submission at the date of this dissertation filing.

Permanent e-mail address: ngoquangthongphucacat@gmail.com

This dissertation was typed by Thong Quang Ngo